POLITECNICO DI TORINO

SCUOLA DI DOTTORATO
Dottorato inIngegneria Elettronica e delle Comunicazioni – XXVI
ciclo

Tesi di Dottorato

Simulation and Design of an UWB Imaging System for Breast Cancer Detection

Xiaolu Guo

| **Tutore** | **Coordinatore del corso di dottorato** |
| prof. Maurizio Zamboni | prof. Ivo Montrosset |

April 2014

Summary

Breast cancer is the most frequently diagnosed cancer among women. In recent years, the mortality rate due to this disease is greatly decreased thanks to both enormous progress in cancer research, and screening campaigns which have allowed the increase in the number of early diagnoses of the disease. In fact, if the tumor is identified in its early stage, e.g. when it has a diameter of less than one centimeter, the possibility of a cure can reach 93%. However, statistics show that more young aged women are suffered breast cancer.

The goal of screening exams for early breast cancer detection is to find cancers before they start to cause symptoms. Regular mass screening of all women at risk is a good option to achieve that. Instead of meeting very high diagnostic standards, it is expected to yield an early warning, not a definitive diagnosis. In the last decades, X-ray mammography is the most efficient screening technique. However, it uses ionizing radiation and, therefore, should not be used for frequent check-ups. Besides, it requires significant breast compression, which is often painful. In this scenario many alternative technologies were developed to overcome the limitations of mammography. Among these possibilities, Magnetic Resonance Imaging (MRI) is too expensive and time-consuming, Ultrasound is considered to be too operator-dependent and low specificity, which are not suitable for mass screening. Microwave imaging techniques, especially Ultra WideBand (UWB) radar imaging, is the most interesting one. The reason of this interest relies on the fact that microwaves are non-ionizing thus permitting frequent examinations. Moreover, it is potentially low-cost and more efficient for young women. Since it has been demonstrated in the literatures that the dielectric constants between cancerous and healthy tissues are quite different, the technique consists in illuminating these biological tissues with microwave radiations by one or more antennas and analyzing the reflected signals.

An UWB imaging system consists of transmitters, receivers and antennas for the RF part, the transmission channel and of a digital backend imaging unit for processing the received signals. When an UWB pulse strikes the breast, the pulse is reflected due to the dielectric discontinuity in tissues, the bigger the difference, the bigger the backscatter. The reflected signals are acquired and processed to create the energy maps. This thesis aims to develop an UWB system at high resolution for

the detection of carcinoma breast already in its initial phase. To favor the adoption of this method in screening campaigns, it is necessary to replace the expensive and bulky RF instrumentation used so far with ad-hoc designed circuits and systems. In order to realize that, at the very beginning, the overall system environment must be built and verified, which mainly consists of the transmission channel–the breast model and the imaging unit. The used transmission channel data come from MRI of the prone patient. In order to correctly use this numerical model, a simulator was built, which was implemented in Matlab, according to the Finite-Difference-Time-Domain (FDTD) method. FDTD algorithm solves the electric and magnetic field both in time and in space, thus, simulates the propagation of electromagnetic waves in the breast model. To better understand the effect of the system non-idealities, two 2D breast models are investigated, one is homogeneous, the other is heterogeneous. Moreover, the modeling takes into account all critical aspects, including stability and medium dispersion. Given the types of tissues under examination, the frequency dependence of tissue dielectric properties is incorporated into wideband FDTD simulations using Debye dispersion parameters. A performed further study is in the implementation of the boundary conditions. The Convolution Perfectly Matched Layer (CPML) is used to implement the absorbing boundaries.

The objective of the imaging unit is to obtain an energy map representing the amount of energy reflected from each point of the breast, by recombining the sampled backscattered signals. For this purpose, the study has been carried out on various beamforming in the literature. The basic idea is called as "delay and sum", which is to align the received signals in such a way as to focus a given point in space and then add up all the contributions, so as to obtain a constructive interference at that point if this is a diseased tissue. In this work, Microwave Imaging via Space Time (MIST) Beamforming algorithm is applied, which is based on the above principle and add more elaborations of the signals in order to make the algorithm less sensitive to propagation phenomena in the medium and to the non-idealities of the system. It is divided into two distinct steps: the first step, called SKin Artifact Removal (SKAR), takes care of removing the contributions from the signal caused by the direct path between the transmitter and receiver, the reflection of skin, as they are orders of magnitude higher compared to the reflections caused by cancers; the second step, which is BEAmForming (BEAF), performs the algorithm of reconstruction by forming a weighted combination of time delayed version of the calibrated reflected signals.

As discussed above, more attention must be paid on the implementation of the ad-hoc integration circuits. In this scenario, due to the strict requirements on the RF receiver component, two different approaches of the implementation of the RF front-end, Direct Conversion (DC) receiver and Coherent Equivalent Time Sampling (CETS) receiver are compared. They are modeled behaviorally and the effects of various impairments, such as thermal, jitter, and phase noise, as well as phase

inaccuracies, non-linearity, ADC quantization noise and distortion, on energy maps and on quantitative metrics such as SCR and SMR are evaluated. Differential Gaussian pulse is chosen as the exciting source. Results show that DC receiver performs higher sensitivity to phase inaccuracies, which makes it less robust than the CETS receiver. Another advantage of the CETS receiver is that it can work in time domain with UWB pulses, other than in frequency domain with stepped frequency continuous waves like the DC one, which reduces the acquisition time without impacting the performance.

Based on the results of the behavioral simulations, low noise amplifier (LNA) and Track and Hold Amplifier (THA) can be regarded as the most critical parts for the proposed CETS receiver, as well as the UWB antenna. This work therefore focuses on their hardware implementations. The LNA, which shows critical performance limitation at bandwidth and noise figure of receiver, has been developed based on common-gate configuration. And the THA based on Switched Source Follower (SSF) scheme has been presented and improved to obtain high input bandwidth, high sampling rate, high linearity and low power consumption. LNA and THA are implemented in CMOS 130 nm technology and the circuit performance evaluation has been taken place separately and together. The small size UWB wide-slot antenna is designed and simulated in HFSS.

Finally, in order to evaluate the effect of the implemented transistor level components on system performance, a multi-resolution top-down system methodology is applied. Therfore, the entire flow is analyzed for different levels of the RF frontend. Initially the system components are described behaviorally as ideal elements. The main activity consists in the analysis and development of the entire frontend system, observing and complementing each other blocks in a single flow simulation, clear and well-defined in its various interfaces. To achieve that the receiver is modeled and analyzed using VHDL-AMS language block by block, moreover, the impact of quantization, noise, jitter, and non-linearity is also evaluated. At last, the behavioral description of antenna, LNA and THA is replaced with a circuit-level one without changing the rest of the system, which permits a system-level assessment of low-level issues.

Acknowledgements

Contents

List of Tables

List of Figures

XI

XIII

Chapter 1

Introduction

Nowadays, breast cancer is the most common form of cancer affecting women worldwide. About 1/8 U.S. women (just under 12%), 1/12 Europe women and 1/40 Asia women will develop invasive breast cancer over the course of her lifetime. All women have the chances of developing breast cancer. The risk of developing breast cancer increases with age beginning in the fourth decade of life. The probability of developing invasive breast cancer over the next decade is 0.4% for women aged 30-39, 1.5% for women aged 40-49, 2.8% for women aged 50-59, and 3.6% for women aged 60-69.

Recent research indicates that the five-year disease-free relative survival rate was greater than 98% for women with a 20 mm or smaller invasive cancer (stage I) which has not spread to lymph nodes yet, compared to 86% for stage II disease (1-3 positive axillary lymph nodes and/or primary tumor size 21 to 50 mm) [1]. Therefore, early detection is believed to be crucial to reduce the breast cancer death by finding cancers at smaller sizes and thus treating more effectively. Breast cancers can be found by clinical breast exam or by a woman herself, but such tumors have a median size of 20 to 25 mm [2]. Tumors with such sizes are more likely to be later stage breast cancers that are logically have already spread to the axillary lymph nodes and are likelier to be lethal. Hence detecting tumors at a nonpalpable early stage becomes the philosophy that drives the development of breast cancer screening technology. With advances in screening, diagnosis and treatment, the death rate for breast cancer has declined considerably over the past decade.

In the literatures, there are different kinds of screening method for detecting breast cancer such as X-ray mammography, ultrasound, Computed Tomography (CT) and Magnetic Resonance Imaging (MRI). Currently the most widely used method is X-ray mammography. In this chapter different breast cancer detection screening methods will be introduced and compared.

1.1 Mammography

Nowadays, X-ray mammography is the most common screening method to detect breast cancer in women who have no signs or symptoms of the disease. It uses x-rays to produce images of the breast. In other words, mammography provides information about breast morphology, normal anatomy, and gross pathology. The overall procedure includes tightly compressing the breast between two parallel plates. A x-ray pulse is then used to take the image. During the procedure, the breast is flattened to evenly spread out the tissue. Consequently, the x-ray attenuation is about the same within the overall region of the breast. In addition, the radiation dosage absorbed by the breast is at a minimum value. The whole procedure takes about 20 minutes. Film-screen mammography and digital mammography are the two main types of mammography. The techniques for performing them are the same. What differs is whether the images take the form of photographic films or of digital files recorded directly onto a computer.

The effective of mammographic screening before age 50 years is less than at older ages and the associated radiation risks are higher, due to the fact that younger women have denser breasts that contain microcalcifications and have thick epithelial tissue, so as to absorb more of the radiation from the surface. Therefore, the radiation logically penetrates less deeper into the breast tissue, which is the area where malignant cancers are most likely to be found.

The researches showed that cancer detection with digital or film-screen mammography is similar in U.S. women aged 50 to 79 years going through screening mammography. However, digital mammography is significantly better that film mammography in screening women who are under age 50, or women of any age who had very dense breasts [3]. Nevertheless, one of the obstacles to greater use of digital mammography is its cost, it costs about 1.5 to 4 times more than film mammography. The mammography that will talk about in the following is film mammography. In women aged 50 years old, mammography's sensitivity has been estimated to range from 68% to over 90%, with most trials achieving sensitivities of about 85%. In women aged 40-49, however, the sensitivity has been reported to be about 62%. The specificity of mammography ranges between 82% and 97%.

High-quality, two view screening mammography is able to find the relatively small breast cancers, with median size 1.0 to 1.5 cm. Because of its important role in detecting tumor earlier, mammography has played a substantial role in reducing the mortality rate by 20% in the last decade [4]. However, x-ray mammography has the following shortages:

- Radiation exposure. As with all x-ray examinations, there is some radiation exposure, although mammography uses low energy ionizing x-rays at low radiation doses to create an image, frequently repeated x-rays still may cause

cancer.

- High false positive. False-positive results occur when radiologists decide mammograms are odd but no cancer is actually present. On the whole, screening mammograms misdiagnose about 12 percent of breast cancers that are present at the time of screening. It may lead to anxiety and other forms of psychological distress in affected women. The additional imaging studies and invasive procedures (such as biopsy or fine-needle aspiration) required to exclude cancer can also be costly and cause physical discomfort. False-positive results and accompanying additional imaging studies are more common in younger women.

- High false negative. Up to 20% false-negative rates, false-negative results occur when mammograms appear normal even though breast cancer is present. The main cause of false-negative results is high breast density. Breasts contain both dense fibroglandular tissue and fatty tissue. Fatty tissue appears dark on a mammogram, whereas fibroglandular tissue appears as white areas. Since fibroglandular tissue has similar density with tumors, it is harder to detect tumor in women with denser breasts. This phenomena appear more often among younger women than older women. False-negative results can lead to delays in treatment and a false sense of security for influenced women.

- Overdiagnosis and overtreatment. Screening mammograms can find cancers and cases of ductal carcinoma in situ (DCIS, a noninvasive tumor in which abnormal cells that may become cancerous build up in the lining of breast ducts) that need to be treated. However, some cases of DCIS will never cause symptoms which may bring out "overdiagnosis", the subsequently unnecessary treatment is called as "overtreatment".

Other potential harms, such as pain caused by the procedure, exist but are thought to have tolerable effect on mammography use. All of these limitations and their associated potential for harm, along with the additional health risks associated with x-ray's ionizing radiation, give impetus to the development of alternative techniques of breast cancer detection.

1.2   alternative methods

In this section, several important alternative methods are introduced.

1.2.1 Breast Ultrasound

Ultrasound, also known as sonography, uses ultrasound waves to profile a part of the body. Ultrasound waves are high-frequency sound waves that reflect at boundaries between tissues with different acoustic properties. The depth of these boundaries is related to the time intervals of reflection arrivals. The echoes are converted into a black and white image and displayed on a computer screen. Thus, the image of tissue boundaries can be mapped. Ultrasound helps distinguish between cysts (fluid-filled sacs) and solid masses and sometimes can help telling the difference between benign and cancerous tumors. It holds promise as a method for detection of cancers in women with dense breast tissue, which is often problematic with conventional X-ray mammography [4]. Ultrasound has also assumed an important role in breast imaging, as an adjunct to serial evaluation of benign masses, palpable mass evaluation, and diagnostic mammography for biopsy guidance [4]. In the last few years, great steps have been made in improving image quality and resolution of all ultrasound machines. These improvements were benefited from the new transducer design technology and advances in electronic signal processing.

This test is not painful and does not expose you to radiation. Unfortunately, even though ultrasound is also a valid and low-cost method for breast imaging, it is just a complementary method, the use of ultrasound instead of mammograms for breast cancer screening is not suggested. Normally, it is used to target a specific area of concern found on the mammogram. Its major limitation is that breast fat and most cancer cells have similar acoustic properties, which reduces the detection efficiency. Also, its imaging results are highly operator-dependent, as the vast majority of ultrasound procedures are executed using hand-held devices.

1.2.2 Magnetic Resonance Imaging

MR images are created by acquiring the signals generated after radio frequency excitation of nuclear particles in tissue exposed to a strong magnetic field [4]. The signals have characteristics that vary according to tissue type. Magnetic resonance imaging (MRI) relies on the interaction of RF energy and strong magnetic fields with the magnetic properties of certain atoms to produce high resolution images. In MRI, a strong magnet is first employed to align the protons of the hydrogen (also possibly phosphorus or sodium) atoms, and then pulsed RF energy is used to tip the protons out of alignment. Once the RF pulse ends, as the individual protons return to alignment and begin to precess at different rates, they transmit an RF signal that is detected by antennas in the MR device. Imaging is possible because these return signals vary in intensity and phase based on the strength of the magnetic field, the frequency and pattern of the RF pulses, and the properties of the tissue. The tissue properties at each location can be mapped to form high resolution 3D images by

encoding location information using magnetic field gradients and different sequences of RF pulses.

If a suspected area exhibits contrast agent uptake, the probability that it is malignant is very big, it may or may not be a tumor. Conversely, its specificity is better. Further imaging or biopsy may be needed to confirm the suspicion. MRI is also used to image breast tissue near implants, where x-ray mammography is poor. Despite the fact that MRI is more sensitive in detecting cancers than mammography, ultrasound, or clinical breast exam, it has higher false positive rate. These false positive findings have to be checked out to know that cancer is not present, which means coming back for further tests and/or biopsies. The studies have shown that MRI had a specificity of only 95.4 percent, compared to 96, 99.3, and 99.8 percent for ultrasound, clinical breast exam and mammography, respectively. Another important drawback is its higher cost and more time-consuming than mammography. Moreover, it is uncomfortable during the examination, the patient should be able to remain perfectly still. All these above shortcomings severely limit the widespread application as a early breast imaging technique.

1.2.3 Microwave Imaging

The shortcomings of these techniques have motivated the search for better alternatives. The microwave imaging approach has the potential for a much higher sensitivity in detecting tumors and higher specificity in differentiating malignant and benign tumors, as it benefits from the significant dielectric contrast between malignant and healthy tissues at microwave frequencies (between 2:1 and 10:1) [5][4], whereas for X-rays the contrast is only a few percent.

Microwave imaging is safe without using ionizing radiations, relatively comfortable without compressing breast. Considering real implementation, the test instrumentation is mature, compact, thus it is potentially cheaper than X-ray mammography and MRI. It is potentially more efficient with younger patients. One of the main reason for the unsolved breast cancer problem is lack of efficiency of early detection. The growing speed of the tumor from 10 mm is fast and the chances of survival are better than 90% if malignant growth is removed before it reaches a size of about 1.5 cm in any given direction. This implies frequently repeated examinations of all women above the age of 45-50 years. Mass screening method is a good solution for that, it need not meet very high diagnostic standards, just an early warning, not a definitive diagnosis [6]. To meet the requirement of mass screening, the examination should be cheap, safe and easy to operate, otherwise, it is difficult for patient to persist doing that. The existing breast imaging methods as introduced above, of which X-ray mammography and MRI are most common, are not suitable for mass screening. X-ray mammography is not safe for frequently tests as it uses ionizing

radiation, Besides, it requires significant breast compression, which is often uncomfortable and even painful. Ultrasound on the other hand is too operator-dependent and of low specificity. MRI is considered to be too expensive and time-consuming.

It is reasonable to assume that microwave breast cancer imaging for mass-screening purposes should aim at the sensitivity levels of mammography and the specificity levels of MRI in order to be competitive to both and yet have the advantage of being a cheaper and safer modality. At this time, extensive research and development is being carried out worldwide toward microwave imaging systems, which could achieve this goal.

During the past several decades, many microwave imaging techniques, including passive, hybrid and active approaches, have been explored for breast cancer detection. From the basic concepts of each approach, researchers have investigated different techniques to achieve a suitable system for breast cancer detection. The investigated techniques are illustrated in Figure 1.1.
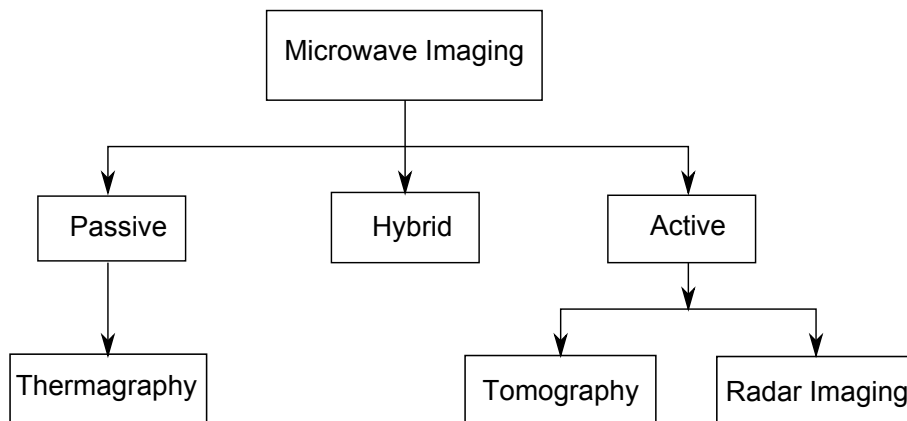
Figure 1.1. A summary of the most actively pursued methods for image reconstruction from microwave measurements.

The passive approaches detect malignant tumors based on the contrast between the temperatures of the cancerous tissue to that of the normal one [9]. The radiometers are used to measure the temperature differences. Under the illumination of the microwave radiation the tumor shows a greater increase in temperature compared with healthy breast tissue [7][8]. The main challenge to this method is to detect a very low level power radiated by tumors, which causes technical problems. The other difficulty comes from the temperature distribution inside the body. It is hard to distinguish between a cool target close to the skin and a hot target located deep in the breast [10].

Hybrid (acoustic) microwave imaging systems use microwaves to rapidly illuminate the selected areas in the breast and ultrasound transducers are used to detect

the pressure waves generated by the expansion of the heated tissues [9]. The heterogeneity (asymmetric nature) of breast is a major challenge being faced by this technique, since the microwave energy illuminated on the breast surface results in a non-uniform response being received that requires complicated algorithms to generate the image. The received heat energy which is called as thermal acoustic signals includes responses from all kind of tissues, such as breast skin, breast tissues and tumor. The reflected skin signals are much stronger than small tumors due to the high conductivity of skin and the smaller distance between acoustic sensors and skin. Moreover, because of the heterogeneity nature of the breast, the speed of the received acoustic signal is non-uniform, and therefore causing a problem in accurately determining the time of the acoustic pulse generated at a particular location [10]. All these factors make it difficult to approximate the tumor location in the breast.

Unlike passive and hybrid techniques, as discussed above, the active approaches rely on the significant electrical properties contrast between malignant and normal breast tissues at microwave frequencies, and two different types of technique have achieved promising results: microwave tomography and ultra-wideband (UWB) microwave imaging.

Tomography

The goal of microwave tomography is to use the scattered signals to reconstruct the complete dielectric profile of the breast. The narrowband signals are applied and the reflected signals received by antennas are used to create a trace of electrical properties of the breast, using algorithms that basically match measurements of the microwave signal scattered by the breast to results computed with a model. The existence of tumors reduces the strength of the scattered signal, which results in areas of increased permittivity and conductivity on images. This method requires solving both forward scattering problem and nonlinear ill-conditioned inverse scattering problem iteratively, until the computed and the measured data are close enough.

The tomographic approach has shown significant promise in both detecting small tumors and also differentiating between malignant and benign tissue for lesions as small as 1 cm in diameter. Several research groups are working on this approach [11][12].

UWB radar imaging

Ultra-wideband (UWB) radar technique was introduced by S.C. Hagness in 1998. The key point of the technique is time shifting and summing (synthetic focusing) of scattered waveforms, thereby determines the location of microwave scatterers within the breast. One of the advantages of UWB microwave imaging systems is that they receive and process the reflected data in a very wide frequency band that can be

up to 10 GHz. The large bandwidth allows the UWB radar to obtain more information about the possible surrounding targets and detect, identify, and locate only the most desired target among others. This fine spatial resolution makes the ultra wideband radar beneficial for medical applications. The properties of short UWB pulse indicate that the UWB signal can penetrate a great variety of breast tissues. However, since the length of UWB pulse has the same order of magnitude with the potential objects, UWB radar scattered pulses are changed by the electrical characteristics and target structure. Those changes in pulse waveform provide valuable information such as material properties and shape about the objects. Discrimination of object using higher order signal processing of impulse signals can distinguish between materials that would not be otherwise distinguishable by the narrowband signals, at the expense of complex signal processing.

Rather than using the tomographic approach of reconstructing the entire dielectric profile of the breast, which carries more information, UWB radar imaging uses the following beamforming algorithm to build the image of scatterers distribution only. Hence, the big advantage of radar-based imaging over the tomographic imaging is its less computational complex and robust signal processing.

1.3 System overview

Since the microwave technique allows to obtain a compromise between resolution and penetration depth. Moreover the development of a low cost system is theoretically possible using this technology. An high resolution breast cancer detection system would be developed using this method. The diagram of the system is shown in Figure 2.1. It consists of channel model breast, RF front-end transceiver and antenna array, and back-end imaging reconstruction unit. The working flow of the system is the following: the powerful transmitter generates UWB pulse and radiates to breast by transmitting antenna. Due to the difference in dielectric properties of the breast tissues, the wave scatters at each dielectric discontinuity. Consequently, the backscattered pulse acquired by a highly sensitive receiver contains information on the presence and position of the scatter, in the form of the magnitude and arrival time of the reflected pulse. The energy map of the breast can be reconstructed and the tumor can be identified by processing a set of obtained data from antenna array in the following imaging reconstruction unit.
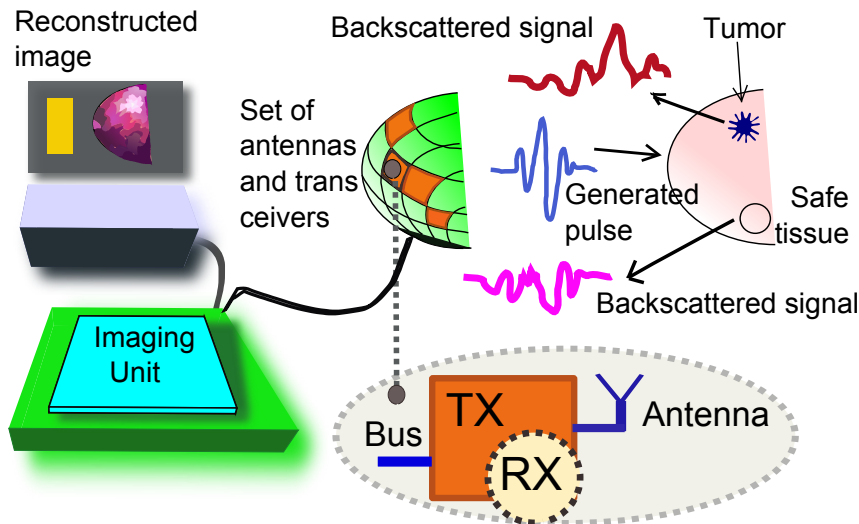
Figure 1.2. An overview of breast cancer detection system. UWB pulses are radiated against the breast and the echoes are acquired with a set of transceivers and antennas. An imaging unit processes the data and produces a map of reflected energy. Cancerous tissues have higher dielectric constant, resulting in high reflected energy

1.4 Thesis outline

There are four primary topics of interest discussed in this thesis, including the microwave breast cancer detection system analysis, microwave imaging system verification, hardware modeling and design, and simulation performances of the overall system. The thesis work begins with Chapter2 which describes the system modeling and design environment, the numerical transmission channel, breast model, is built, the front-end components are introduced and the imaging reconstruction algorithm is analyzed. Chapter 3 presents the system feasibility of the system environment by setting proper system parameters. In Chapter 4, UWB receivers for this specific application are proposed and modeled behaviorally, followed by circuit impairments consideration of each individual radar receiver components. In Chapter 5, UWB antenna and some other circuit design in $0.13\,\mu m$ CMOS are presented. Chapter 6 illustrates the influence of the designed hardware components on system performance evaluation. A multi-resolution environment is built to evaluate the influence of various non-idealities of front-end components. Finally, the conclusion is given in Chapter 7.

Chapter 2

UWB Imaging System

The main UWB microwave imaging system components are shown in Figure 2.1. Antennas, transmitters, and receivers are arranged in an anatomically shaped support places in close proximity to a patient's breast. Transmitting antennas are activated in turn, while receiving antennas can be activated all at once or one by one (multistatic vs monostatic approach). Receivers acquire antenna signals and send digitized data to the front-end interface, which collects and prepare them for the elaboration performed by the imaging unit. During the processing first the contribution of skin reflection that is typically larger than tumor information is eliminated, and then all signals are realignd so as to focus them on a single point of the breast volume. The energy reflected by that point is computed and the procedure repeated for all image points, according to the chosen resolution. To speed up the computation, specialized hardware accelerators cooperate with a standard microprocessor. The image is finally displayed on a standard PC screen.

Apart from the transmission channel, the breast, the imaging system can be ideally partitioned in two main components, the RF part that generates and acquires the UWB signal, which we term as front-end, and the part that processes the data and produces the image of reflected energy, termed as back-end. In the following they are introduced one by one.

2.1   Transmission channel

First of all, it is important to understand which tissues compose the breast, an example of the breast anatomy is shown in Figure 2.2. It includes adipose tissues (fat), glandular tissues, skin, nipple and chest wall. The glandular tissue, which appears white or "dense", as defined by radiologists, is represented in the breast together with the adipose tissue, or fat, which appears dark in contrast during the mammographic, or "ray", always using the language of radiologists.
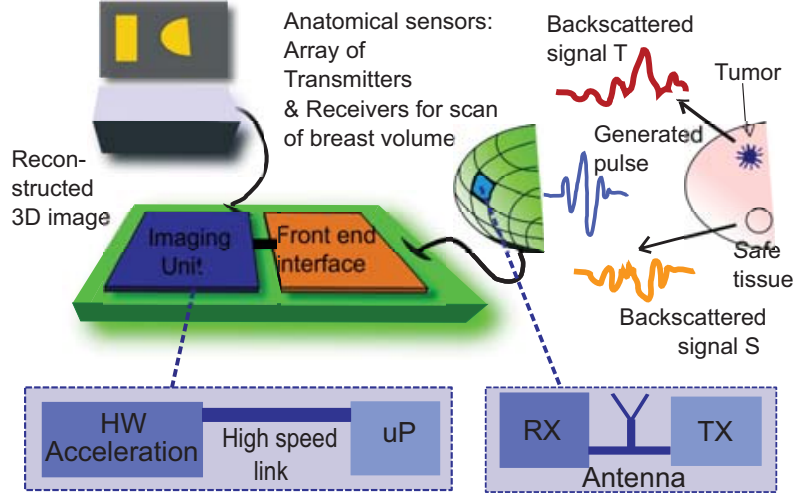
Figure 2.1.   An overview of breast cancer detection system.

In order to analyze the performance of the imaging system under development, simulations of the channel transmission, the breast must be carried out. To achieve that, a numerical study model should be built and simulated to imitate the microwave propagation in the breast. Several key electromagnetic simulation techniques have been developed over recent years, including the Method of Moments (MoM), Finite Element (FEM) and Finite Difference Time Domain (FDTD) solutions [13]. MOM method is not proper for general three-dimensional (3D) structures, whereas FEM and FDTD simulation methods are true 3D field solver which can be used for any type of 3D structure. In contrast to MOM and FEM algorithms, which work in the frequency domain and solve Maxwell's equations implicitly, FDTD algorithms work in the time domain and solve Maxwell's equations in a fully clear way. For a FDTD analysis, simulated targets are placed within a "box" with defined borders, to truncate the analysis space and define the simulation domain. The volume of the simulation domain is filled by discrete elements, known as "Yee" cells. FDTD employs a time-stepping algorithm, which updates the field values across the mesh cell time-step by time-step, hereby explicitly following the EM waves as they propagate through the structure. The required time to implement a basic FDTD solver is at least an order of magnitude less work than either an FEM or MoM solver.

Thanks to the above properties, FDTD modeling is frequently used in many applications like radar signature technology, radiation antenna analysis, wireless communication devices examination and digital interconnections. In 1998, Hagness et al introduced FDTD modeling for breast cancer detection using ultra wide-band radar techniques [4].
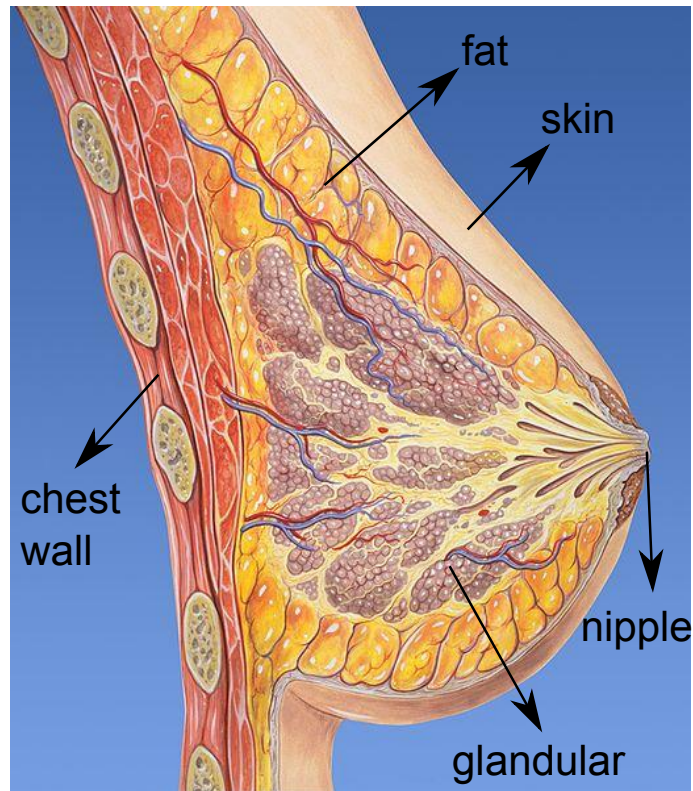
Figure 2.2.   Anatomy of breast.

2.1.1   FDTD method

FDTD method is easy to understand and easy to implement in software, which are given by, FDTD is a time-domain technique, when a broadband pulse (such as a Gaussian pulse) is used as the source, the response of the system over a wide range of frequencies can be obtained with a single simulation. It processes Maxwell's curl equations with differential form. In the following, the basis of the FDTD numerical technique for solving Maxwell's curl equations directly in the time domain on a space grid will be described. Maxwell's curl equations are given by equations (2.1) and (2.2):

$$\nabla \times H = \frac{\partial D}{\partial t} + J \tag{2.1}$$

$$\nabla \times E = -\frac{\partial B}{\partial t} - J_m \tag{2.2}$$

where
   E is the electric field;

H is the magnetic field;

B is the magnetic flux density;

D is the electric flux density;

J is the electric current density;

J_m is the equivalent magnetic current density.

Moreover, in linear, isotropic, non-dispersive materials, we can define the following proportions:

$$D = \varepsilon E = \varepsilon_r \varepsilon_0 E, \qquad B = \mu H = \mu_r \mu_0 H, \qquad J = \sigma E, \qquad J_m = \sigma_m H \qquad (2.3)$$

where

ε represents the electric permittivity;

ε_r represents the relative electric permittivity;

ε_0 represents the free-space electric permittivity;

μ represents the magnetic permeability;

μ_r represents the relative magnetic permeability;

μ_0 represents the free-space magnetic permeability;

σ represents the electrical conductivity;

σ_m represents the magnetic conductivity.

In the Cartesian coordinate system, equation (2.1) and (2.2) can be written as:

$$\begin{aligned}
\frac{\partial H_z}{\partial y} - \frac{\partial H_y}{\partial z} &= \varepsilon \frac{\partial E_x}{\partial t} + \sigma E_x \\
\frac{\partial H_x}{\partial z} - \frac{\partial H_z}{\partial x} &= \varepsilon \frac{\partial E_y}{\partial t} + \sigma E_y \\
\frac{\partial H_y}{\partial x} - \frac{\partial H_x}{\partial y} &= \varepsilon \frac{\partial E_z}{\partial t} + \sigma E_z
\end{aligned} \qquad (2.4)$$

and,

$$\begin{aligned}
\frac{\partial E_z}{\partial y} - \frac{\partial E_y}{\partial z} &= -\mu \frac{\partial H_x}{\partial t} - \sigma_m H_x \\
\frac{\partial E_x}{\partial z} - \frac{\partial E_z}{\partial x} &= -\mu \frac{\partial H_y}{\partial t} - \sigma_m H_y \\
\frac{\partial E_y}{\partial x} - \frac{\partial E_x}{\partial y} &= -\mu \frac{\partial H_z}{\partial t} - \sigma_m H_z
\end{aligned} \qquad (2.5)$$

It can be seen that the change in the E-field in time (the time derivative) is dependent on the change in the H-field across space (the curl) when Maxwell's differential equations (2.1) and (2.2) are examined. This leads to the basic FDTD time-stepping relation that, at any point in space, the updated value of the E-field in time is dependent on the stored value of the E-field and the numerical curl of the local distribution of the H-field in space [14]. The H-field is time-stepped in a

similar manner. At any point in space, the updated value of the H-field in time is dependent on the stored value of the H-field and the numerical curl of the local distribution of the E-field in space. Iterating the E-field and H-field update results in a marching-in-time process wherein sampled-data of the continuous electromagnetic waves under consideration propagate in a numerical grid stored in the computer memory.

Now the difference discrete of equation (2.4) and (2.5) are taken into consideration. $f(x,y,z,t)$ represents the arbitrary component of E-field or H-field, its discrete sample in time and space domain can be represented as in equation (2.6).

$$f(x,y,z,t) = f(i\Delta x, j\Delta y, k\Delta z, n\Delta t) = f^n(i,j,k) \tag{2.6}$$

where the subscripts i, j and k are integers representing spatial grid locations in the x, y and z direction respectively, and Δx, Δy and Δz are, respectively, the lattice space increments in the corresponding directions. Besides, the superscript n is an integer representing the increment of the time step Δt.

Then, the central-difference approximation of $f(x,y,z,t)$ about the first-order partial derivative of time and space domain can be described as in equation 2.7.

$$
\begin{aligned}
\frac{\partial f(x,y,z,t)}{\partial x}\Big|_{x=i\Delta x} &\approx \frac{f^n(i+\frac{1}{2},j,k) - f^n(i-\frac{1}{2},j,k)}{\Delta x} \\
\frac{\partial f(x,y,z,t)}{\partial y}\Big|_{y=j\Delta y} &\approx \frac{f^n(i,j+\frac{1}{2},k) - f^n(i,j-\frac{1}{2},k)}{\Delta y} \\
\frac{\partial f(x,y,z,t)}{\partial z}\Big|_{z=k\Delta z} &\approx \frac{f^n(i,j,k+\frac{1}{2}) - f^n(i,j,k-\frac{1}{2})}{\Delta z} \\
\frac{\partial f(x,y,z,t)}{\partial t}\Big|_{t=n\Delta t} &\approx \frac{f^{n+\frac{1}{2}}(i,j,k) - f^{n-\frac{1}{2}}(i,j,k)}{\Delta t}
\end{aligned}
\tag{2.7}
$$

Yee lattice

However, to better understand the FDTD algorithm, the basic Yee lattice is analyzed in detail. Figure 2.3 illustrates the standard Yee cell used for FDTD. It is possible to observe that every electric field component (E) is surrounded by four magnetic component (H), likewise, every electric magnetic component (H) is surrounded by four electric component (E). A three-dimensional space lattice is composed of a multiplicity of such Yee cells. An electromagnetic wave interaction structure is mapped into the space lattice by assigning appropriate values of permittivity to each electric field component (E), and permeability to each magnetic field component (H). Besides, electric and magnetic fields are sampled alternatively in the time sequence, with a sampling interval between them equal to half the time-step. In this way the Maxwell's curl equations become the explicit differential equations after discretization and can be solved by iterating in time without the necessary to

14

execute matrix inversion operations. As a consequence, FDTD method can solve the electromagnetic field spatial distribution at each time, step by step, by applying proper initial values.
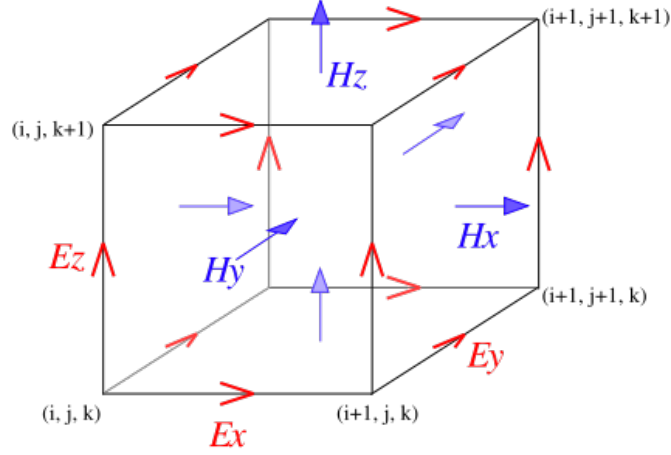
Figure 2.3.   Standard Yee cell for FDTD.

In Yee cell, the relationships between the grid points for the E-field and H-field components and the time step are shown in Table 2.1. The Yee algorithm also centers its E and H components in time in what is normally called a leapfrog arrangement. All of E computations in the modeled space are completed and stored in memory for a particular time point using previously stored H data. Then all of the H computations in the space are completed and stored in memory using the E data just computed. The cycle begins again with the re-computation of the H components based on the newly obtained E. This process continues until time-stepping is concluded. The calculation flow is shown in Figure 2.4.

electromagnetic fields	x-axis	y-axis	z-axis	time t sample.
E_x	$i + \frac{1}{2}$	j	k	n
E_y	i	$j + \frac{1}{2}$	k	n
E_z	i	j	$k + \frac{1}{2}$	n
H_x	i	$j + \frac{1}{2}$	$k + \frac{1}{2}$	$n + \frac{1}{2}$
H_y	$i + \frac{1}{2}$	j	$k + \frac{1}{2}$	$n + \frac{1}{2}$
H_z	$i + \frac{1}{2}$	$j + \frac{1}{2}$	k	$n + \frac{1}{2}$

Table 2.1.   The position of the E-field and H-field components in Yee cell.

15
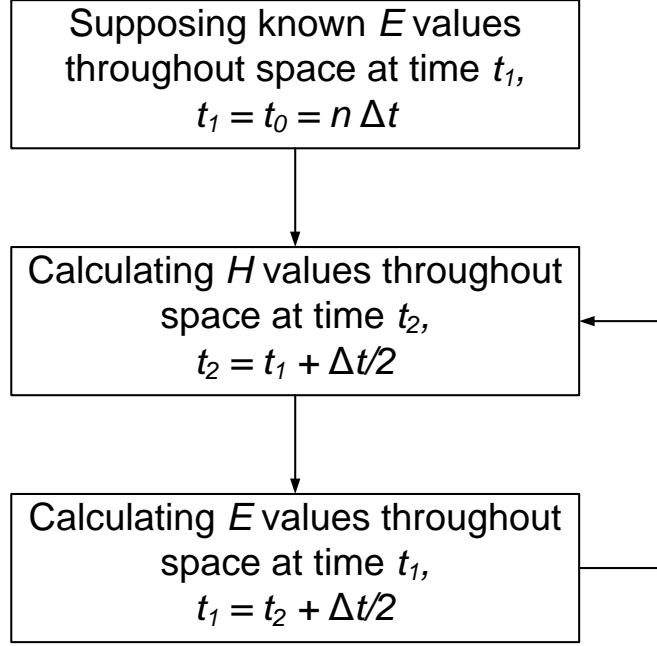
Figure 2.4.   Calculation flow chart of FDTD method.

Accordingly, the finite difference equations corresponding to (2.4) and (2.5), can be written as in equations (2.8) and (2.9) (supposing the observing point (x,y,z) is the grid point of E_x and H_x, which mean $(i + 1/2,j,k)$ at $(n + 1/2)\Delta t$ and $(i,j + 1/2,k + 1/2)$ at $n\Delta t$, respectively).

$$
\begin{aligned}
&\frac{H_z^{n+1/2}(i + \tfrac{1}{2},j + \tfrac{1}{2},k) - H_z^{n+1/2}(i + \tfrac{1}{2},j - \tfrac{1}{2},k)}{\Delta y} \\
&-\frac{H_y^{n+1/2}(i + \tfrac{1}{2},j,k + \tfrac{1}{2}) - H_y^{n+1/2}(i + \tfrac{1}{2},j,k - \tfrac{1}{2})}{\Delta z} \\
&= \varepsilon(i + \frac{1}{2},j,k)(\frac{E_x^{n+1}(i + \tfrac{1}{2},j,k) - E_x^n(i + \tfrac{1}{2},j,k)}{\Delta t}) \\
&\qquad\qquad +\sigma(i + \frac{1}{2},j,k)E_x^{n+\frac{1}{2}}(i + \frac{1}{2},j,k)
\end{aligned}
\tag{2.8}
$$

$$
\begin{aligned}
&\frac{E_z^n(i,j + 1,k + \tfrac{1}{2}) - E_z^n(i,j,k + \tfrac{1}{2})}{\Delta y} - \frac{E_y^n(i,j + \tfrac{1}{2},k + 1) - E_y^n(i,j + \tfrac{1}{2},k)}{\Delta z} \\
&= -\mu(i,j + \frac{1}{2},k + \frac{1}{2})(\frac{H_x^{n+1/2}(i,j + \tfrac{1}{2},k + \tfrac{1}{2}) - H_x^{n-1/2}(i,j + \tfrac{1}{2},k + \tfrac{1}{2})}{\Delta t}) \\
&\qquad\qquad -\sigma_m(i,j + \frac{1}{2},k + \frac{1}{2})H_x^n(i,j + \frac{1}{2},k + \frac{1}{2})
\end{aligned}
\tag{2.9}
$$

16

In the following (equation 2.10), the semi-implicit approximation method is applied. Since E_x values at time-step $n + 1/2$ and H_x values at time-step n are not assumed to be stored in the computer's memory (only the previous values of E_x at time-step n and H_x at time-step $n - 1/2$ are assumed to be stored in memory), a simple arithmetic average is taken between the stored values of E_x at time-step n and the yet-to-be computed new values of E_x at time-step $n + 1$, and similarly an average is taken between the stored values of H_x at time-step $n - 1/2$ and the yet-to-be computed new values of H_x at time-step $n + 1/2$.

$$H_x^n(i,j + \frac{1}{2},k + \frac{1}{2}) = \frac{H_x^{n+1/2}(i,j + \frac{1}{2},k + \frac{1}{2}) + H_x^{n-1/2}(i,j + \frac{1}{2},k + \frac{1}{2})}{2}$$

$$E_x^{n+1/2}(i + \frac{1}{2},j,k) = \frac{E_x^{n+1}(i + \frac{1}{2},j,k) + E_x^n(i + \frac{1}{2},j,k)}{2} \quad (2.10)$$

Equation (2.8) can be written equivalently as:

$$
\begin{aligned}
E_x^{n+1}(i + \frac{1}{2},j,k) &= CA(m) \cdot E_x^n(i + \frac{1}{2},j,k) \\
&+ CB(m) \cdot [\frac{H_z^{n+1/2}(i + \frac{1}{2},j + \frac{1}{2},k) - H_z^{n+1/2}(i + \frac{1}{2},j - \frac{1}{2},k)}{\Delta y} \\
&- \frac{H_y^{n+1/2}(i + \frac{1}{2},j,k + \frac{1}{2}) - H_y^{n+1/2}(i + \frac{1}{2},j,k - \frac{1}{2})}{\Delta z}]
\end{aligned}
\quad (2.11)
$$

where

$$CA(m) = \frac{\frac{\varepsilon(m)}{\Delta t} - \frac{\sigma(m)}{2}}{\frac{\varepsilon(m)}{\Delta t} + \frac{\sigma(m)}{2}} = -\frac{1 - \frac{\sigma(m)\Delta t}{2\varepsilon(m)}}{1 + \frac{\sigma(m)\Delta t}{2\varepsilon(m)}} \quad (2.12)$$

$$CB(m) = \frac{1}{\frac{\varepsilon(m)}{\Delta t} + \frac{\sigma(m)}{2}} = \frac{\frac{\Delta t}{\varepsilon(m)}}{1 + \frac{\sigma(m)\Delta t}{2\varepsilon(m)}} \quad (2.13)$$

where $m = (i + 1/2,j,k)$. Similarly, the other two equations in (2.4) can be written as:

$$
\begin{aligned}
E_y^{n+1}(i,j + \frac{1}{2},k) &= CA(m) \cdot E_y^n(i,j + \frac{1}{2},k) \\
&+ CB(m) \cdot [\frac{H_x^{n+1/2}(i,j + \frac{1}{2},k + \frac{1}{2}) - H_x^{n+1/2}(i,j + \frac{1}{2},k - \frac{1}{2})}{\Delta z} \\
&- \frac{H_z^{n+1/2}(i + \frac{1}{2},j + \frac{1}{2},k) - H_z^{n+1/2}(i - \frac{1}{2},j + \frac{1}{2},k)}{\Delta x}]
\end{aligned}
\quad (2.14)
$$

where $m = (i,j + 1/2,k)$, and

$$
\begin{aligned}
E_z^{n+1}(i,j,k + \frac{1}{2}) = \ & CA(m) \cdot E_z^n(i,j,k + \frac{1}{2}) \\
+ \ & CB(m) \cdot [\frac{H_y^{n+1/2}(i + \frac{1}{2},j,k + \frac{1}{2}) - H_y^{n+1/2}(i - \frac{1}{2},j,k + \frac{1}{2})}{\Delta x} \\
- \ & \frac{H_x^{n+1/2}(i,j + \frac{1}{2},k + \frac{1}{2}) - H_x^{n+1/2}(i,j - \frac{1}{2},k + \frac{1}{2})}{\Delta y}]
\end{aligned}
\tag{2.15}
$$

where $m = (i,j,k + 1/2)$.

Correspondingly, equation (2.9) and the other two equations in (2.5) can be written as:

$$
\begin{aligned}
H_x^{n+1/2}(i,j + \frac{1}{2},k + \frac{1}{2}) = \ & CP(m) \cdot H_x^{n-1/2}(i,j + \frac{1}{2},k + \frac{1}{2}) \\
- \ & CQ(m) \cdot [\frac{E_z^n(i,j + 1,k + \frac{1}{2}) - E_z^n(i,j,k + \frac{1}{2})}{\Delta y} \\
- \ & \frac{E_y^n(i,j + \frac{1}{2},k + 1) - E_y^n(i,j + \frac{1}{2},k)}{\Delta z}]
\end{aligned}
\tag{2.16}
$$

$$
\begin{aligned}
H_y^{n+1/2}(i + \frac{1}{2},j,k + \frac{1}{2}) = \ & CP(m) \cdot H_y^{n-1/2}(i + \frac{1}{2},j,k + \frac{1}{2}) \\
- \ & CQ(m) \cdot [\frac{E_x^n(i + \frac{1}{2},j,k + 1) - E_z^n(i + \frac{1}{2},j,k)}{\Delta z} \\
- \ & \frac{E_z^n(i + 1,j,k + \frac{1}{2}) - E_z^n(i,j,k + \frac{1}{2})}{\Delta x}]
\end{aligned}
\tag{2.17}
$$

$$
\begin{aligned}
H_z^{n+1/2}(i + \frac{1}{2},j + \frac{1}{2},k) = \ & CP(m) \cdot H_z^{n-1/2}(i + \frac{1}{2},j + \frac{1}{2},k) \\
- \ & CQ(m) \cdot [\frac{E_y^n(i + 1,j + \frac{1}{2},k) - E_y^n(i,j + \frac{1}{2},k)}{\Delta x} \\
- \ & \frac{E_x^n(i + \frac{1}{2},j + 1,k) - E_x^n(i + \frac{1}{2},j,k)}{\Delta y}]
\end{aligned}
\tag{2.18}
$$

where

$$
CP(m) = \frac{\frac{\mu(m)}{\Delta t} - \frac{\sigma_m(m)}{2}}{\frac{\mu(m)}{\Delta t} + \frac{\sigma_m(m)}{2}} = \frac{1 - \frac{\sigma_m(m)\Delta t}{2\mu(m)}}{1 + \frac{\sigma_m(m)\Delta t}{2\mu(m)}}
\tag{2.19}
$$

$$
CQ(m) = \frac{1}{\frac{\mu(m)}{\Delta t} + \frac{\sigma_m(m)}{2}} = \frac{\frac{\Delta t}{\mu(m)}}{1 + \frac{\sigma_m(m)\Delta t}{2\varepsilon(m)}}
\tag{2.20}
$$

where the label m is $(i,j + 1/2,k + 1/2)$, $(i + 1/2,j,k + 1/2)$, $(i + 1/2,j + 1/2,k)$ successively.

The finite-difference systems of (2.11), (2.14), (2.15), (2.16), (2.17) and (2.18) can be simplified if applied to a two-dimensional (2D) case. For 2D cases, if all physical quantities are not related to z-axis, all partial derivatives of the fields with respect to z are equal to zero, $\partial/\partial z = 0$. From (2.4) and (2.5) two independent sets can be identified, the sets of (E_z,H_x,H_y) components called TM wave and the sets of (H_z,E_x,E_y) components called TE wave.

On the basis of the above 3D condition, their finite difference schemes can be expressed in the following forms. For TE wave, $H_x = H_y = E_z = 0$, FDTD equations become:

$$
\begin{aligned}
E_x^{n+1}(i + \tfrac{1}{2},j) &= CA(m) \cdot E_x^n(i + \tfrac{1}{2},j) \\
&+ CB(m) \cdot \left[\frac{H_z^{n+1/2}(i + \tfrac{1}{2},j + \tfrac{1}{2}) - H_z^{n+1/2}(i + \tfrac{1}{2},j - \tfrac{1}{2})}{\Delta y}\right]
\end{aligned} \tag{2.21}
$$

$$
\begin{aligned}
E_y^{n+1}(i,j + \tfrac{1}{2}) &= CA(m) \cdot E_y^n(i,j + \tfrac{1}{2}) \\
&- CB(m) \cdot \left[\frac{H_z^{n+1/2}(i + \tfrac{1}{2},j + \tfrac{1}{2}) - H_z^{n+1/2}(i - \tfrac{1}{2},j + \tfrac{1}{2})}{\Delta x}\right]
\end{aligned} \tag{2.22}
$$

$$
\begin{aligned}
H_z^{n+1/2}(i + \tfrac{1}{2},j + \tfrac{1}{2}) &= CP(m) \cdot H_z^{n-1/2}(i + \tfrac{1}{2},j + \tfrac{1}{2}) \\
&- CQ(m) \cdot \left[\frac{E_y^n(i + 1,j + \tfrac{1}{2}) - E_y^n(i,j + \tfrac{1}{2})}{\Delta x}\right. \\
&- \left.\frac{E_x^n(i + \tfrac{1}{2},j + 1) - E_x^n(i + \tfrac{1}{2},j)}{\Delta y}\right]
\end{aligned} \tag{2.23}
$$

For TM wave, $E_x = E_y = H_z = 0$, FDTD equations become:

$$
\begin{aligned}
H_x^{n+1/2}(i,j + \tfrac{1}{2}) &= CP(m) \cdot H_x^{n-1/2}(i,j + \tfrac{1}{2}) \\
&- CQ(m) \cdot \left[\frac{E_z^n(i,j + 1) - E_z^n(i,j)}{\Delta y}\right]
\end{aligned} \tag{2.24}
$$

$$
\begin{aligned}
H_y^{n+1/2}(i + \tfrac{1}{2},j) &= CP(m) \cdot H_y^{n-1/2}(i + \tfrac{1}{2},j) \\
&+ CQ(m) \cdot \left[\frac{E_z^n(i + 1,j,k + \tfrac{1}{2}) - E_z^n(i,j,k + \tfrac{1}{2})}{\Delta x}\right]
\end{aligned} \tag{2.25}
$$

$$
\begin{aligned}
E_z^{n+1}(i,j) \;=\;& CA(m) \cdot E_z^n(i,j) \\
+\;& CB(m) \cdot \big[\frac{H_y^{n+1/2}(i+\tfrac{1}{2},j) - H_y^{n+1/2}(i-\tfrac{1}{2},j)}{\Delta x} \\
-\;& \frac{H_x^{n+1/2}(i,j+\tfrac{1}{2}) - H_x^{n+1/2}(i,j-\tfrac{1}{2})}{\Delta y} \big]
\end{aligned}
\qquad (2.26)
$$

where, the coefficients CA, CB, CP, CQ are the same of equations (2.11) (2.18), and m is the same with the grid position of the left-hand side of the corresponding equations.

The TM wave propagation will be used when 2D breast model is applied.

FDTD source

For FDTD simulations, correct modeling of sources is essential. There are two kinds of sources, voltage sources and current sources. Another classification of FDTD methods is possible based on the source modeling. Replaced source method, implemented by replacing the calculated component on a Yee-cell edge by the source at every time-step. Added source method, achieved by adding the source to the FDTD calculated component. Replaced sources may give rise to reflections of waves propagating back to the source location, while added sources act transparently to these incoming waves [15].

The modeling of FDTD voltage source is straightforward, due to the fact that the electric field E appears explicitly in the standard FDTD equations. The operation of replacing and adding to E with a source E is therefore explicit. However, modeling FDTD current sources is more complex because current is usually not explicitly included in the FDTD equations. The problem of where should the current source be placed in the Yee cell, and how should the current source be included in the FDTD equations should be taken into account.

In this application, current source is used as the FDTD source. The current source in the FDTD formulation is located on the edge of a Yee cell and added to the current density J in Maxwell's equation (2.1). Therefore, J in equation (2.1) becomes $\sigma E + J_s$ rather than σE, where J_s is the z-axis source current density averaged over the entire FDTD source cell. Considering TM wave, instead of (2.26), the electric field can be expressed as,

$$
\begin{aligned}
E_z^{n+1}(i,j) \;=\;& CA(m) \cdot E_z^n(i,j) \\
+\;& CB(m) \cdot \big[\frac{H_y^{n+1/2}(i+\tfrac{1}{2},j) - H_y^{n+1/2}(i-\tfrac{1}{2},j)}{\Delta x} \\
-\;& \frac{H_x^{n+1/2}(i,j+\tfrac{1}{2}) - H_x^{n+1/2}(i,j-\tfrac{1}{2})}{\Delta y} + J_s^{n+1/2}(i,j) \big]
\end{aligned}
\qquad (2.27)
$$

Other FDTD expressions in TM wave are unaffected by the current source. For more details please refer to [16].

CPML

Due to the limited amount of computer memory, FDTD computation only can be executed within finite computational domain. In order to model the electromagnetic scattering process efficiently and accurately, the artificial boundaries must be inserted into the simulation space. Meanwhile, attentions must be taken to minimize errors introduced by such boundaries. Instead of using highly effective absorbing boundary conditions (ABCs) to simulate an infinite unbounded computational domain, such as first and second order Mur ABC and Liao ABC, a special absorbing "material", called a perfectly matched layer (PML) is applied to implement absorbing boundaries in most modern FDTD implementations [17]. PML can provide orders-of-magnitude lower reflections than Mur and Liao ABC, but at the expense of added complexity. It is implemented by setting a kind of special medium layer at the FDTD truncation border, the wave impedance of this media is totally matched with the adjacent media, thus, the incident wave goes through the interface and goes into PML layer without any reflection. Moreover, due to the fact that PML layer is lossy medium, the transmitted wave which enters PML layer will attenuate rapidly. Even though PML has limited thickness, it still exhibits good absorbing effect for incident waves.

Since 1994, the original PML formulation has been modified and extended to the uniaxial PML (UPML), the convolutional PML (CPML), and the higher-order PML [18]. CPML is chosen as our absorbing boundary condition, due to its increased ability to absorb evanescent waves, therefore the absorbing layer can in theory be placed closer to a simulated scattering or radiating structure. CPML constructs the PML from an anisotropic, dispersive material, it does not require the fields to be split and can be implemented in a relatively straightforward manner. Authors in [19] have proved its effectiveness, besides, as compared to termination with a traditional formulation of the PML, the CPML technique has lead to a four-fold reduction in memory.

Figure 2.5 shows the schematic of a typical problem of equation waves propagation, where, in the region of interest analyzed, the radiated waves propagate at infinite (Figure 2.5 (a)). The same problem but with the addition of a layer of absorption (PML) to limit the area of analysis which does not create reflections is shown in Figure 2.5 (b).

In order to better understand the CPML technique, the general PML formulations are introduced first. Here, for sake of example, a lossy medium is assumed.
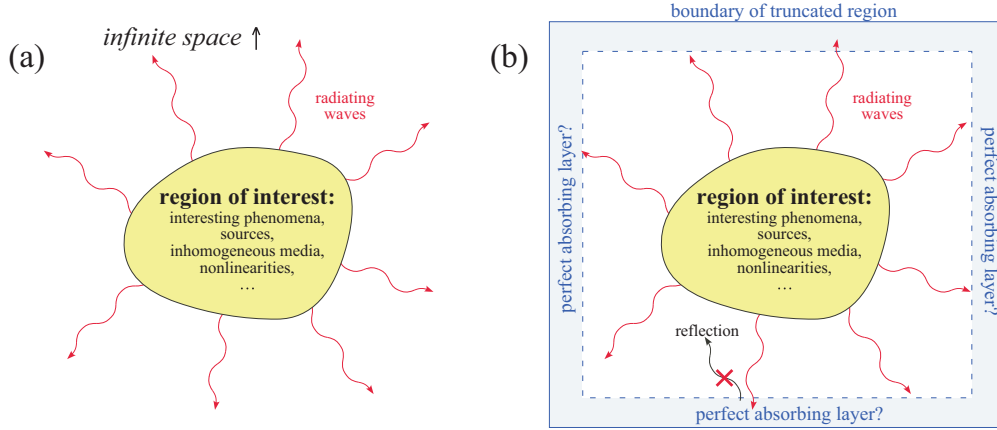
Figure 2.5. Schematic of a typical problem in the equation waves propagation, where, in the region of interest analyzed, the radiated waves propagate at finite in (a). The same problem but with the addition of a layer of absorption (PML) to limit the area of analysis which does not create reflections is shown in (b).

The x-projection of Ampere's law is thus specified as [19]:

$$j\omega\varepsilon E_x + \sigma E_x = \frac{1}{s_y}\frac{\partial H_z}{\partial y} - \frac{1}{s_z}\frac{\partial H_y}{\partial z} \tag{2.28}$$

where s_i are the stretched coordinate metrics, which was originally proposed by Berenger in [18]:

$$s_i = 1 + \frac{\sigma_i}{j\omega\varepsilon_0}, (i = x, y \text{ or } z) \tag{2.29}$$

Next, equation (2.28) is transformed to the time domain.

$$\varepsilon\frac{\partial E_x}{\partial t} + \sigma E_x = 1 + \overline{s_y}(t) * \frac{\partial H_z}{\partial y} - \overline{s_z}(t) * \frac{\partial H_y}{\partial z} \tag{2.30}$$

where $\overline{s_i}(t)$ is the inverse Laplace transform of s_i^{-1}.

The CPML technique is based on the writing of the PML model in the form of a convolution in time and on the introduction of memory variables to not have to explicitly store all the past states of the medium to carry out the convolution, but rather to calculate this convolution in a recursive way. The main idea of the CPML technique consists of making a choice for s_i more general than that of equation(2.29) by introducing not only σ_i, but also two other real variables $\alpha_i \geq 0$ and $\kappa_i \geq 1$ such that:

$$s_i = \kappa_i + \frac{\sigma_i}{\alpha_i + j\omega\varepsilon_0}, (i = x, y \text{ or } z) \tag{2.31}$$

In the particular case of $\kappa_i = 1$ and $\alpha_i = 0$, we get the classical PML coordinate transformation. Using Laplace transform theory, equation (2.30) becomes:

$$\varepsilon\frac{\partial E_x}{\partial t} + \sigma E_x = \frac{1}{\kappa_y}\frac{\partial H_z}{\partial y} - \frac{1}{\kappa_z}\frac{\partial H_x}{\partial z} + \zeta_y(t) * \frac{\partial H_z}{\partial y} - \zeta_z(t) * \frac{1}{\kappa_z}\frac{\partial H_x}{\partial z} \qquad (2.32)$$

The discrete impulse response for $\zeta_i(t)$ is defined as

$$\begin{aligned}
Z_{0_i}(m) &= \int_{m\Delta t}^{(m+1)\Delta t} \zeta_i(\tau)d\tau = -\frac{\sigma_i}{\varepsilon_0\kappa_i^2}\int_{m\Delta t}^{(m+1)\Delta t} e^{-(\frac{\sigma_i}{\varepsilon_0\kappa_i}+\frac{\alpha}{\varepsilon_0})\tau}d\tau \\
&= a_i e^{-(\frac{\sigma_i}{\kappa_i}+\alpha)\frac{m\Delta t}{\varepsilon_0}}
\end{aligned} \qquad (2.33)$$

where

$$a_i = \frac{\sigma_i}{(\sigma_i\kappa_i + \alpha_i\kappa_i^2)}\left(e^{-(\frac{\sigma_i}{\kappa_i}+\alpha_i)\frac{\Delta t}{\sigma_0}-1}\right) \qquad (2.34)$$

Using (2.33) and (2.34), (2.32) is discretized in both space and time according to a staggered Yee-scheme, leading to:

$$\begin{aligned}
\varepsilon&\frac{E_x^{n+1}(i+1/2,j,k) - E_x^n(i+1/2,j,k)}{\Delta t} + \sigma\frac{E_x^{n+1}(i+1/2,j,k) + E_x^n(i+1/2,j,k)}{2} \\
&= \frac{H_z^{n+1/2}(i+1/2,j+1/2,k) - H_z^{n+1/2}(i+1/2,j-1/2,k)}{\kappa_y\Delta y} \\
&\quad - \frac{H_y^{n+1/2}(i+1/2,j,k+1/2) - H_y^{n+1/2}(i+1/2,j,k-1/2)}{\kappa_z\Delta z} \\
&+ \sum_{m=0}^{N-1} Z_{0_y}(m)\frac{H_z^{n-m+1/2}(i+1/2,j+1/2,k) - H_z^{n-m+1/2}(i+1/2,j-1/2,k)}{\Delta y} \\
&- \sum_{m=0}^{N-1} Z_{0_z}(m)\frac{H_y^{n-m+1/2}(i+1/2,j,k+1/2) - H_y^{n-m+1/2}(i+1/2,j,k-1/2)}{\Delta z}
\end{aligned}$$
$$(2.35)$$

Due to the simple exponential form of $Z_{0_i}(m)$, sums in (2.35) can be performed recursively using the recursive convolution method.

$$\begin{aligned}
\varepsilon&\frac{E_x^{n+1}(i+1/2,j,k) - E_x^n(i+1/2,j,k)}{\Delta t} + \sigma\frac{E_x^{n+1}(i+1/2,j,k) + E_x^n(i+1/2,j,k)}{2} \\
&= \frac{H_z^{n+1/2}(i+1/2,j+1/2,k) - H_z^{n+1/2}(i+1/2,j-1/2,k)}{\kappa_y\Delta y} \\
&\quad - \frac{H_y^{n+1/2}(i+1/2,j,k+1/2) - H_y^{n+1/2}(i+1/2,j,k-1/2)}{\kappa_z\Delta z} \\
&\quad + \Psi_{e_{xy}}^{n+1/2}(i+1/2,j,k) - \Psi_{e_{xz}}^{n+1/2}(i+1/2,j,k)
\end{aligned}$$
$$(2.36)$$

where

$$
\begin{aligned}
\Psi_{e_{xy}}^{n+1/2}(i+1/2,j,k) \;=\;& b_y \Psi_{e_{xy}}^{n-1/2}(i+1/2,j,k) \\
+\;& a_y (H_z^{n+\frac{1}{2}}(i+1/2,j+1/2,k) - H_z^{n+\frac{1}{2}}(i+1/2,j-1/2,k))/\Delta y
\end{aligned}
\tag{2.37}
$$

$$
\begin{aligned}
\Psi_{e_{xz}}^{n+1/2}(i+1/2,j,k) \;=\;& b_z \Psi_{e_{xz}}^{n-1/2}(i+1/2,j,k) \\
+\;& a_z (H_y^{n+\frac{1}{2}}(i+1/2,j+1/2,k) - H_y^{n+\frac{1}{2}}(i+1/2,j-1/2,k))/\Delta z
\end{aligned}
\tag{2.38}
$$

$$
b_i = e^{-(\frac{\sigma_i}{\kappa_i}+a_i)\frac{\Delta t}{\varepsilon_0}}, (i = x, y, \text{ or } z)
\tag{2.39}
$$

This scheme is second-order accurate and is stable within the Courant limit for all positive real values of σ_i and α_i and for all real values of $\kappa_i \geq 1$.

The convolution terms are updated at each time step synchronously with the normal FDTD algorithm and, to reduce the errors of reflection in space discrete, the constitutive parameters $(\sigma_i, \alpha_i, \kappa_i)$ are scaled along the respective axes. In this way, the constitutive parameters have a one-dimensional variation, also a_i and b_i are one-dimensional functions that can be calculated in advance and stored in a vector, saving memory. The explicit update of the electric field (2.11) becomes:

$$
\begin{aligned}
E_x^{n+1}(i+\tfrac{1}{2},j,k) \;=\;& CA(m) \cdot E_x^n(i+\tfrac{1}{2},j,k) \\
+\;& CB(m) \cdot [\frac{H_z^{n+1/2}(i+\tfrac{1}{2},j+\tfrac{1}{2},k) - H_z^{n+1/2}(i+\tfrac{1}{2},j-\tfrac{1}{2},k)}{\kappa_y \Delta y} \\
-\;& \frac{H_y^{n+1/2}(i+\tfrac{1}{2},j,k+\tfrac{1}{2}) - H_y^{n+1/2}(i+\tfrac{1}{2},j,k-\tfrac{1}{2})}{\kappa_z \Delta z} \\
+\;& \Psi_{e_{xy}}^{n+1/2}(i+1/2,j,k) - \Psi_{e_{xz}}^{n+1/2}(i+1/2,j,k)]
\end{aligned}
\tag{2.40}
$$

Similar expressions are derived for the remaining electric and magnetic fields.

The basic structure of the CPML setting was displayed in Figure 2.5 (b). In FDTD computational region, Maxwell's equations are solved by standard FDTD algorithm, correspondingly, the computational region is surrounded by CPML layer, in which the equations are solved by the algorithms introduced above. The reflection coefficient is an important parameter for the evaluation of the CPML performance, it can be calculated as follows [16],

$$
R(\theta) = e^{-2\eta\sigma d\cos\theta}
\tag{2.41}
$$

where θ is the angle of incidence of the incident wave relative to the PML interface surface, d is the CPML layer thickness, η is wave impedance, σ is the conductivity in PML layer.

From (2.41) we know that $R(\theta)$ is a function of layer thickness and layer conductivity. In a FDTD simulation, $R(\theta)$ is taken as a reflection of error, so the bigger the product of d and σ, the smaller value of $R(\theta)$, the better performance of the CPML.

Due to the discrete nature of the FDTD algorithm, the discontinuities due to sampling artifacts must be compensated in some way. The change of the conductivity in PML layer is represented according to the following formula,

$$\sigma(x) = (x/d)^m \sigma_{max} \tag{2.42}$$

The conductivity grows from a zero value at the inner edge to a maximum value σ_{max} at the outer edge. It grows linearly when $m = 1$ and grows exponentially when $m > 1$. Combining the polynomial variation of the conductivity from (2.42) and (2.41) we obtain

$$R(\theta) = e^{-2\eta\sigma_{max}d\cos\theta/(m+1)} \tag{2.43}$$

In (2.43), a large m allows to obtain a distribution of $\sigma(x)$ flat near the interface of the CPML while for small m there is a more rapid growth $\sigma(x)$ inside of the absorbing layer. Generally, a value of $3 \leq m \leq 4$ allows to obtain good performance for most FDTD simulations [16].

With these assumptions, the parameters of a PML may easily be calculated to obtain a specific value of error, according to the following formula.

$$\sigma_{max} = -\frac{(m+1)\ln[R(0)]}{2\eta d} \tag{2.44}$$

By balancing the parameters in equation (2.45) an optimal efficiency of the CPML minimizing the discretization errors is obtained. Getting a low value of σ_{max}, it is possible to obtain a great reflection from the PEC wall set as boundary condition.

In this case, using dispersive materials, the CPML parameters must be suitably chosen to optimize the performance of our computational model, such as layer thickness and sigma attenuation factor. Following the literature [14] various tests to evaluate the correct values for the design were performed.

To sum up, the design flow for CPML can be organized as following:

- As a first choice we opted for an error of reflection $R(0)$, which brings us to write the following equation for calculating the optimal loss coefficient:

$$\sigma_{opt} = -\frac{0.8(m+1)}{\eta_0 \Delta \sqrt{\varepsilon_{r,eff}\mu_{r,eff}}} \tag{2.45}$$

where $\varepsilon_{r,eff}$ and $\mu_{r,eff}$ are the average value of the material parameters present at the edge of the main calculation area, and Δ is the space interval.

- The second parameter to be chosen is the thickness of the layer d. Based on the selected σ_{max} and typical values of m, κ_{max} and α_{max}, $\sigma(x)$ can be expressed as a function of d, which is the coefficient in the expression of a_i and b_i.

- Choosing a value of σ_{max} different from the optimal one to evaluate how further we can go to improve the performance.

These aspects will be evaluated from the practical point of view later.

Grid size and Stability

As FDTD technique represents Maxwell's curl equations with a set of finite difference equations, which means replacing the original solutions of electromagnetic partial differential equations with the solutions of finite difference equations. This kind of replacement is meaningful if and only if the solutions of the discrete difference equations are convergent and stable. Thus the limitation of time and space discrete intervals should be considered, from the stability and convergence of Maxwell's equations point of view.

For computational stability, it is necessary to satisfy the Courant stability conditions, in other words, the relationship between space interval Δx, Δy, Δz and time interval Δt:

$$c\Delta t \leq \frac{1}{\sqrt{\frac{1}{(\Delta x)^2} + \frac{1}{(\Delta y)^2} + \frac{1}{(\Delta z)^2}}} \tag{2.46}$$

where $c = 1/\sqrt{\varepsilon\mu}$ is the light speed in medium. This requirement puts a limitation on Δt for the chosen Δx, Δy and Δz.

Square Yee cells are adopted in this work for simplicity with $\Delta x = \Delta y = \Delta z = \Delta$. Authors in [16] introduced a Courant stability factor S to deal in a formal way with the time step choice. This factor is common to all numerical methods that have to deal with partial differential equations and must always be less than or equal to one to ensure stability. In 2D case the Courant factor is assumed to be 0.5, so, the time step Δt can be expressed as [16],

$$\Delta t = \frac{\Delta}{2c} \tag{2.47}$$

The value of spatial grid Δ in the FDTD grid is chosen to sufficiently sample the shortest wavelength in the system (normally determined by the bandwidth of the source), which means that over one increment the electromagnetic field does

not change significantly, and to accurately model the smallest dimension and/or physical and electromagnetic phenomenon in the simulated materials (such as skin depth, exchange length or domain wall width in a magnetic material). This means that, to have meaningful results, the linear dimension of the grid must be only a fraction of the wavelength (generally chosen between $\lambda/10$ and $\lambda/20$). In this application, for example, the considered maximum wave frequency is $10.6\,\mathrm{GHz}$, in free space, the calculated minimum wavelength is about $30\,\mathrm{mm}$, thus, the space interval must be smaller than $3\,\mathrm{mm}$ to obtain the accurate results.

2.1.2 Breast model

The "UWCEM Numerical Breast Phantom Repository" contains a fairly large number of numerical models of the breast anatomy derived from MRI scans with the patient in the prone position. They are used to investigate the methods for prevention of breast cancer and its treatment applications [20] [21]. Breast with ID: 012204 is selected as the investigated channel model, whose sagittal slice from the 3D numerical breast phantom is demonstrated in Figure 2.6. According to the radiographic density, this breast is classified as scattered fibroglandular who has 25-50% glandular tissue [20].
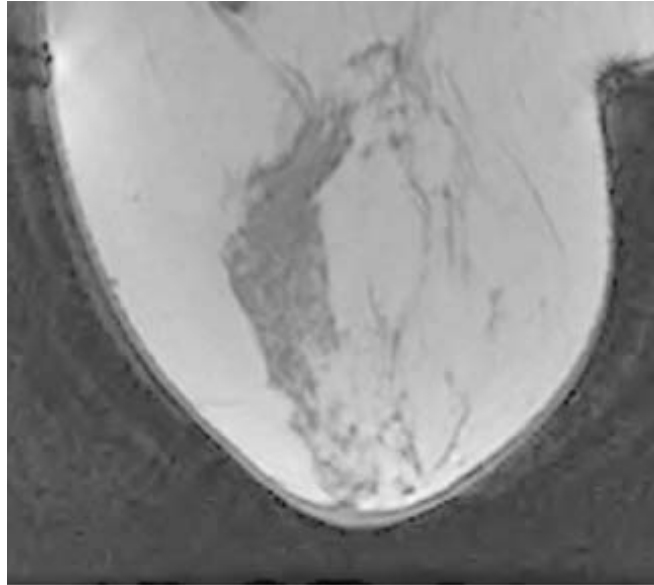
Figure 2.6.   MRI scans of the phantom in the repository UWCEM with Breast ID: 012204.

The phantom is comprised of a 3D grid of cubic voxels, where each voxel is $0.5\,mm \times 0.5\,mm \times 0.5\,mm$. The breast model consists of a roughly 1.5-mm-thick

skin layer, a 1.5-cm-thick subcutaneous fat layer at the base of the breast, and a 0.5-cm-thick muscle chest wall.

The included mediums in the breast model are illustrated in Table. 2.2, they are termed by media numbers. Except the skin and muscle medium, the normal breast tissues in the breast phantom are categorized into seven tissue types, ranging from the highest-water-content fibroconnective/glandular tissue with the highest dielectric properties (media number = 1.1), to the lowest-water-content fatty tissue with the lowest dielectric properties (media number = 3.3). There is also a transitional region with media number 2 which represents intermediate dielectric properties [20]. The dielectric properties information for each voxel of the breast interior are given.

tissue type	media number.
external Environment	-1
skin	-2
muscle	-4
glandular1	1.1
grandular2	1.2
glandular3	1.3
transitional	2
fat1	3.1
fat2	3.2
fat3	3.2

Table 2.2.   Type of fabric and the corresponding average number [20]

As microwave imaging technique for breast cancer detection application is based on the principle that the dielectric properties contrast between malignant tissue and normal tissue is significant, recently published data in [22] [23], based on a large clinical study, report the realistic dispersive dielectric properties of normal breast tissue in the extremely wide frequency range of 0.5 to 20 GHz, and suggest that the contrast between healthy and malignant breast tissues might be not as high as previously believed.

Dispersive medium

Since most human tissues are dispersive medium, it is necessary to take the dispersive effect into account to approach the actual case. In this study, the dispersive properties of breast tissues were also included in our FDTD breast models. The dispersive breast is modeled by setting different dispersive electrical properties for the breast fat, the skin, the chest wall and the tumor.

Figure 2.7 shows the eight wideband dielectric properties curves that serve as upper and lower bounds on each of the seven types of normal breast tissue listed in Table 2.2 from 0.5 to 20 GHz [20] [22].
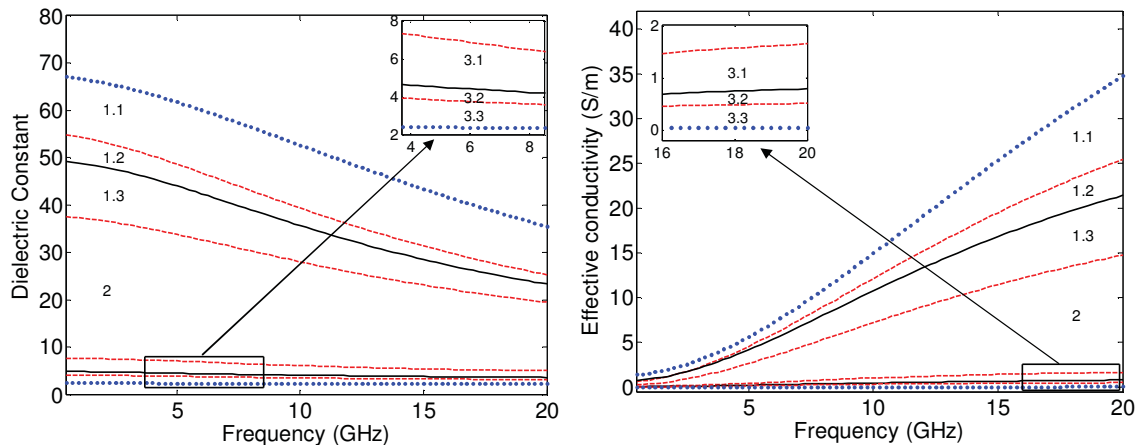
Figure 2.7. The seven tissue-type regions bounded by the curves in this graph are labeled with the media numbers reported in Tab. 2.2. From top to bottom, the curves correspond to the following eight cases: maximum, group1-high, group1-median, group1-low, group3-high, group3-median, group3-low, and minimum [20].

The frequency dependence of tissue dielectric properties is more promptly incorporated into wideband FDTD simulations using Debye dispersion parameters rather than Cole-Cole parameters [20]. The frequency dependence of the dielectric constant, $\varepsilon(\omega)$, and the conductivity, $\sigma(\omega)$, over the band of interest (3 GHz to 10 GHz) was accurately modeled using single-pole Debye dispersion equations of the following form:

$$\varepsilon(\omega) - j\frac{\sigma}{\omega\varepsilon_0} = \varepsilon_\infty + \frac{\varepsilon_s - \varepsilon_\infty}{1 + j\omega\tau} - j\frac{\sigma_s}{\omega\varepsilon_0} \qquad (2.48)$$

In this model, ω is the angular frequency, $\sigma/\omega\varepsilon_0$ is the frequency-dependent dielectric loss, ε_∞ defines the relative permittivity at infinite frequency, ε_s is the static relative permittivity, σ_s is the static conductivity, and τ is the relaxation time constant. τ can be approximated by a single known spatially independent value since the relaxation time constant in the microwave frequency range is similar (e.g., on the order of 10 ps) for various different biological tissues [24]. Consequently, there are three unknowns for this equation (ε_∞, ε_s and σ_s) at every voxel within the volume. These three model parameters can be estimated from the experimental data.

Here, in Table 2.3, the parameters for single-pole Debye models over the 3-10 GHz band are presented, which are used in the above introduced FDTD simulations

29

[16]. A constant relaxation time constant $\tau = 13\,ps$ for all tissue types is used, $\Delta\varepsilon = \varepsilon_s - \varepsilon_\infty$.

	ε_∞	$\Delta\varepsilon$	$\tau(ps)$	$\sigma_s(s/m)$
minimum	2.309	0.092	13.00	0.005
group3-low	2.848	1.104	13.00	0.005
group3-median	3.116	1.592	13.00	0.050
group3-high	3.987	3.545	13.00	0.080
group1-low	12.99	24.40	13.00	0.397
group1-median	13.81	35.55	13.00	0.738
group1-high	14.20	40.49	13.00	0.824
maximum	23.20	46.05	13.00	1.306
skin	15.93	23.83	13.00	0.831
muscle	21.66	33.24	13.00	0.886

Table 2.3. Single-pole Debye parameters for the maximum, group1-high, group1-median, group1-low, group3-high, group3-median, group3-low, and minimum curves associated with normal breast tissue as well as skin and muscle (valid for the 3-10 GHz band) [20].

Figure 2.8 shows the single-pole Debye curves for normal breast tissue along with their corresponding Cole-Cole curves, to illustrate the accuracy of the Debye models over the 3-10 GHz band. Debye parameters for specific voxels within the breast were computed using a weighted average based on the p value of a specific voxel [16]. It is possible to note that the weighted averages are applied to the Debye parameters themselves rather than the frequency-specific dielectric constant and conductivity [20].

Investigated breast model

Figure 2.9 shows the result of three-dimensional (3D) pre-processing at a given frequency of 8 GHz.

However, as the first step, a two dimensional (2D) breast model was used as our channel model, which is shown in Figure 2.10. It is the sagittal slice of the 3D breast model of Figure 2.9. The chest wall was included, and the model was terminated by a complementary perfectly matched layer (CPML). A fake tumor (the black square) is inserted in the FDTD models, while the Debye parameters for the tumor are $\varepsilon_\infty = 3.9$, $\Delta\varepsilon = 50.1$, $\tau = 13\,ps$ and $\sigma_s = 0.7\,S/m$. A conformal array consisting of 9 antenna elements is located on the surface of the naturally flattened breast, the antenna in the FDTD model is the hertzian dipole antenna which is modeled as an electric current sources [16].
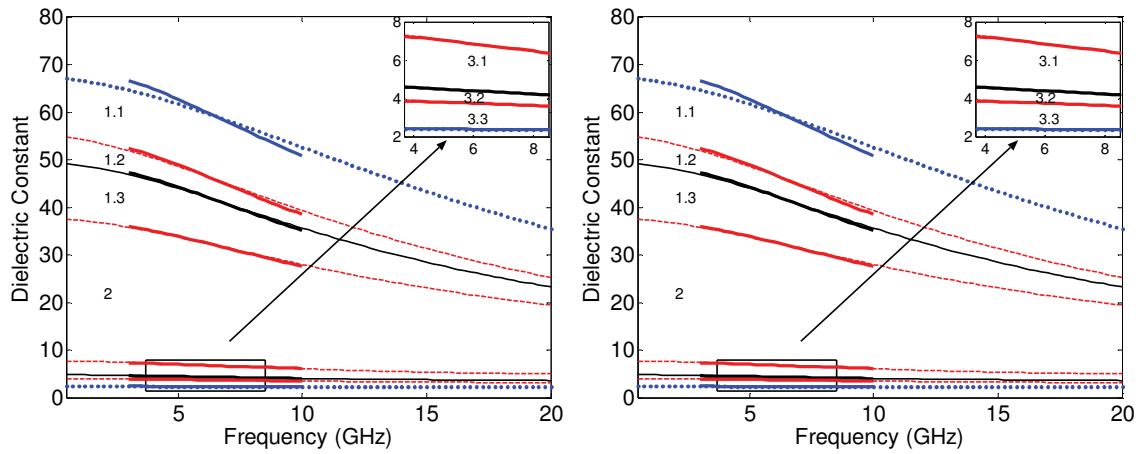
Figure 2.8. From top to bottom, the Cole-Cole and Debye (bold) curves correspond to the following eight cases: maximum, group1-high, group1-median, group1-low, group3-high, group3-median, group3-low, and minimum [20].
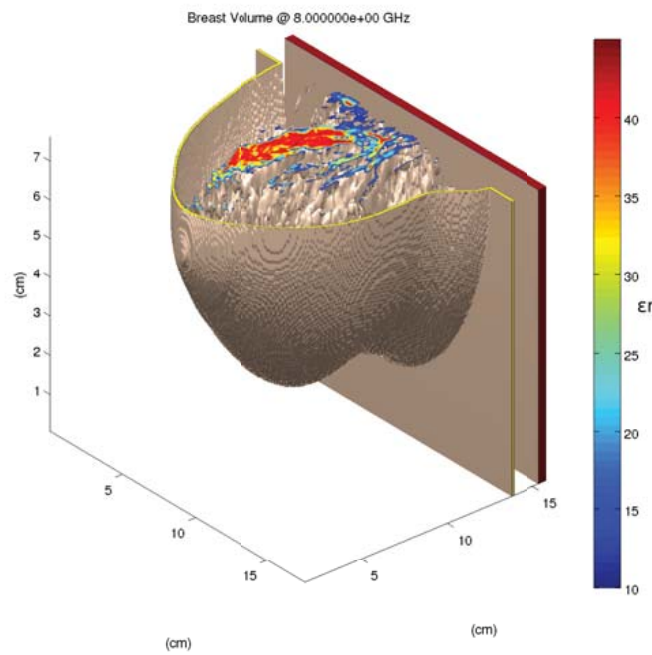
Figure 2.9. Dielectric constant–three dimensional model.

Another breast model was created using the average properties technique, with the same size and shape with above heterogeneous breast, but with constant breast tissue [25]. The ideal model is used to decouple the effect of a complex breast

31
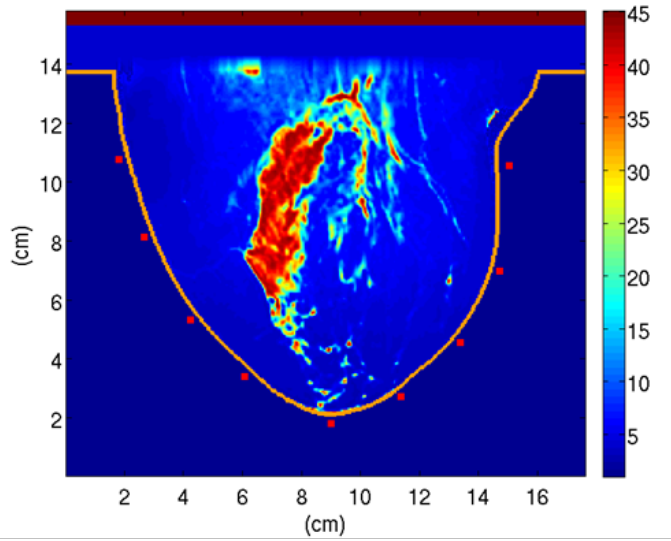
Figure 2.10.   Heterogeneous breast model.

from the effect of system non-idealities when we evaluate the system functionality. The real model is used for a final assessment, when we evaluate the two effects combined. Figure 2.11 depicts this homogeneous breast model. Table 2.4 shows the spatial averages of the Debye parameters for each phantom in our application.
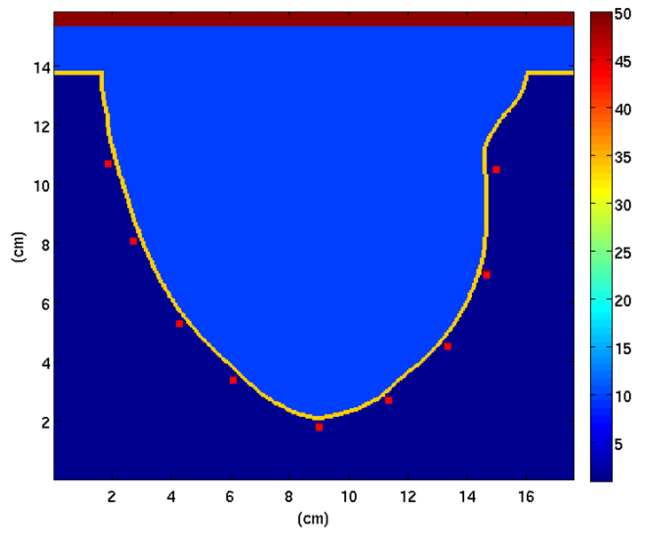
Figure 2.11.   Homogeneous breast model.

32

	ε_∞	$\Delta\varepsilon$	$\tau(ps)$	$\sigma_s(s/m)$
skin	4	33	13.00	1.1
normal tissues	7	3	13.00	0.15
muscle	4	50	13.00	0.7
tumor	3.9	50.1	13.00	0.7

Table 2.4.   Average breast tissue single-pole Debye parameters for each phantom.

As mentioned above, the spatial grid resolution for FDTD simulation is 0.5 mm, which is accurate enough for the breast modeling. Using the 2D model, combined with equation (2.47), the calculated time step is 0.834 ps, which is about 1200 GHz sampling frequency.

2.2   Front-end: Transceiver and Antenna

The aim of the front-end is data transmission and acquisition. The UWB imaging system is expected to be suitable for long term, continuous monitoring purposes, so that low cost is one of the important characteristic to promote the development of microwave imaging techniques for breast cancer detection. Even experiments with standard RF instruments have proved that the microwave imaging technique is capable of detecting small tumors [26]. The required experimental instruments, like Vector Network Analyzer and the switching network, are bulky and expensive, so they should be replaced by low cost integrated circuits and systems.

The block diagram of the proposed front-end is shown in Figure 2.12. It is composed of the array of transceivers and antennas. Transceivers are the chain that connects the antennas on one side and signal processing section on the other side. In this specific application, the purpose of the hardware is to send a pulse train toward the breast through antenna, detect and sample the particular type of reflected pulse train, caused by the interface between the different breast tissues, and then convert it to digital signal. Based on the radar configuration, a circulator or switch may need to select between connecting the antenna to the transmitter and to the receiver. Moreover, the isolation between transmitter and receiver can not be ignored.

2.2.1   Transmitter

The transmitter part is conceptually simple. It works as a pulse generator, and should be able to generate any type of sub-nanosecond pulse in the band chosen for application to breast cancer detection. Ideally, it is modeled in Matlab as a single source point in FDTD simulation. An integrated and flexible CMOS UWB
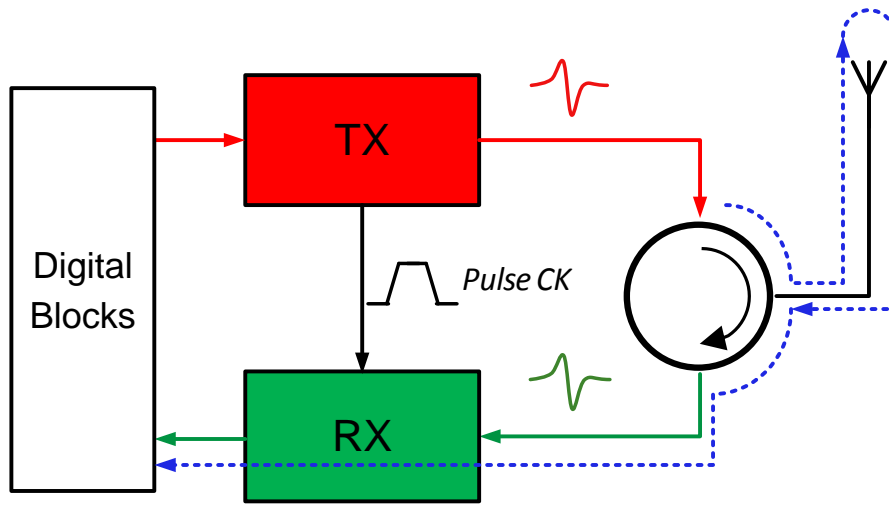
Figure 2.12. Block diagram of RF frontend.

transmitter architecture based on the distributed-waveform generator technique have proposed and developed [27] [28]. The block diagram is presented in Figure 2.13.
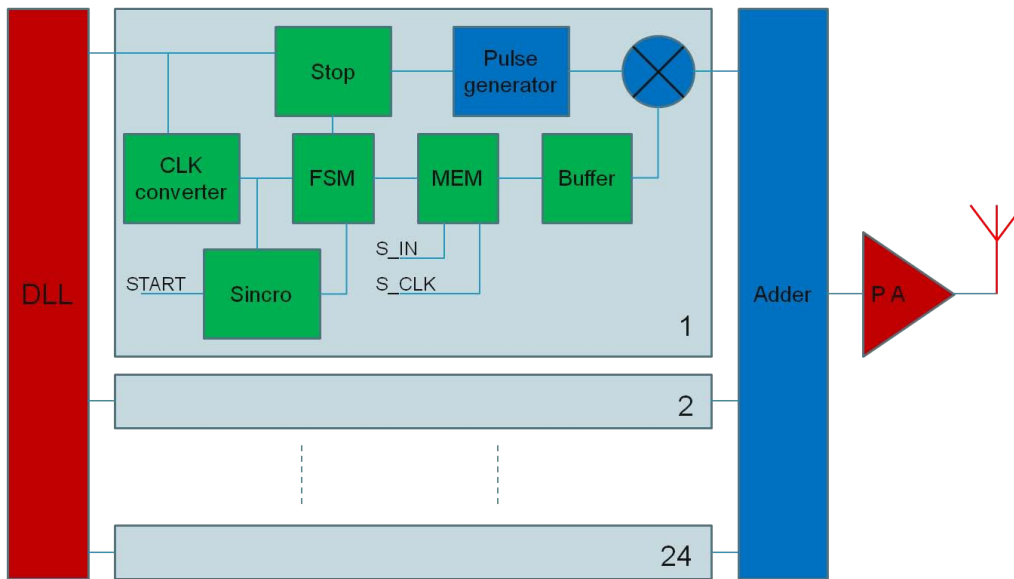
Figure 2.13. Block diagram of the transmitter [27].

2.2.2 Receiver

The receiver is an important block and a design challenge in our microwave imaging application, as the requirements of the receiver are very strict in this application, given that it has to satisfy the input matching with the antenna, minimize the noise distortion within the specific ultra-wide bandwidth (up to 10 GHz), while achieving at the same time very large dynamic ranges. Similarly to the transmitter, the receiver is modeled as a perfect cell under ideal condition. The focus will be focused on the implementation of the receiver part later.

2.2.3 Antenna

Antennas are located around and close to the breast, and each antenna is connected to a transceiver pair. In the ideal model that we use as a reference, the antenna is ideally modeled as a hertzian dipole during FDTD simulation [16]. Figure 2.14 shows the ideal radiation pattern of the typical Hertzian dipole antenna. In addition, a custom-designed slot antenna was also experimented, as will be discussed later on.
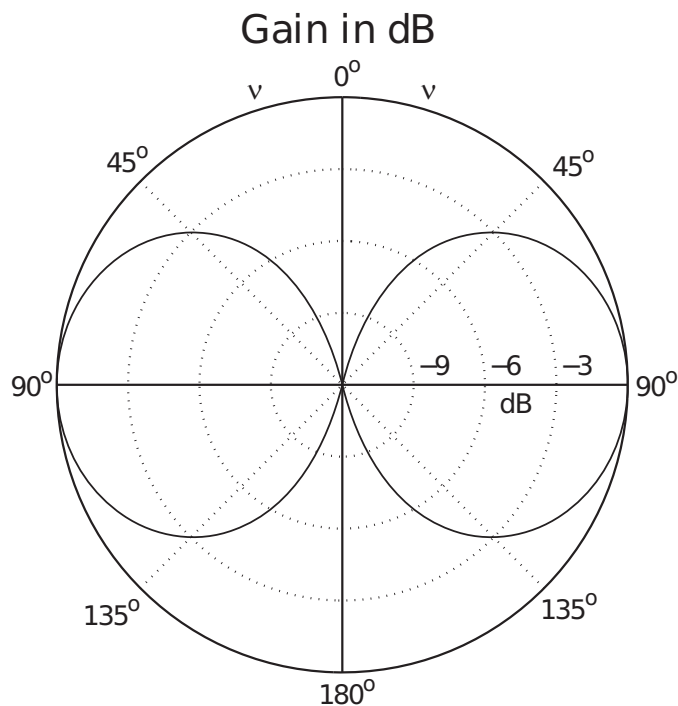
Figure 2.14. Diagram of emission of a Hertzian dipole antenna [16].

2.3   Algorithm and implementation

The aim of the image reconstruction unit is, starting from the sampled reflected signals, to recombine this values in order to obtain an energy map representing the amount of energy backscattered from each point of the breast.

Depending on how the backscattered energy is acquired, there are several different approaches to UWB radar imaging. These approaches can be divided into three categories: monostatic, bistatic, and multistatic. In the monostatic case, the transmitting antenna itself acquires the backscattered signal. Often the transmitting antenna is moved across the breast to produce a synthetic aperture. In the bistatic configuration, two antennas are used, a single transmitting antenna and a single receiving antenna. At last, in the multistatic approach, the tissue is illuminated by one transmitting antenna while the backscattered signals are recorded at several antennas placed at different positions around the breast [29]. Figure 2.15 explains better these configurations. Multistatic and Bistatic configurations offer better performance at the expense of increased implementation complexity.
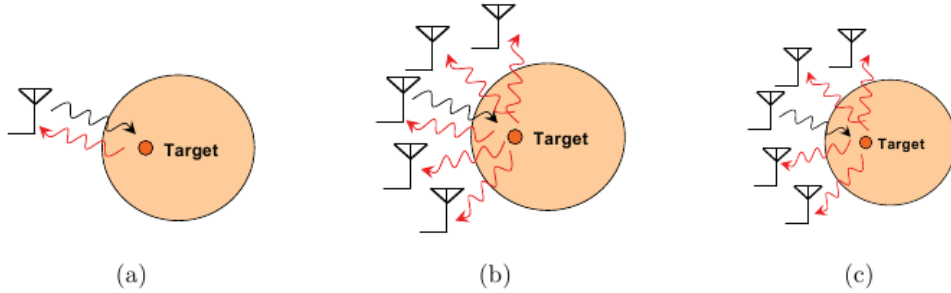
Figure 2.15.   Possible configurations with Radar Microwave Imaging: (a) Monostatic, (b) Multistatic, (c) Bistatic.

Based on different radar configurations, various imaging algorithms have been proposed, like Confocal Microwave Imaging(CMI) [5], Time Reversal(TR) [30], Generalized Likelihood Ratio Test(GLRT) [31], multistatic adaptive microwave imaging(MAMI) [29], delay-multiply-and-sum (DMAS) [32] and Microwave Imaging via Space-Time(MIST) [33] [34]. The monostatic radar method is applied in this breast cancer detection system for its simplicity; moreover, the MIST beamforming algorithm has proved to be a better technique for the application [35].

To better understand the imaging reconstruction process, CMI technique will also be introduced, which is the most simple algorithm for detecting breast cancer.

2.3.1 Confocal Microwave Imaging

Confocal Microwave Imaging employs a simple delay-and-sum (DAS) beamforming algorithm. Figure 2.16 shows the basic principle of CMI, antenna array is located around breast surface. The antennas detect all the points in breast, the delay types are the same at the same points. The received signals at different antenna positions are shown in the central panel. It is possible to see that the time delay of the received pulse by different antennas is different, and the sum of all delayed waveforms gives us an information about dielectric contrast in that point. When the beamformer is steered to location r_0 (the actual location of the tumor), the signals coherently sum, as shown by the left panel, the resulting signal will be big. Correspondingly, when the beamformer is steered to a location other than r_0, incoherent summation results, as shown by the right panel, the energy will be smaller. More in detail, the
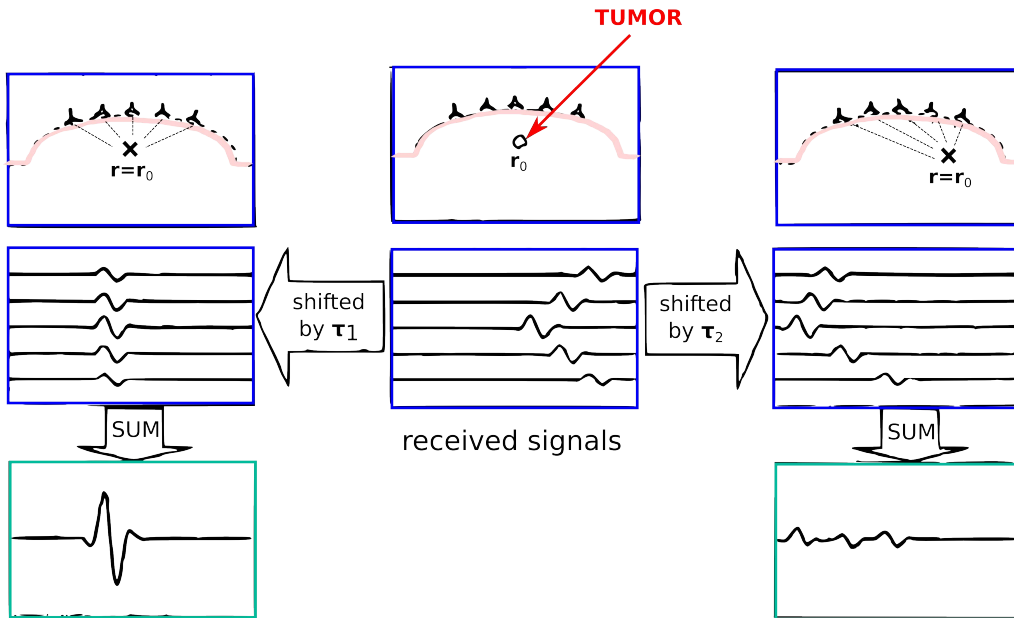
Figure 2.16. An illustration of simple delay-and-sum beamforming. The received signals are shown in the central panel. When the beamformer is steered to location r_0 (the actual location of tumor), the signals coherently sum, as shown by the left panel. When the beamformer is steered to a location other than r_0, incoherent summation results, as shown by the right panel [34].

implementation of this algorithm can be divided into four steps [5].

1. Calibration. This is the first and fundamental step prior to performing tumor detection, not only for CMI technique, but for all imaging techniques. The goal of the calibration step is to remove the incident pulse and skin backscatter

from the recorded waveforms, as the response from the skin-breast interface is orders of magnitude larger than the response from all other contributions and may persist in time beyond the time at which the lesion response occurs. Supposing the distance between antenna and breast skin is identical, so the signals recorded at various antenna locations have identical incident pulse and skin backscatter content. Moreover, as the distance of antenna-to-skin is smaller than the distance of antenna-to-tumor, the skin reflection appears earlier than tumor information. The calibration operation is implemented generating a calibration signal for each antenna by averaging the time response of every other antenna. The calibration is completed subtracting the signal from the corresponding antenna.

2. Integration. The next step in the signal processing is the integration of the calibrated signals. The differentiated Gaussian excitation signal has a zero-crossing at its center point in time. The backscattered signal that would follow after a specific time delay corresponding to the round-trip distance between the antenna and the scatterer would also have a zero-crossing at its center point. After integration, the signal would have a maximum at the center point, allowing for the coherent addition of local maxima via straightforward time-shifting.

3. Compensation. Compensation for radial spreading and/or path loss is applied to the signals. Radial spreading correction accounts for the decrease in amplitude of a spherical wave as it expands, while path loss compensation corrects for the reduction in signal strength due to propagation through lossy breast tissue.

4. Image Reconstruction. It consists on calculating, for each pixel, its intensity. First, the round trip time (τ_{ii}) from each antenna to the considered pixel ($|\vec{r} - \vec{r_i}|$) is calculated. In this calculation, the wave velocities (v) of the different covered mediums (air, skin, healthy breast tissue) are taken into account. Then, the time-domain signals are time-shifted by an amount corresponding to the calculated round-trip times. In this way, the information on the considered pixel embedded in the various time-domain signals is aligned [35]. The round-trip time is calculated by

$$\tau_{ii}(\vec{r}) = \frac{2|\vec{r} - \vec{r_i}|}{v \Delta t} \tag{2.49}$$

The intensity of a pixel in the reconstructed image is the square of the coherently summed values.

$$I(\vec{r}) = \left[\sum_{i=1}^{NRX} w_i \mathbf{a}_{ii}(\tau_{ii}(\vec{r})) \right]^2 \tag{2.50}$$

where the weights w_i are introduced to compensate for the radial spreading of each cylindrical wave as it propagates outward from the transmitting antenna.

However, this algorithm does not account for dispersive propagation effects and offers limited capability for discriminating against artifacts and noise. In the following, MIST beamforming algorithm, along with an advanced algorithm for optimal removal of skin artifacts are analyzed.

2.3.2 MIST

Since antennas may be located at slightly different (sub-millimeter) distances from the skin, it is clear that the above introduced calibration procedure is effective as long as each antenna has the same distance from the skin. More sophisticated algorithms should be employed to estimate the correct distance and efficiently remove the skin content.

The MIST imaging system can be divided into two main processing stages: preprocessing that eliminates the large reflection at the skin (skin artifact removal), optimal beamforming (MIST beamforming). The structure of this MIST imaging system is demonstrated in Figure 2.17, n is the number of antennas, n channels are used in skin artifact removal part, and then MIST beamforming processes the calibrated n signals and reconstructs the energy map, N is the antenna number. Details of each of these stages are described below.
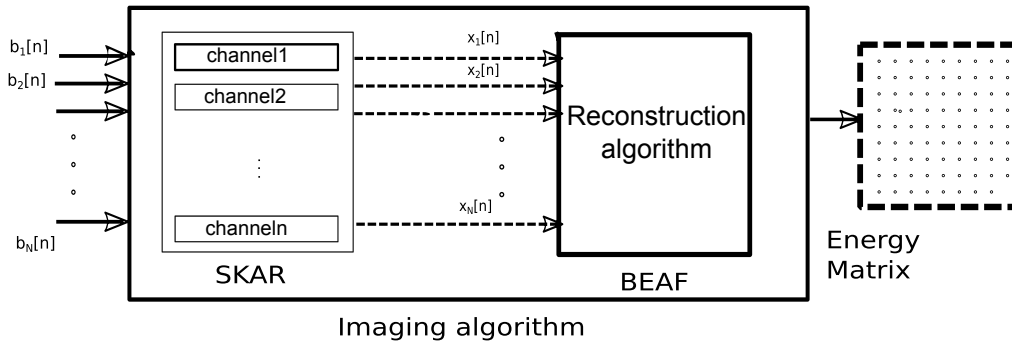
Figure 2.17. Structure of the reconstruction algorithm organized in two parts: skin artifact removal (SKAR) and MIST beamforming (BEAF).

Skin Artifact Removal

Skin artifact removal (SKAR) is an algorithm for optimally removing artifacts in the received signals due to backscatter from the skin-breast interface [33]. Compared

with the above mentioned calibration, this approach takes into account the local variations in skin thickness and breast heterogeneity.

The general idea behind this approach is simple. It estimates the skin artifact at each antenna as a filtered combination of the signals at all other antennas to compensate for channel-to-channel variation. The filter weights are chosen to minimize the residual signal over the initial portion of the received data, which is dominated by the backscatter from the skin interface. Figure 2.18 shows the block diagram of this algorithm.
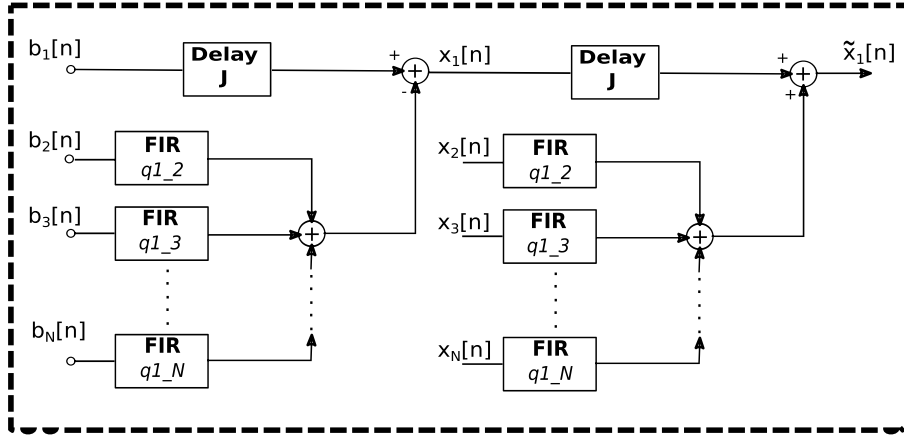
Figure 2.18.   Block diagram illustrating the algorithm for removing the skin-breast artifact from the backscattered signal received at the first of N antennas [35].

Without loss of generality, suppose that the skin-breast artifact is to be removed from the first antenna. Considering an array of N_{ant} receiving antennas, we denote the nth received sample at the ith antenna as $b_i[n]$. Starting to analyze the block for the first antenna, the skin contribute on sample n^{th} is estimated from a window $\mathbf{b}_i[n]$ of length $2J+1$ centered on the nth sample in each other $N_{ant} - 1$ channel:

$$\mathbf{b}_i[n] = [b_i[n-J],..,b_i[n],..,b_i[n+J]]^T \quad 2 \le i \le N_{ant} \qquad (2.51)$$

$$\mathbf{b}_{2N}[n] = [\mathbf{b}_2[n]^T,..,\mathbf{b}_N[n]^T]^T \qquad (2.52)$$

Vector $\mathbf{b}_{2N}[n]$ is obtained as the merging of windows from channel 2 to channel N_{ant}. The filter weights vector is denoted as $\mathbf{q}_i$ and concatenation of coefficients from channels 2 through N_{ant} is $\mathbf{q} = [q_2^T....q_N^T]^T$.
The residual part of signal is computed subtracting the sum from all filtered windows to the n-sample of first antenna:

$$x_1[n] = b_1[n] - \mathbf{q}^T\mathbf{b}_{2N}[n] \qquad (2.53)$$

This operation is repeated for each channel. If received data are decomposed in skin ($s[n]$) and residual ($d[n]$) contributions a distortion occurs in the residual part of each signal:

$$x_1[n] = s_1[n] - \mathbf{q}^T \mathbf{s}_{2N}[n] + d_1[n] - \mathbf{q}^T \mathbf{d}_{2N}[n]$$
$$\approx d_1[n] - \mathbf{q}^T \mathbf{d}_{2N}[n] \tag{2.54}$$

$\mathbf{d}_{2N}[n]$ can be approximated by using $\mathbf{x}_{2N}[n]$. Taking into account this approximation, the compensation is performed using the following formula:

$$\tilde{x}_1[n] = x_1[n] + \mathbf{q}^T \mathbf{x}_{2N}[n] \tag{2.55}$$

In order to obtain the coefficients, a specific procedure is requested, and is reported here. Filter weights are chosen to satisfy the constraints of equation (2.56),

$$\mathbf{q} = arg \min_q \sum_{n=n_0}^{n_0+m-1} |b_1[n] - \mathbf{q}^T \mathbf{b}_{2N}[n]|^2 \tag{2.56}$$

where the time interval $n = n_0$ to $n_0 + m - 1$ represents the initial portion of the data record containing skin-breast artifact and no backscattered signals from lesions. In other words, coefficients are chosen to nullify part of signal dominated by unwanted skin reflection and direct path, delimited by n_0 and $n_0 + m - 1$. Solution to this kind of problem requests a least square method solution. This minimization problem can be solved by:

$$\mathbf{q} = \mathbf{R}^{-1} \cdot \mathbf{p} \tag{2.57}$$

$$\mathbf{p} = \frac{1}{m} \sum_{n=n_0}^{n_0+m-1} \mathbf{b}_{2N}[n] b_1[n] \tag{2.58}$$

$$\mathbf{R} = \frac{1}{m} \sum_{n=n_0}^{n_0+m-1} \mathbf{b}_{2N}[n] \mathbf{b}_{2N}^T[n] \tag{2.59}$$

An issue with this kind of solution is that the signals in specified time interval have high similarity, which leads to have matrix $\mathbf{R}$ ill-conditioned. Weights obtained have large norm and amplify noise. To prevent this, low-rank approximation R_p is used in place of R. Matrix inversion becomes:

$$\mathbf{R}_p = \sum_{i=1}^{p} \lambda_i \mathbf{u}_i \mathbf{u}_i^T \tag{2.60}$$

$$\mathbf{R}_p^{-1} = \sum_{i=1}^{p} \frac{1}{\lambda_i} \mathbf{u}_i \mathbf{u}_i^T \tag{2.61}$$

41

where λ_i, $1 \leq i \leq p$, are the p most significant $\mathbf{R}$ eigenvalues and $\mathbf{u}_i$, $i \leq i \leq p$, are the corresponding eigenvectors.

Therefore, the design flow can be simply organized as follows:

1. Choosing the starting sample n_0 and the number of the processed samples m. It is correct to think that only these m samples will contain skin artifact.

2. Choosing a window has a length of $2J + 1$ for theses m samples.

3. Calculating the filter weights and calibrating these chosen m samples to get the residual parts of the received signals.

4. Compensating the calculated residual parts.

An example of the SKAR effect on the signal is shown in Figure 2.19. The backscattered signals are from antenna, obtained by a FDTD simulation. The solid pulse is acquired at the condition when tumor is inserted, the dotted pulse is without tumor. The zoomed part includes tumor information, it is invisible, as the skin reflection part is too big. The bottom figure shows the pulses after the SKAR application, it is possible to see that the big skin reflection parts are eliminated and the tumor information part is kept and became clear (compare the superposition between two signals obtained in a case without tumor and with tumor). The importance and effectiveness of this stage is therefore evident.

MIST Beamforming

Following the skin artifact removal, the calibrated signals $\widetilde{x}_1[n]$ to $\widetilde{x}_N[n]$ are then passed through the MIST beamformer.

The image of backscattered energy as a function of scan location is obtained by applying a space-time beamformer designed for each scan location to the backscattered signals measured at each antenna. Figure 2.20 shows the space-time beamformer for each scan location forms a weighted combination of time-delayed versions of the backscattered signals. The aim of this section is to design the beamformer to keep the backscattered signals from the designed point while attenuating contributions from other locations.

Similarly to other beamforming techniques, the MIST beamforming algorithm, or "BEAF", is based on time aligning of signals from different antennas in order to adjust different round trips time ($\tau_i(r_0)$) from antennas to a generic point r_0. In this way, if a dielectric discontinuity, such as malignant tumor, exists at r_0, the time-aligned signals add coherently and the energy response will be large. The MIST block diagram is shown in Figure 2.20.

FDTD Simulation: Received Signal Before Calibration

(a)

FDTD Simulation: Received Signal After Calibration

(b)
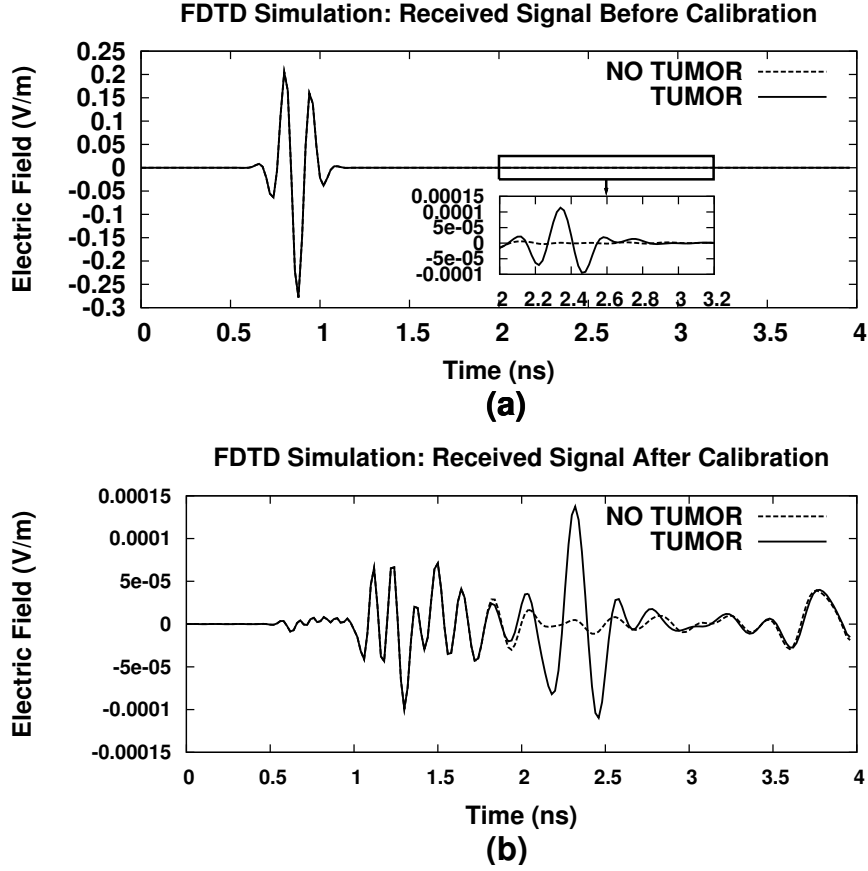
Figure 2.19. Example of pulses before and after calibration. FDTD-computed backscattered signals with and without tumor as received by one of the antennas, with zoom on the late-time response, showing a difference between the two signals. (b) Signal after calibration, the skin artifacts are removed.

Remembering that the distances between each antenna and point r_0 may not be the same. First of all, time-aligning is performed, as suggested in [33] [35], by delaying the waveform by an integer number $n_i(r_0)$:

$$n_i(r_0) = n_a - round(\tau_i(r_0)) \quad n_a \geq round(\max_{i,r_0} \tau_i(r_0)) \tag{2.62}$$

where n_a is the worst case round-trip over all channels and locations.

Then, the aligned signal is truncated by a window function $g[n]$ to remove the samples before n_a which are not useful for energy estimation.

$$g[n] = \begin{cases} 1, & n \geq n_a \\ 0, & \text{otherwise} \end{cases} \tag{2.63}$$

43
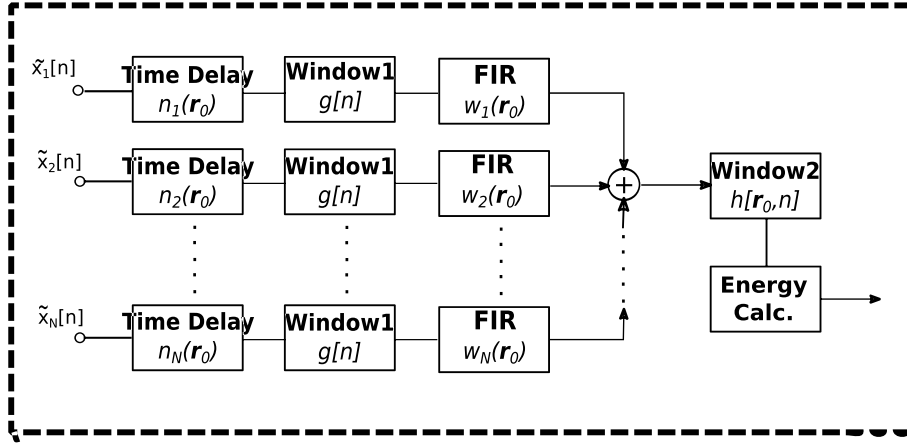
Figure 2.20. Block diagram illustrating the MIST beamforming process for location r in the breast [33].

Before summing the outputs, the FIR filters are needed to compensate the frequency-dependent propagation effects, such as attenuation and dispersion of breast tissues related to the path length. If w_{il} is defined as the lth weight of ith filter, the summed output from these filters can be expressed as [35]:

$$z[n,\mathbf{r}_0] = \sum_{i=1}^{N} \sum_{l=0}^{L} w_{il} \cdot \tilde{x}_i[n - l - n_i(r_0)] \qquad (2.64)$$

where L is the number of weights in each channel. The calculation of filter weights will be introduced later. It is necessary to notice that the performance will be better with more filter weights, but the design complexity will increase too, so the weights number must be chosen by carefully exploring this trade-off.

Before calculating the voxel energy, another window h with length of l_h is defined to choose the useful samples which contain the tumor information.

$$h[n,\mathbf{r}_0] = \begin{cases} 1, & n_h \leq n \leq n_h + l_h \\ 0, & \text{otherwise} \end{cases} \qquad (2.65)$$

Finally, the energy $p(\mathbf{r}_0)$ is obtained as the sum of the squares of $z[n]$ windowed by $h[n,\mathbf{r}_0]$:

$$p(\mathbf{r}_0) = \sum_{n} |z[n]h[n,\mathbf{r}_0]|^2 \qquad (2.66)$$

Weights of FIR filters can be computed in time-domain [33] [35] or frequency-domain [36] [37]. Frequency-domain approach is applied for its computationally simplicity, as it does not require matrix inversion.

The frequency resolution for weights design $\Delta\omega$ is:

$$\Delta\omega = \frac{2\pi}{LT_s} \tag{2.67}$$

As mentioned above, it is limited by maximum length of FIR filter L. T_s is the sampling time interval.

The band of interest is composed of the set of K frequencies starting form a lower bound ω_l to an upper-bound ω_h:

$$\omega_l = \omega_0 \le \omega_k \le \omega_{K-1} = \omega_h \quad : \quad 0 \le k \le K - 1 \tag{2.68}$$

Then, supposing to choose ω_l and ω_h multiple of frequency step $\Delta\omega$, K is equal to:

$$K = \frac{\omega_h - \omega_l}{\Delta\omega} + 1 \tag{2.69}$$

For a monostatic configuration, the backscattered signal in frequency domain $B_i(\omega)$ is:

$$B_i(\omega_k) = I(\omega_k)S_{ii}(\omega_k,\mathbf{r}_0) \tag{2.70}$$

where $I(\omega_k)$ is the portion of the transmitted signal belonging to the kth frequency in UWB range of transmitted signal. Each value $S_{ii}(\omega_k,\mathbf{r}_0)$ corresponds to the ideal scattering value in frequency domain for each voxel. In a monostatic configuration $S_{ii}(\omega_k,\mathbf{r}_0)$ can be formulated by considering radial spreading, path loss and phase shift. Depending on if the scanning is performed in 2D or 3D space, the formulas are:

$$
\begin{aligned}
S_{ii}(\omega_k,\mathbf{r}_0) &= \left[\frac{1}{|\mathbf{r}_0 - \mathbf{r}_i|} e^{-\alpha(\omega_k)|\mathbf{r}_0 - \mathbf{r}_i|} e^{-\beta(\omega_k)|\mathbf{r}_0 - \mathbf{r}_i|} \right]^2 \qquad \text{3D} \\
S_{ii}(\omega_k,\mathbf{r}_0) &= \left[\frac{1}{|\mathbf{r}_0 - \mathbf{r}_i|^{0.5}} e^{-\alpha(\omega_k)|\mathbf{r}_0 - \mathbf{r}_i|} e^{-\beta(\omega_k)|\mathbf{r}_0 - \mathbf{r}_i|} \right]^2 \qquad \text{2D}
\end{aligned}
\tag{2.71}
$$

$\alpha(\omega)$ is attenuation factor for path loss and $\beta(\omega)$ is phase constant for phase shift. They are functions of dielectric properties of the medium considering also dielectric losses (the same used in FDTD simulation algorithms) [35].

Since the filter weights are designed to have unit gain and linear phase response, the following relationship is obtained.

$$I(\omega_k) \sum_{i=1}^{M} S_{ii}(\omega_k,\mathbf{r}_0) e^{j\omega_k \lfloor \tau_i(\mathbf{r}_0)/T_s \rfloor T_s} W_i^*[k,\mathbf{r}_0] = e^{-j\omega_k \tau_0} \tag{2.72}$$

The linear phase term $e^{j\omega_k \lfloor \tau_i(\mathbf{r}_0)/T_s \rfloor T_s}$ represents the coarse time alignment, while $\tau_0 = (L-1)T_s/2$ is the average time delay introduced by the filters.

The above formula can be divided into two parts, one is $\mathbf{V}(\omega_k,\mathbf{r}_0)$ which denotes combination of pulse shape, propagation and coarse time alignment effects, the other is $\mathbf{W}[k,\mathbf{r}_0]$ that is the vector of weights associated to each signal at a given frequency.

$$
\begin{aligned}
\tilde{S}_{ii}(\omega_k,\mathbf{r}_0) &= S_{ii}(\omega_k,\mathbf{r}_0)e^{j\omega_k\lfloor\tau_i(\mathbf{r}_0)/T_s\rfloor T_s} \\
\mathbf{V}(\omega_k,\mathbf{r}_0) &= I(\omega_k)\{\tilde{S}_{ii}(\omega_k,\mathbf{r}_0)\}_{i=1}^{N}
\end{aligned}
\tag{2.73}
$$

$$
\mathbf{W}[k,\mathbf{r}_0] = \{[W_i[k,\mathbf{r}_0]\}_{i=1}^{N}
\tag{2.74}
$$

Formula (2.72) can be rewritten as:

$$
\mathbf{W}^H[k,\mathbf{r}_0]\mathbf{V}(\omega_k,\mathbf{r}_0) = e^{-j\omega_k\tau_0}
\tag{2.75}
$$

Therefore, the weights calculated by this frequency-domain method can be expressed as:

$$
\mathbf{W}[k,\mathbf{r}_0] = \frac{\mathbf{V}(\omega_k,\mathbf{r}_0)e^{j\omega_k\tau_0}}{\mathbf{V}^H(\omega_k,\mathbf{r}_0)\mathbf{V}(\omega_k,\mathbf{r}_0)}
\tag{2.76}
$$

However, this result is prone to amplify noise because weights can become very large when $\mathbf{V}^H(\mathbf{r}_0,\omega_k)\mathbf{V}(\mathbf{r}_0,\omega_k)$ is small. This situation occurs, particularly at higher frequencies and deeper locations, due to greater attenuation values for $S_{ii}(\omega_k,\mathbf{r}_0)$. This problem was studied and discussed in [37], a penalized least-squares approach was applied. Basically, equation (2.75) is solved as:

$$
\begin{aligned}
\mathbf{W}[k,\mathbf{r}_0] = arg \min_{\mathbf{W}[k,\mathbf{r}_0]} \{ & |\mathbf{W}^H[k,\mathbf{r}_0]\mathbf{V}(\omega_k,\mathbf{r}_0) - e^{-j\omega_k\tau_0}|^2 + \\
& \xi\mathbf{W}^H[k,\mathbf{r}_0]\mathbf{\Lambda}[k,\mathbf{r}_0]\mathbf{W}[k,\mathbf{r}_0]\}
\end{aligned}
\tag{2.77}
$$

Second term controls noise gain, where matrix $\mathbf{\Lambda}[k,\mathbf{r}_0]$ represents the penalty structure and ξ is positive parameter, it is used to scale the impact of penalty. Various kind of matrix $\mathbf{\Lambda}[k,\mathbf{r}_0]$ can be chosen to perform this operation. As discussed in [37] and verified in [35], in a comparison between identity matrix, diagonal matrix and square diagonal matrix, the second one resulted to be the best choice for the case in analysis. The calculated weights are:

$$
W_i[k,\mathbf{r}_0] = \frac{V_i(\omega_k,\mathbf{r}_0)e^{j\omega_k\tau_0}}{|V_i(\omega_k,\mathbf{r}_0)|(\xi + \sum_{j=1}^{N}|V_{jj}(\omega_k,\mathbf{r}_0)|)}, \qquad \mathbf{\Lambda}_{ii}[k,\mathbf{r}_0] = |V_i[k,\mathbf{r}_0]|
\tag{2.78}
$$

Finally, FIR filter weights are computed by performing IFFT of $W_i[k,\mathbf{r}_0]$ to produce a set of vectors of size L.

For other skin artifact removal and beamforming algorithms, please refer to [35].

2.3.3   Quality factors

To evaluate the results obtained during the simulation, it is not sufficient to observe the reconstructed map. Quality factors are used for the evaluation of performance in addition to the observation of the outcomes.

- **SMR** - Ratio between maximum value into the backscattered energy matrix in case of tumor (rec_T) and average inbreast energy points $rec_{T,ave}$. The formula is:

$$\mathbf{SMR} = 10 \cdot log \frac{max(rec_T)}{rec_{T,ave}} \tag{2.79}$$

  The maximum energy value is supposed to be the tumor response. If this is not true, this value become meaningless.

- **SCR** - The maximum value of backscattered energy in the tumor region (rec_T) divided by the maximum value found elsewhere (rec_T'). The formula is:

$$\mathbf{SCR} = 10 \cdot log \frac{max(rec_T)}{rec_T'} \tag{2.80}$$

- **MAXPOS** - Maximum energy position in the map: if the maximum point is near to theoretical, the beamformer has detected tumor.

For the definitions presented here, the tumor can be thought as detected if and only if SMR and SCR are greater than $10\,dB$ and $0\,dB$, respectively, as well an energy peak appears at the correct tumor position.

Chapter 3

System setting and verification

The purpose in this chapter is to build the entire system using the models developed in previous chapters, that is, the transmitter for pulse generation, the antennas for transmitting and receiving signals, the 2D channel model represented by the breast and the surrounding environment, the receiver, and the imaging unit(IU), and then to analyze the system feasibility. In this chapter, all simulations are ideally performed by Matlab, in other words, the transmitters, receivers and antennas are included in FDTD simulation. Therefore, the block scheme and design flow is illustrated in Figure 3.1.
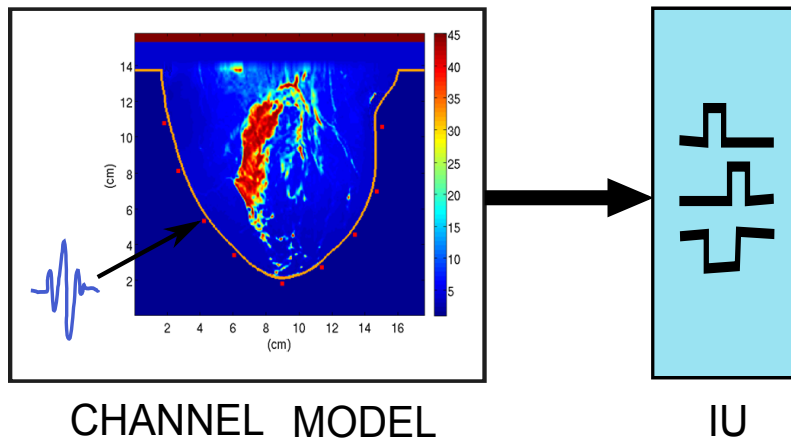
Figure 3.1. Block scheme of imaging system and design flow.

3.1   System parameters

Before performing any simulation, the system parameters should be defined. Firstly, the parameters of the 2D numerical breast model are organized here: the effective breast size is 158 mm×176 mm, the depth of the skin layer is 1.5 mm, the spatial grid resolution is 0.5 mm, the FDTD time step is $0.834\,ps$, the sampling frequency is around 1200 GHz. After that, the performance of the Convolution Perfect Match Layer (CPML) is evaluated. Based on the defined breast model parameters, the suitable setting for CPML can be found. A set of simulations have been performed to choose the optimal CPML parameters for the specific 2D breast model, especially the thickness of the CPML absorbing layer d [16]. To this end, a coefficient, error relative to the reference solution, was computed as a function of time using [16]:

$$Rel.error^n(i,j) = |E^n(i,j) - E^n_{ref}(i,j)|/|E_{ref,max}(i,j)| \qquad (3.1)$$

where $E^n(i,j)$ represents the time-dependent discrete electric field computed within the working volume, $E^n_{ref}(i,j)$ represents the same discrete electric field computed by the reference problem, and $E_{ref,max}(i,j)$ represents the maximum value of the electric field in the given reference probe point over the full time simulation.

The reflection error versus time for different dimension of CPML is illustrated in Figure 3.2. It is possible to observe that $d = 16$ is a good choice to compromise the performance and execution time (refer to [16] for more details).

Moreover, the effect of antenna and transceiver is also included in FDTD simulation, both of them are ideally modeled. Figure 3.3 presents the proposed FDTD simulation environment, a conformal dipole antenna and transceiver array consisting of 9 elements modeled as electric-current sources is located around the surface of the breast, the distance between each antenna and skin is 2 mm. A 16-layer CPML surrounds the breast model. A small square in the breast is a fake tumor, which is inserted in the numerical model during the FDTD simulation. The tumor size selection will be analyzed later.

As introduced in Chapter 2, SKAR calibration and MIST beamforming algorithm are used to reconstruct a microwave scattering image of the interior of the breast. First of all, since UWB pulses are applied, based on the Nyquist criterion, the sampling frequency must be greater than two times signal frequency (10.6 GHz), therefore, the sampling frequency of beamformer is set to be 50 GHz [33]. The grid resolution of beamforming is 1 mm, which must be a multiple of FDTD spatial resolution. Based on them, other design parameters for SKAR and MIST beamforing are evaluated [35].

Furthermore, in order to process the reflected signals from FDTD simulation, the signals are decimated from a sampling frequency of 1200 GHz to 50 GHz.
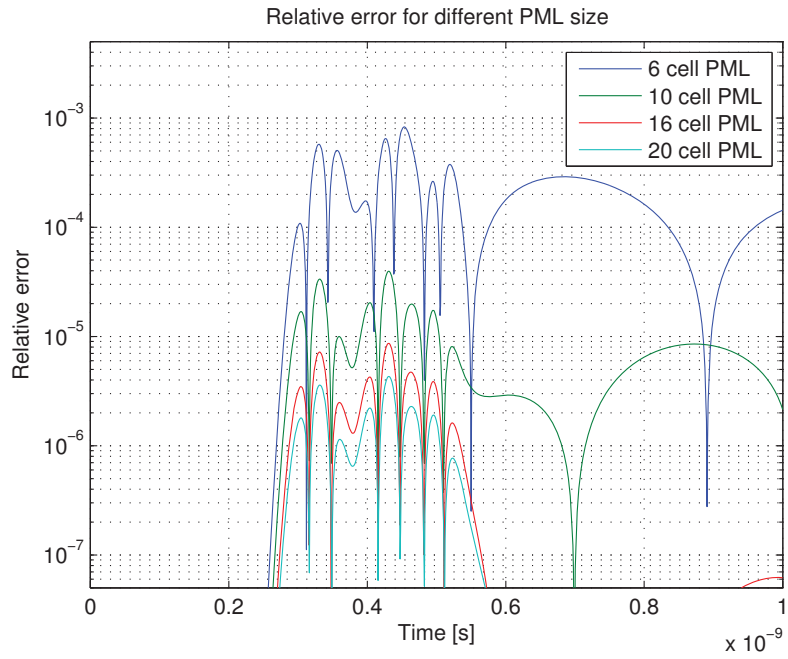
Figure 3.2.   The reflection error versus time for different dimension of CPML [16].
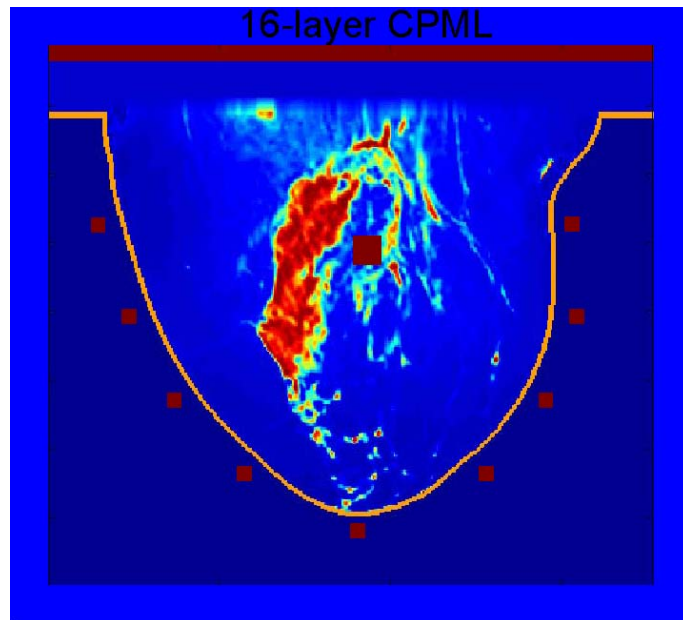
Figure 3.3.   The breast model in FDTD simulation.

3.2 Source pulses

In this section, the last important component for executing the imaging system simulation, the exciting source, is introduced. As the characteristic of radar imaging approach, the signal bandwidth related to the resolution and penetration depth. The higher the signal frequency, the higher the radar profile resolution, but the more attenuation displayed by the body tissues, impairing the capability of detecting a deeper target. Consequently, penetration depth and spatial resolution need to be properly balanced by the choice of the operating frequencies. This discussion is important because different types of UWB signals generate different backscattered responses and then it is possible to obtain imaging reconstructions with different properties.

In UWB waveforms, impulsive type pulses typically have a wavelength less than $1\,\mathrm{ns}$ and a bandwidth greater than gigahertz. A brief discussion about three commonly used impulse types for breast cancer detection application is included here.

3.2.1 Modified Hermite Pulse (MHP)

The *Modified Hermitian Pulse* (MHP) are defined as [38]:

$$h_n(t) = k_n e^{-t^2/4\tau^2} h_{e,n}(t) \tag{3.2}$$

The value k_n defines the energy of the signal, n defines the derivative order of the polynomial, τ represents the width time of the pulse and the sequence is orthogonal. The MHP has the following properties [38] [39]:

- The duration of the pulse is roughly the same for all values of n.

- The bandwidth of the pulse is approximately the same for all values of n.

- The pulses are mutually orthogonal.

- The pulses do not have a DC component equal to zero, and in fact the low-frequency component is relatively significant.

- The number of steps for the coordinate zero is equal to n.

Figure 3.4 represents the first-order ($n = 1$) MHP signals in time domain and frequency domain, the pulse width τ is equal to $150\,\mathrm{ps}$. The spectral analysis shows a center frequency equal to 750MHz and a $3\,\mathrm{dB}$ bandwidth extends to $1.2\,\mathrm{GHz}$. This MHP pulse is a relative low frequency source, which can achieve high penetration depth, but low range resolution.
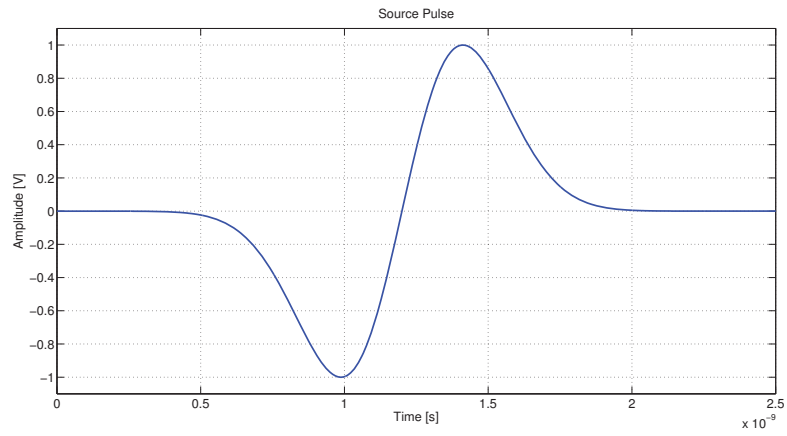
(a)
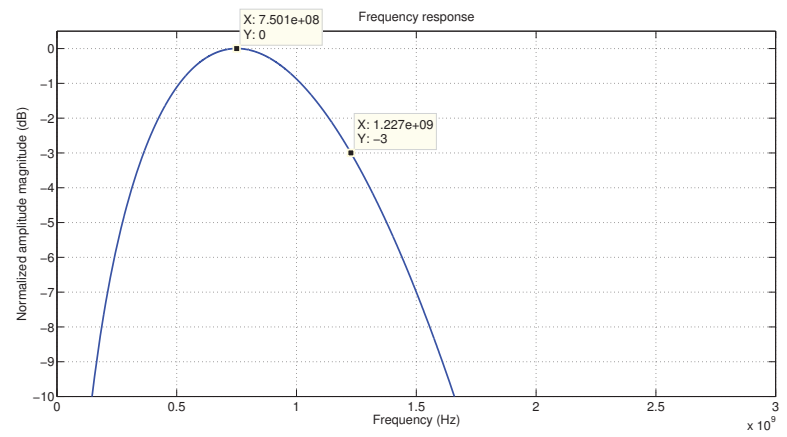
(b)

Figure 3.4.   MHP used for simulations: a) time domain b) frequency domain [16].

3.2.2 Modulated and Modified Hermite Pulse (MMHP)

The Modulated and Modified Hermite Pulses (MMHP) are another candidate model for the UWB signals, which are used to investigate the effect of excitation pulses on the microwave imaging qualities. It was designed in [30] in order to obtain high resolution map using Time Reversal algorithm. As suggested by the name, they are obtained by performing a modulation of MHP sequence. The obtained MMHP pulses are expressed as,

$$p_n(t) = \sqrt{2} h_n cos(2\pi f_c t + \phi_r) \tag{3.3}$$

The modulation carrier is f_c and ϕ_r is a phase term.

Authors in [30] have indicated that MMHP has more oscillations than MHP with the same pulse width. Unlike MHP, MMHP has zero DC component, but, as the same as MHP, both the duration and bandwidth remain the same for pulses of different orders. Figure 3.5 displays the time domain and frequency domain of this MMHP signals with $\tau = 40\,\mathrm{ps}$, $f_c = 8\,\mathrm{GHz}$, $n = 8$. Figure 3.5 (b) shows that more spectral components go up to a maximum frequency of 18GHz.

A higher signal frequency of MMHP allows to obtain a higher spatial resolution compared to the case MHP and a greater sensitivity is in the tumor masses of small dimensions. However, due to the lower frequency of the main lobe respect to the following differential gaussian pulse, an higher penetration depth but less resolution is obtained, as possible to verify in [16].

3.2.3 Differential Gaussian pulse (DG)

Differential gaussian pulse is the most frequently used impulse type in literature for UWB applications [40] [33]. It has a zero-crossing at its center point in time. This pulse is obtained modulating the Gaussian Monocycle pulse and the equation is [16]:

$$y_{DG}(t) = sin(2\pi f_c t) \cdot \frac{t}{\tau} \cdot e^{-\frac{t^2}{4\tau^2}} \tag{3.4}$$

Figure 3.6 shows the time domain and frequency domain of this differential gaussian pulse with a full width at half maximum $\tau = 110\,\mathrm{ps}$, and the center frequency $f_c = 6\,\mathrm{GHz}$, actually it has a significant energy between 1 and 11 GHz.

This DG pulse has indeed a high center frequency that allows a modest penetration capacity within the tissue and a good spatial resolution, and a deviation value of high standard, which allows to reduce the sensitivity is to the clutter. Ultimately should get a response such as to enable, the algorithm reconstruction, the creation of a map with a good compromise between spatial resolution and contrast.

From [35] and [16], it is possible to conclude that differential gaussian pulse is more suitable for the specific breast model. It works as the exciting source for the following analysis.
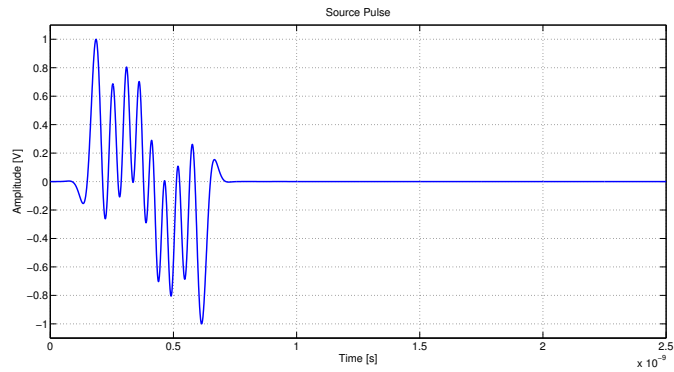
(a)
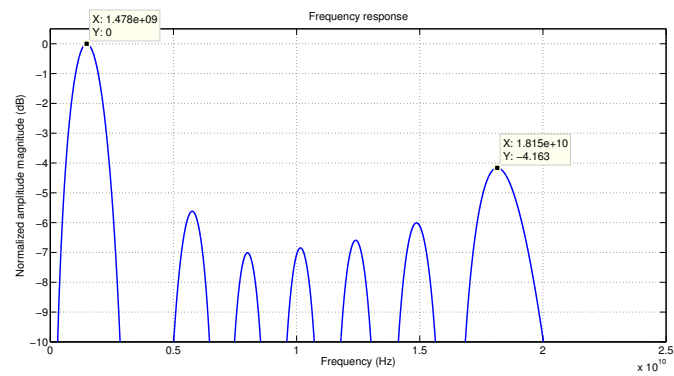
(b)

Figure 3.5.   MMHP used for simulations: a) time domain b) frequency domain.
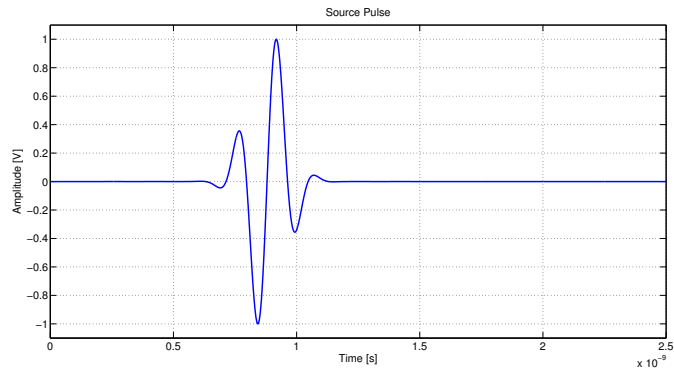
(a)
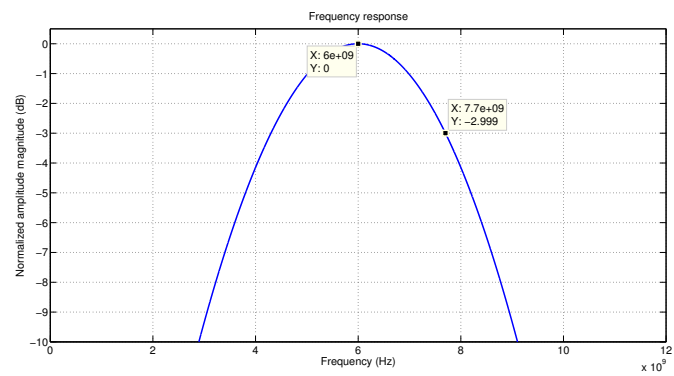
(b)

Figure 3.6.   DG used for simulations: a) time domain b) frequency domain.

3.3 System with homogeneous breast

Now, with above defined system parameter, firstly, the system performance with homogeneous breast is evaluated, which means the dielectric properties of the breast tissue is constant. The functionality of the beamforming algorithm can be verified. The influence of different tumor sizes and tumor positions on the system performance are analyzed.

Before any simulation, an important coefficient should be defined, the propagation speed, which is highly related to determining tumor position. Due to the position of the dielectric discontinuity is expressed by the time delay in the obtained backscattered waveforms. The distance is then computed using the equation, distance=time × velocity, where the time is the pulse round trip time, and the velocity can be calculated based on the Debye parameters in Chapter 2 by the following equaiton:

$$v_p = c \cdot / \sqrt{Re(\varepsilon_r)} \tag{3.5}$$

Where c is the light speed in free space, $3 \cdot 10^8 m/s$, and ε_r is frequency dependent. The plot of the calculated propagation speed versus frequency is shown in Figure 3.7. The propagation speed is $0.95 \cdot 10^8 m/s$ at 6 GHz frequency, which is the central frequency of the applied differential gaussian pulse.
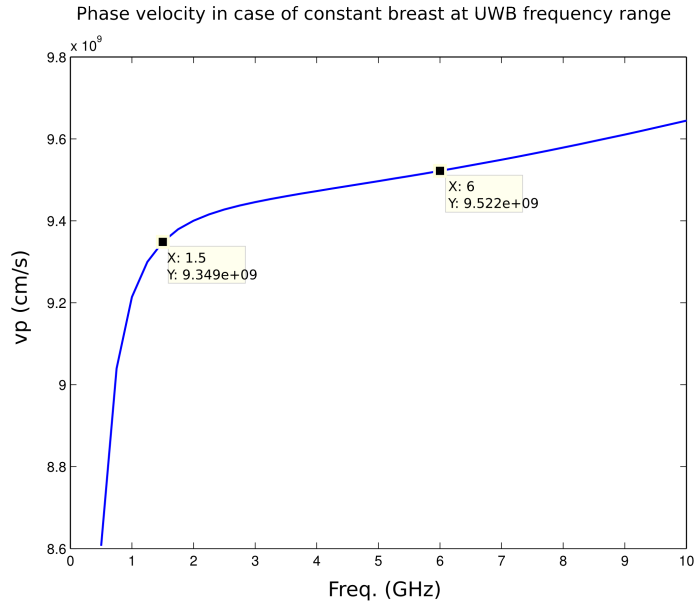
Figure 3.7.   Propagation speed as function of frequency in case of homogeneous breast.

56

3.3.1 Tumor size

The size of the modeled tumor is determined by various factors and has to be carefully chosen. First of all, given that the microwave imaging technique is proposed as a complementary approach to mammography to be used in screening campaigns, an early-stage detection is the target. The size of an early-stage tumor can be defined by reference to the current practice in mammography. Mammography for breast cancer, whose sensitivity depends a lot on the density of the breast tissue, can find tumors with the median size 1 cm to 1.5 cm effectively. Furthermore, studies have shown that 5 mm tumors were found approximately 40% of the time, and the median size at which breast cancers become operationally detectable by mammography is approximately 7 mm [41]. Based on these facts, the upper limit for early-stage detection can be set to around 5 mm and the target for an UWB microwave system to less than 5 mm.

The system performance for tumor sizes of 1 mm, 2 mm, 3 mm and 4 mm due to the homogeneous breast model is evaluated. To better understand the system performance influenced by tumor size, the tumors are placed in the middle of the breast model, at depth of 88 mm. The exciting source is differential gaussian pulse (Figure 3.6). The normalized tumor response is shown in the Table 3.1, which is defined as the peak-to-peak amplitude of the tumor backscattered response divided by the peak-to-peak amplitude of the illuminating pulse. The reflected pulses are shown in Figure 3.8 at antenna 5, it is possible to see that the skin reflections are the same for different tumor size conditions, the tumor information appear within the time intervals 1.5 ns to 2.5 ns, which are zoomed in each figures.

The biggest response is acquired with 4 mm tumor and the smallest with 1 mm tumor. Consequently, the image qualities with 4 mm tumor embedded after reconstruction algorithm should be the best.

Tumor diameter (mm)	Tumor response (dB)
1	-95.2
2	-83.4
3	-79.3
4	-79.0

Table 3.1.   Normalized tumor response with respect to different tumor size.

Before shown the reconstructed energy maps, the pulses after SKAR calibration are presented in Figure 3.9.

The energy maps are demonstrated by Figure 3.10, which are reconstructed by MIST beamforming algorithm. Combining with Table 3.2 which gives the simulated system performance under the ideal analysis condition as a function of the tumor's
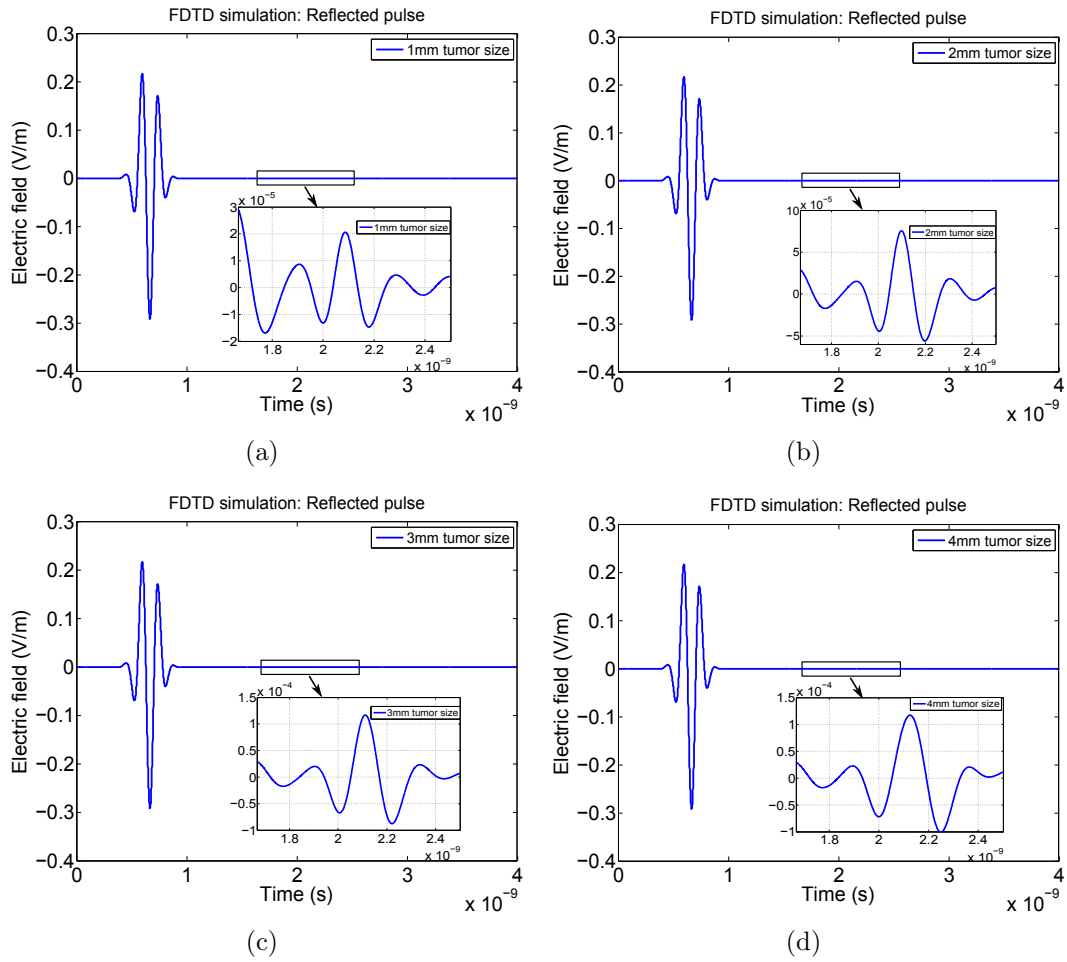
Figure 3.8. Backscattered responses with different tumor size at central position of the breast model, (a) 1 mm (b) 2 mm (c) 3 mm (d) 4 mm.

(a)

(b)

(c)

(d)

(e)

(f)

(g)

(h)

(i)
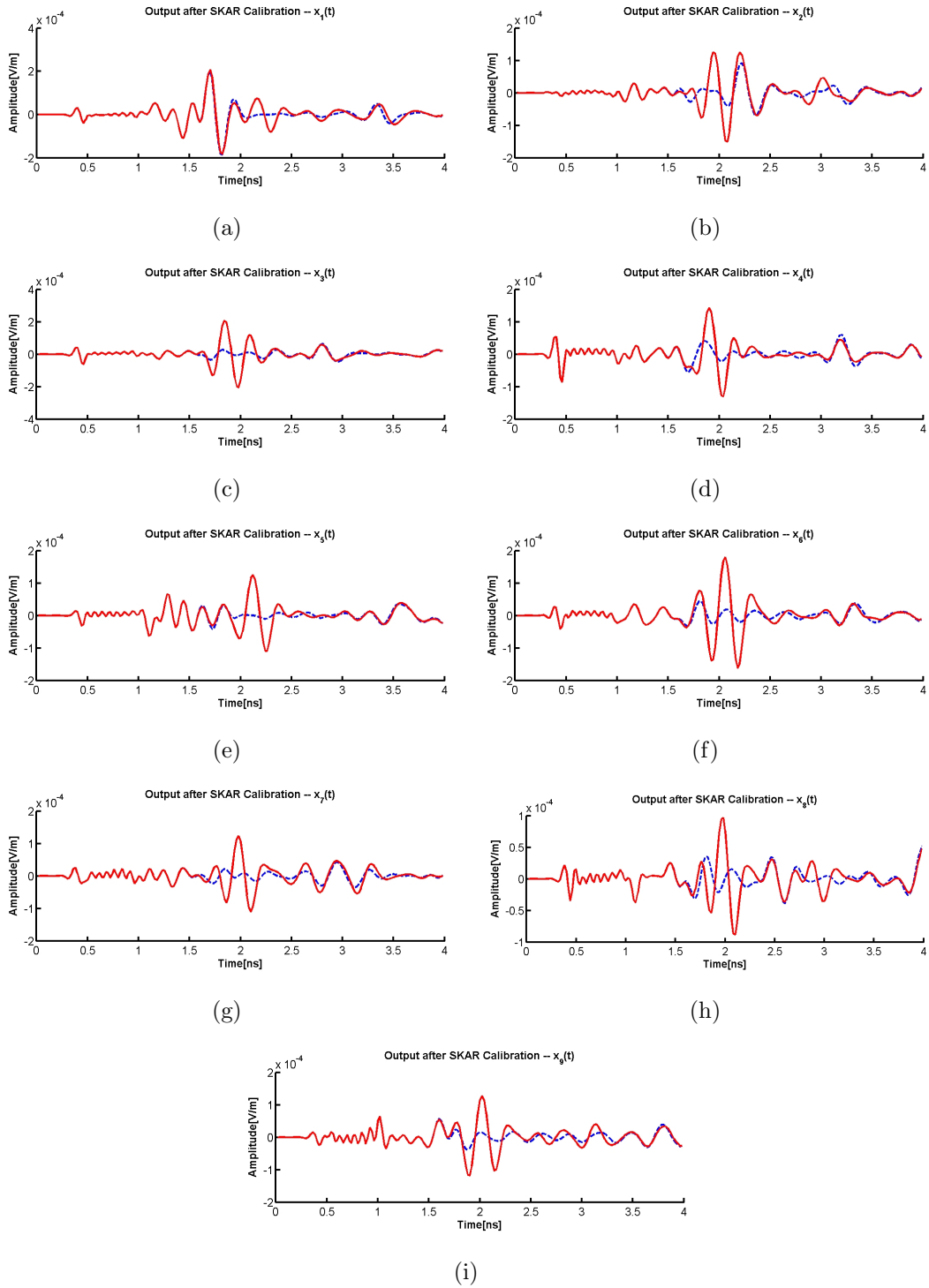
Figure 3.9.   Calibration results with DG pulse, 4 mm tumor and middle tumor position, homogeneous breast, the red lines are cases with tumor, the blue lines are cases without tumor.

59

size, it is possible to see that the applied MIST beamforming algorithm is not able to detect tumor with 1 mm size inside this specific breast model, and it shows much better results with 4 mm tumor inserted. Therefore, 4 mm is chosen as the designed tumor size, since the influence of the hardware implementations and heterogeneous breast model for the following verifications should be taken into account.
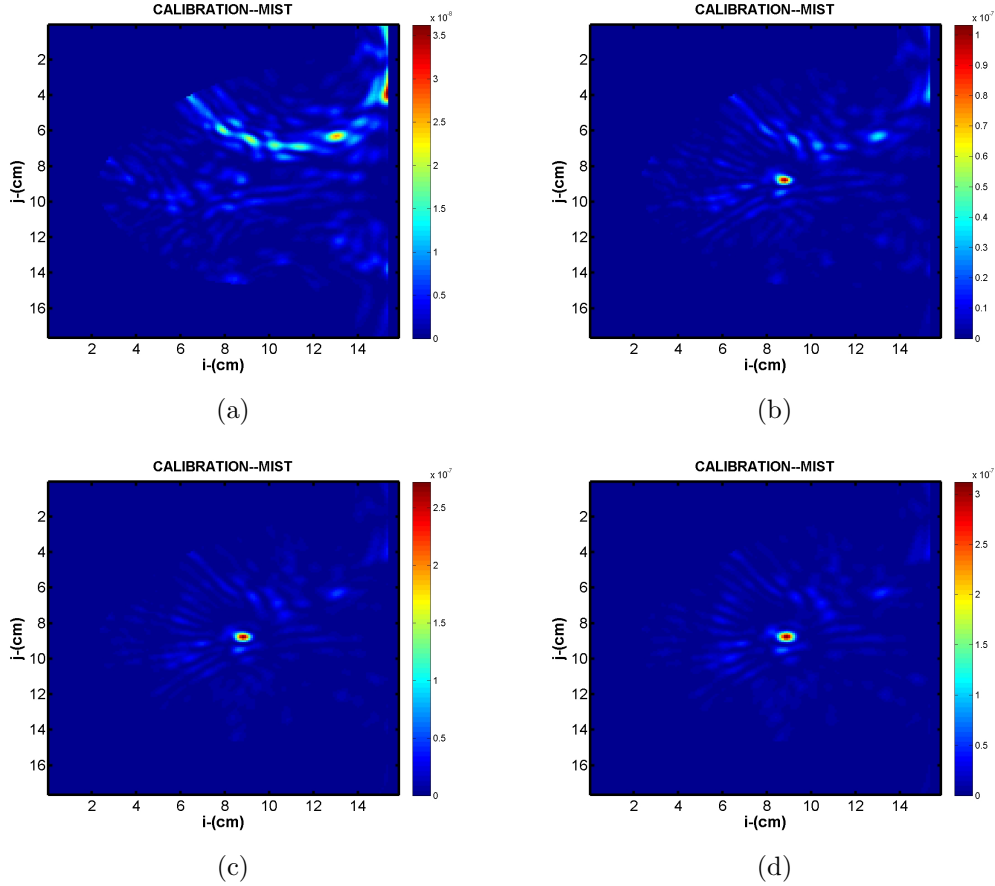
Figure 3.10. Reconstruction results with MIST beamforming algorithm, with different tumor size at central position of the breast model, (a) 1 mm (b) 2 mm (c) 3 mm (d) 4 mm.

3.3.2   Tumor position

The tumor position influence on system performance with 4 mm tumor size are evaluated, not only from reflection pulses point of view, but also from imaging quality point of view. Three different tumor positions are chosen, namely, near,

Tumor size (mm)	SMR (dB)	SCR (dB)	Max. Pos (mm, mm)
1	13.2	-6.3	(153,39)
2	15.7	4.2	(89,88)
3	17.6	7.2	(88,88)
4	17.5	7.8	(89,88)

Table 3.2.   System performance (SMR, SCR) as a function of the tumor's size.

middle and deep. The tumor central positions are (88 mm, 44 mm), (88 mm, 88 mm) and (88 mm, 131 mm) respectively, as displayed in Figure 3.11.
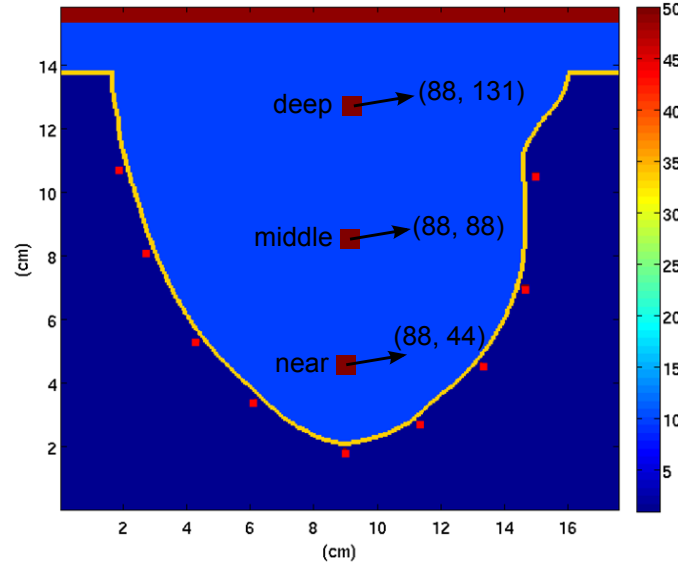
Figure 3.11.   The homogeneous breast model with three tested tumor positions.

Figure 3.12 shows the backscattered responses for different tumor positions. In order to observe and compare tumor information parts easily, the skin artifact parts from the actual reflected waves are subtracted. The tumor information are clearly separated in time. The amplitude of the response from deep position tumor is small due to more tissue attenuation during wave propagation.

The quantitative values of SMR and SCR after beamforming for different tumor positions are tabulated in Table 3.3 and energy maps are graphed in Figure 3.13. The first column in Table 3.3 is the real tumor position, and the fourth column is the simulated maximum energy point, which represents examined tumor position.

The skin artifact removal and imaging reconstruction algorithm are working well,
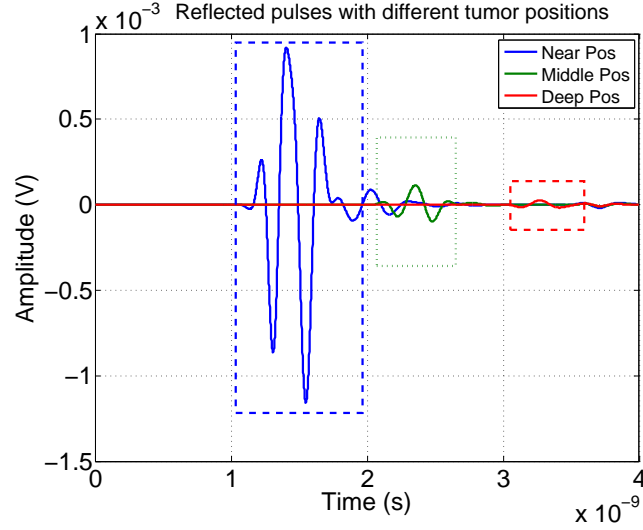
Figure 3.12.   Comparison of the backscattered responses for the different positions of the tumor mass.

as the tumors corresponding to the energy peaks are clearly identified. Moreover, as seen from Figure 3.13 (a), more clutters near tumor appear, the skin contributes more distortion. SMR value for the deep tumor condition is quite small, but the energy peak still can be recognized in Figure 3.13 (c). The reason is that the amplitude of tumor reflection is smaller with larger attenuation and the distortion from breast wall.

Tumor Pos. (mm, mm)	SMR (dB)	SCR (dB)	Max. Pos. (mm, mm)
near (88,44)	15.2	2.6	(88,46)
middle (88,88)	17.5	7.8	(89,88)
deep (88, 131)	12.0	1.9	(89, 131)

Table 3.3.   system performance (SMR, SCR) as a function of the tumor's position.

(a)

(b)

(c)
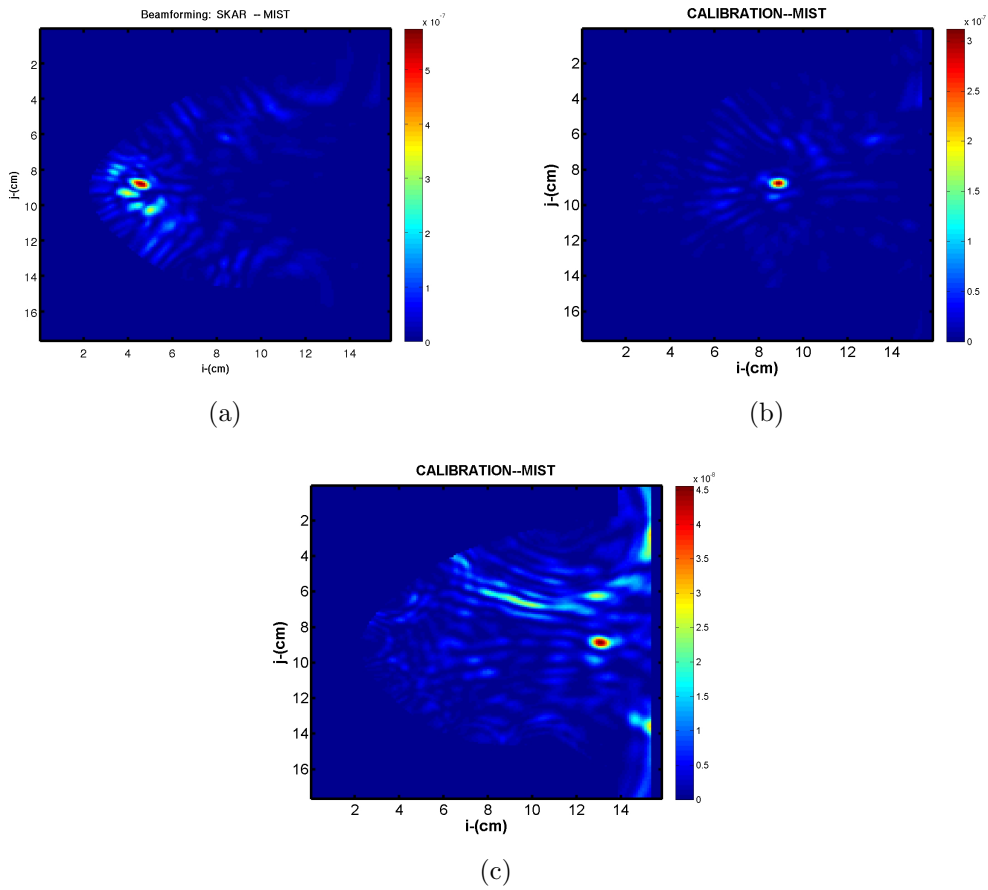
Figure 3.13. Reconstruction results with MIST beamforming algorithm, with different tumor position, (a) near (b) middle (c) deep.

3.4   System with heterogeneous breast

At last, the ideal homogeneous breast model is replaced by the real heterogeneous model. This type of simulation uses signals obtained by real breast phantom FDTD simulation. The pulse in an heterogeneous breast propagates in different ways depending on the tissue that are going through.

The middle position tumor with 4 mm size is inserted. First of all, the heterogeneous breast is shown again in Figure 3.14. It is possible to observe that there are many glandular tissues around tumor, which have high dielectric properties and may add noise. Moreover, each dielectric discontinuity generates a reflection that adds to clutter response.

In this heterogeneous condition, as each kind of tissue has unique ε_r value, we use average propagation speed to approximate the wave propagation behavior in the breast. The average propagation speed was computed using the average dielectric constant of the breast tissues [35]. The average propagation speed is $0.86 \cdot 10^8 m/s$ at 6 GHz central frequency of the applied differential gaussian pulse.
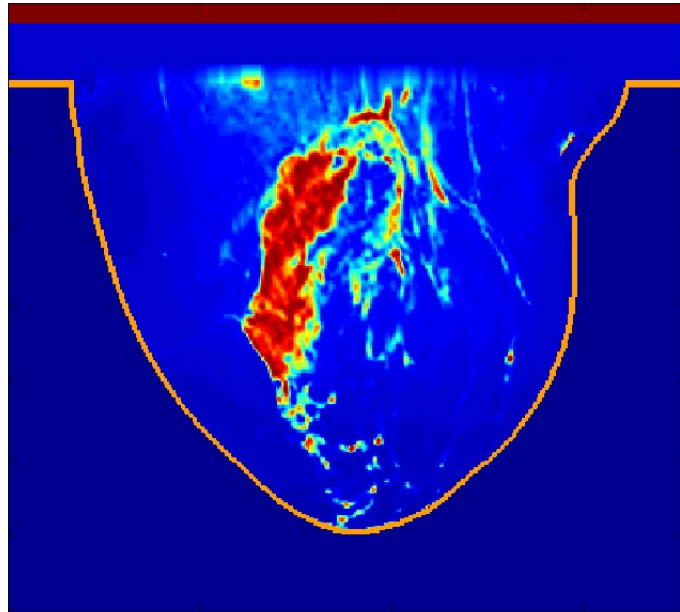
Figure 3.14.   The simulated heterogeneous breast model, 4 mm tumor is inserted in the middle position.

Figure 3.15 displays the backscattered response from antenna 5 with heterogenous breast, as well as the pulse from the same antenna with homogeneous breast model. The exciting sources are differential gaussian pulse in Figure 3.6. They are different even at skin reflection part and in the enlarged late time part. The tumor

information is not as clear as homogeneous one because of clutter responses. Figure 3.16 shows the reconstructed results with MIST beamforming algorithm. Even though the clutters are quite clear, the tumor can be detected. The calculated SMR is 12.7 dB, SCR is 1.2 dB.
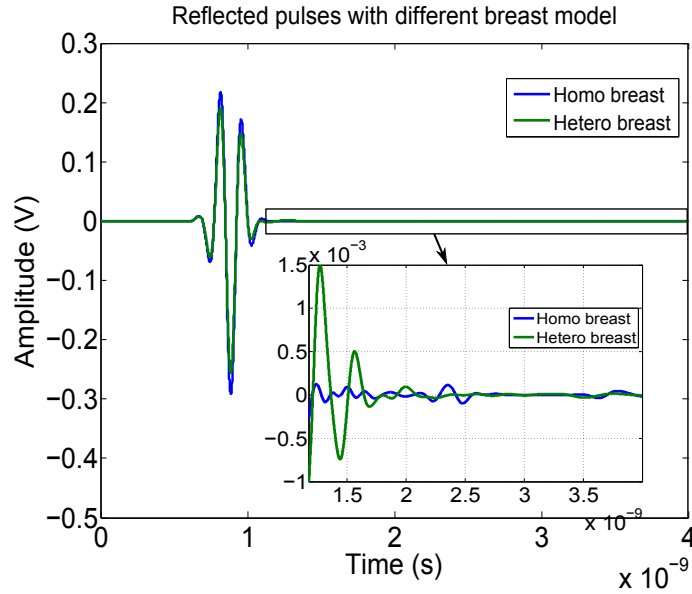
Figure 3.15.   Backscattered responses with different kind of breast model.

All above illustrated simulations have proved the functionality of the proposed UWB radar imaging system for breast cancer detection. The more detailed explanations of the results were shown in [16][35].
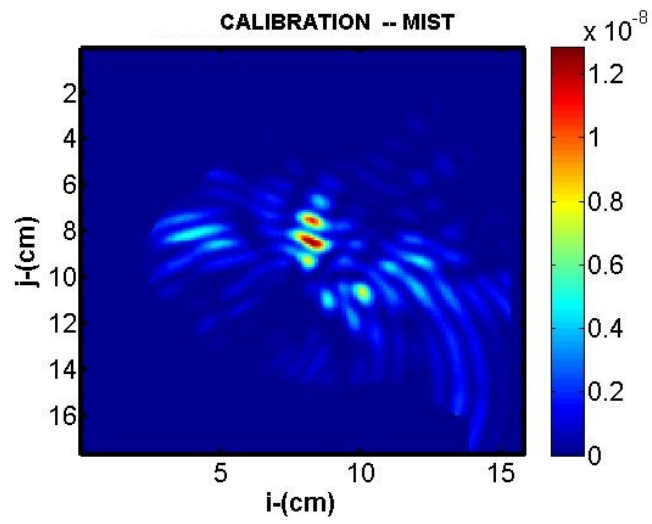
Figure 3.16. Reconstruction results with MIST beamforming algorithm, with heterogeneous breast model, the tumor position is middle and size is 4 mm.

Chapter 4

Receiver comparison

4.1 Motivation

In the previous chapters, the front-end block influence is ignored, it is ideally modeled as a point in FDTD simulation. In this chapter, the discuss will be focused on the front-end block. The system design flow is shown in Figure 4.1, all the components, the transmitter, antenna and receiver are presented. The goal is to define a system-level and architectural solution suitable for the diagnosis application. It is achieved by first proposing a suitable receiver structure, then modeling it and inserting it into the system to evaluate its performance in terms of the system-level performance.
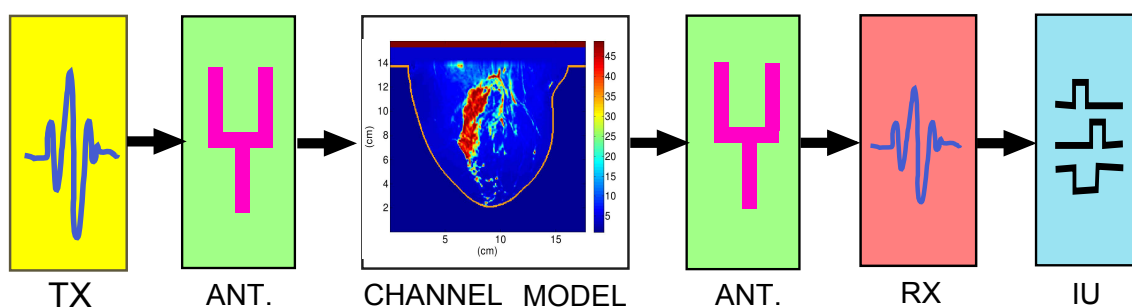
Figure 4.1.   UWB imaging system design flow. Transmitted signals hit the breast and the echoes are acquired with receivers. An imaging unit processes the data and produces a map of reflected energy.

Microwaves may be transmitted as continuous waves, in impulses, by stepped frequencies, pure oscillating sinusoids or as a combination of these methods. Hence, depending on the operating principle, two common radar approaches, impulse radar and Stepped Frequency Continuous Wave (SFCW) radar, are explored. Impulse

radar is a time domain operation, which transmits a single narrow pulse (less than a few nano-seconds), associated with a wide spectrum of signals [42][43]. The time delayed received waveform is then sampled, which, in general, imposes severe constrains on the Analog-to-Digital conversion process. On the other hand, SFCW radar is a frequency domain method, whose waveform is implemented by transmitting a series of single frequency tones separated by a fixed frequency value Δf. At each frequency the amplitude and phase of the received signal is sampled and recorded. Therefore, compared to impulse approach, the SFCW approach requires additional time to transmit and receive N pulses needed to obtain the equivalent wide bandwidth of a single narrow pulse. An additional Inverse Fast Fourier Transform (IFFT) has to be applied to transform the received signals into the time domain synthesizd pulse [44]. The SFCW approach can achieve fine range resolution while maintaining a narrow instantaneous bandwidth which alleviates the ADC requirements. In this chapter, both of them are applied and compared. While accurate electromagnetic simulations and experiments carried out using bulky and expensive RF measurement tools (e.g. vector network analyzers and the like) have proved the validity of the microwave breast cancer detection system, if this method should become suitable for mass screening programs, RF instruments have to be replaced with low-cost and ad-hoc CMOS circuits that integrate the main functionalities in a small chip.

In this thesis, the RF receiver part is described with particular detail because it is the most critical building block. The receiver function is acquire the reflected signals, convert them to digital codes and to send them to the processor. Therefore, the receiver requirements are very strict in this specific application. One of the design challenges that have to be faced is the large dynamics of the received signal, whose maximum amplitude is determined by a large skin reflection. The tumor backscatter is instead a small amplitude signal, which emerges from the background due to the dielectric contrast, but with a magnitude that can be $70\,\mathrm{dB}$ smaller than skin reflection. This can be seen in the FDTD simulation results in Chapter 3. On the other hand, high sampling frequency is another design challenge, as the bandwidth of the excited source is as high as $10\,\mathrm{GHz}$ in our application, based on Nyquist criterion, the sampling frequency is at least two times the signal frequency, so at least $20\,\mathrm{GHz}$ is needed. Therefore, high resolution and high sampling frequency requirement significantly tightens the ADC design constraints.

Since two radar approaches are considered, there are two candidates for the implementation of integrated receiver. One is the direct conversion (DC) receiver, the most popular architecture in narrowband system [45], which has been proposed in this application with SFCW radar approach [46][47]. The other is the UWB receiver based on Coherent Equivalent Time Sampling (CETS) method [48][49]. Both can handle time domain UWB signals and frequency-stepped continuous waves, which is proposed here for the first time in this context.

The **contributions** of this chapter are the following:
1) models of receivers are built behaviorally, by using formulas to represent all their signal processing functions (such as voltage gain, mixing, sampling, etc.) as well as the related non-idealities considered (such as nonlinearity, noise, quantization noise, phase inaccuracy, jitter, etc.). The effect of various circuit impairments is understood and demonstrated with the help of evaluating the performance of the receiver within the breast cancer detection system. Moreover, the performance of DC receiver and CETS receiver with different radar approaches are compared for the first time. The qualities of receivers are ultimately judged with respect to system-level parameters Signal-to-Mean Ratio (SMR) and Signal-to-Clutter Ratio (SCR), as well as energy maps.
2) The fact that the DC receiver is very sensitive to I/Q phase mismatch and phase noise from local oscillator is shown, hence confirming the results reported in [46] under different simulation conditions. Instead, the CETS receiver is more robust to its non-idealities, primarily jitter of the Phase-locked-loops clock and thermal noise, both in case of the time domain single UWB pulse or SFCW sinusoidal signal series.
3) The possibility of saving acquisition time and obtaining even more accuracy with CETS receiver using the time domain radar approach is shown.

4.2 Two different receiver architectures

The main aim here is to develop simple and accurate analytic models of the two receiver candidates with relevant circuit non-idealities. Next, based on these models, the system-level analysis of the entire microwave breast cancer detection system will be performed to explore the receiver design tradeoffs.

4.2.1 Direct Conversion receiver

Figure 4.2 shows the general structure of a RF frontend direct conversion (DC) receiver, in which only one down-conversion component mixer is used to obtain zero-IF signals [45]. As mentioned before, monostatic radar method is applied, only one antenna need be used, the UWB circulator alternately switches the antenna between transmitter and receiver and provides isolation between them.

The basic work flow of the DC receiver is the following: the received RF signal after antenna and circulator is amplified by the low-noise-amplifier (LNA); the amplified RF signal is mixed with in-phase and quadrature local oscillator (LO) signals which are set to be the same frequency of the transmitted RF signal; consequently, the output signals after the mixers contain the desired baseband signal and an undesired signal at twice the RF signal frequency which will be removed by the following low-pass-filters (LPFs); finally the Analog-to-Digital converters (ADCs) are used to
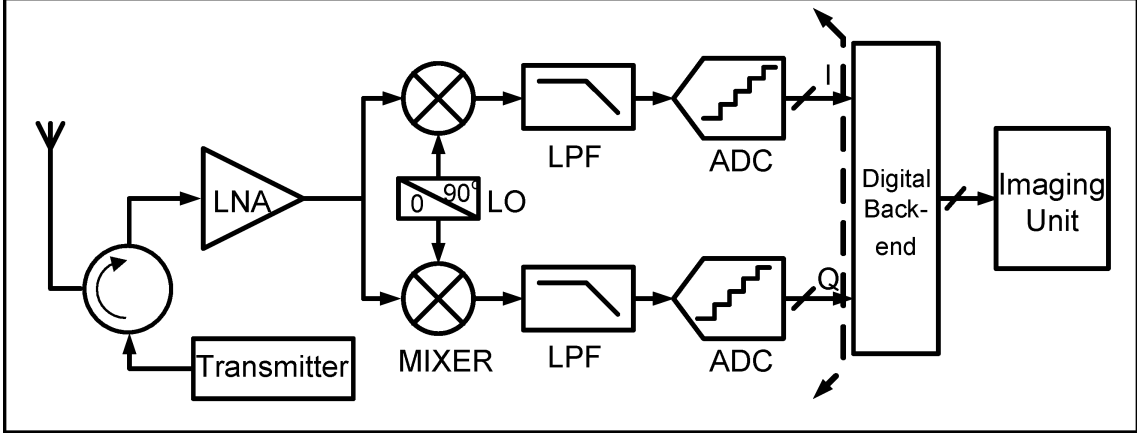
Figure 4.2.   Block diagrams of Direct Conversion (DC) receiver.

quantize the analog complex baseband signal.

In order to make the receiver more realistic, our focus is not only on the functionality implementation of receiver, but also on the modeling techniques of various impairments. The main specific attributes of LNA are conversion gain, thermal noise and nonlinearity. Besides the mixer gain, nonlinearity and thermal noise, the quadrature mixer mainly contributes to the critical In-phase/Quadrature mismatches. Phase noise is the most important impairment in the local oscillator. The main architecture specific non-idealities of ADC are quantization noise and nonlinearity. The behavioral model of DC receiver is shown in Figure 4.3, complex baseband equivalent models are used. The main source of noise is the thermal noise which is specified by the cascaded overall noise figure (NF) while the distortions are expressed by overall saturation and nonlinearity.
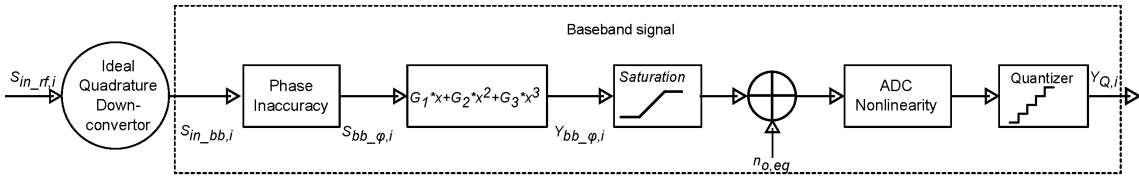
Figure 4.3.   Direct Conversion (DC) receiver behavioral model.

The non-ideal antenna is modeled as a 2-port network, with s-parameters as a function of frequency [50], with the insertion loss at transmitting mode and receiving mode, $(S_{21\_ant}(\omega))$. Non-ideal circulator influences are modeled with insertion loss from transmitter to antenna, $(S_{21\_cc}(\omega))$, the attenuation to the signal as it travels from antenna to receiver, $(S_{32\_cc}(\omega))$, and the transmitter-to-receiver coupling,

$(S_{31\_cc}(\omega))$, respectively. The received signal $S_{in\_rf,i}$ after antenna and circulator can be expressed as:

$$\begin{aligned} S_{in\_rf,i} &= A_{TX}|TF_{all}(\omega_i)|cos\big(\omega_i t + \angle TF_{all}(\omega_i)\big) \\ &+ A_{TX}|S_{31\_cc}(\omega_i)|cos\big(\omega_i t + \angle S_{31\_cc}(\omega_i)\big). \end{aligned} \tag{4.1}$$

where supposing that the transmitted signal is a single tone sinusoidal wave with frequency f_i, as required by the SFCW radar approach, A_{TX} is the signal amplitude at the transmitter. $TF_{all}(\omega) = S_{21\_cc}(\omega)S_{21\_ant}(\omega)S_{21\_ant}(\omega)S_{32\_cc}(\omega)TF(\omega)$. $TF(\omega) = |TF(\omega)|exp(j\angle TF(\omega))$ is the transfer function of our channel model breast which includes both antenna-skin-antenna path and antenna-tumor-antenna path.

After the multiplication with the positive complex LO frequency $e^{j\omega_i t}$ and passing through the low pass filters $h_{lpf}(t)$, the real signal $S_{in\_rf,i}$ is transferred into the ideal baseband complex signals, which is given by the following mathematic expression.

$$\begin{aligned} S_{in\_bb,i} &= A_{TX}|TF_{all}(\omega_i)|e^{j\angle TF_{all}(\omega_i)} \\ &+ A_{TX}|S_{31\_circ}(\omega_i)|e^{j\angle S_{31\_circ}(\omega_i)}. \end{aligned} \tag{4.2}$$

Unfortunately, the down-conversion part (mixers and LO block) includes two impairments, phase noise that comes from LO circuit and I/Q phase mismatch that comes from the In-phase and Quadrature channels phase imbalance. As the tumor position information is included in the time delay of the echoed signals, phase inaccuracies are more critical in this application. A simple model can be realized by changing the ideal LO complex signal expression $e^{j\omega_i t}$ into,

$$\begin{aligned} LO_i &= cos(\omega_i t + \phi_{CM} + \frac{\phi_{DM}}{2} + \Delta\phi) \\ &+ jsin(\omega_i t + \phi_{CM} - \frac{\phi_{DM}}{2} + \Delta\phi). \end{aligned} \tag{4.3}$$

where ϕ_{CM}, common-mode error, represents the phase mismatch between the received RF signals and LO signals, ϕ_{DM}, differential-mode error, represents the phase mismatch between the In-phase and Quadrature components of the LO, both of them are systematic errors and frequency dependent, and are modeled as Gaussian random variables with zero mean and variance σ_{pm}^2. $\Delta\phi$ represents the phase noise, it is a random error, and we model it as Gaussian stochastic process with zero mean and variance σ_{pn}^2.

Consequently, the distorted complex baseband signal $S_{bb\_\phi,i}$ can be expressed as

$$S_{bb\_\phi,i} = S_{in\_bb,i}e^{-j(\phi_{CM}+\Delta\phi)}cos(\frac{\phi_{DM}}{2}). \tag{4.4}$$

The overall receiver nonlinearity can be modeled straightforwardly using the power series equation [51]. Therefore the baseband equivalent nonlinearity model

can be expressed as,

$$
\begin{aligned}
Y_{bb\_\phi,i} &= G1 \cdot S_{bb\_\phi,i} + G2 \cdot |S_{bb\_\phi,i}|^2 (1 + j) \\
&+ G3 \cdot |S_{bb\_\phi,i}|^3 e^{j \angle S_{bb\_\phi,i}}.
\end{aligned}
\tag{4.5}
$$

where the higher order terms above third order are usually not taken into account. $G1$ is the linear conversion gain, $G2$ and $G3$ are the coefficients of the second-order and third-order nonlinearity specified by IIP2 and IIP3 [51], respectively. In case of high input power, a simple saturation is applied, the signal after that will be $Y'_{bb\_\phi,i}$.

Then, the thermal white noise source $n_{o,eq}$ is added, which is modeled as additive white gaussian noise (AWGN), with the equivalent output noise power given by,

$$
P_{noise} = KTB \cdot F \cdot G1^2.
\tag{4.6}
$$

where K is Boltzmann's constant, T is temperature, B is the noise bandwidth after low pass filter and F is the overall noise factor.

Finally, the analog signal is converted to digital code by ADC. There are two steps, first, the signal will come through the nonlinearity distortion part of ADC whose contribution is reflected by integral nonlinearity (INL) rather than IIP2 and IIP3. The non-uniform quantization level is modeled like [52]. Then, ideal quantization, which includes inherent quantization noise is applied. The final data before signal processing is expressed as,

$$
Y_{Q\,i} = [Y'_{bb\_\phi,i} + n_{o,eq}]_q.
\tag{4.7}
$$

$[\cdot]_q$ means quantization.

The flicker noise and DC offset are not modeled, as presented in [47], the autozeroing and chopper stabilization techniques are applied to ignore their influences.

4.2.2   CETS receiver

In this breast cancer detection field, tumor information is much weaker than skin artifact due to the radial spreading of the pulse energy, the path loss and the lossy breast tissue, therefore, it is important to use a high dynamic range receiver to capture the variation in the received analog signals. However the high Nyquist sampling frequency leads to severe constraints in the implementation of ADC.

The proposed CETS receiver is based on the Coherent Equivalent-Time Sampling technique, the work principle is that N samples are taken out of M identical pulses. The properties of the CETS receiver can be summarized as follows:

- The input pulses are periodic

- The equivalent sampling frequency is much greater than Nyquist frequency based on the N and M choice

- The digital backend is necessary to sort the sampled signals

- Average technique is used to reduce the random noise effect

Therefore, compared to conventional Nyquist sampling technique, CETS method can alleviate the sampling frequency requirements for ADC by sampling the periodic signal at a much lower frequency [48][49][53].

In this case the normal acquisition of a single pulse is achieved by gathering samples from different received pulses. Assuming each pulse is repeated M times every T_{pulse} time units, the overall acquisition time equals to MT_{pulse}, N samples are taken out of these M identical pulses, this causes the pulses to be sampled at a real-time sampling frequency of

$$f_s = (MT_{pulse}/N)^{-1} \qquad (4.8)$$

the corresponding equivalent sampling frequency is

$$f_{eq} = (T_{pulse}/N)^{-1} \qquad (4.9)$$

which can be much higher than Nyquist sampling. The technique can severely relaxes the trade-off between the sampling rate and quantization resolution by choosing appropriate M and N values.

Figure 4.4 shows an example of CETS technique, the pulse is repeated 10 times, and 27 samples are acquired. After sorting there are 27 samples in one single pulse, the equivalent sampling frequency is therefore 27 times larger than the pulse frequency and the real sampling frequency is only 2.7 times the pulse frequency which simplifies the circuit design of the ADC.

Figure 4.5 depicts the architecture of the CETS receiver. The received signal as the one in DC receiver is amplified by LNA and then directly sampled by track and hold amplifier at a relatively low sampling frequency, and quantized by ADC. A time to digital converter measures the time offset between transmitted clock and sampling clock. The sampling clock is synthesized by a phase-locked loop (PLL) and locked to the pulse repetition clock of the transmitter with the correct M/N ratio. The N samples are not acquired in order and therefore the digital back-end sorts them. The receiver can acquire the same signal multiple times (K) and average them to reduce the effect of random noise.

Let us focus on the block diagram of Figure 4.6 representing the behavioral model of the CETS receiver. Similarly to the DC receiver, the model includes the main ideal receiver functionality as well as the following imperfections: thermal noise and distortions generated in the very front-end components, ADC quantization

73
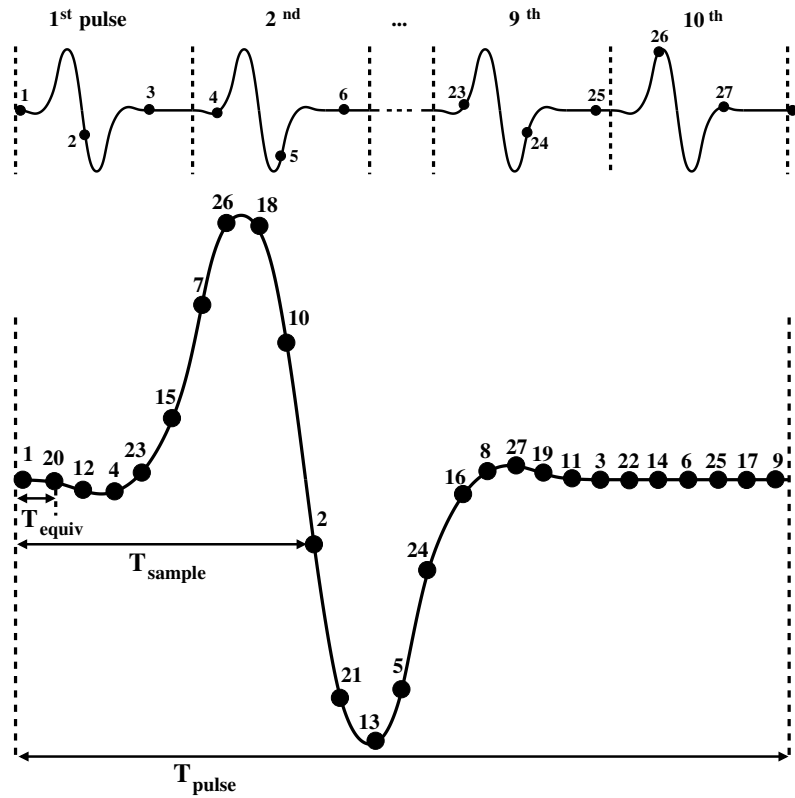
Figure 4.4.   Example of Coherent Equivalent-Time Sampling. Twenty-seven samples of the pulse are acquired in ten repetition periods (27 and 10 are relatively prime). Samples are not acquired in order and need to be sorted.
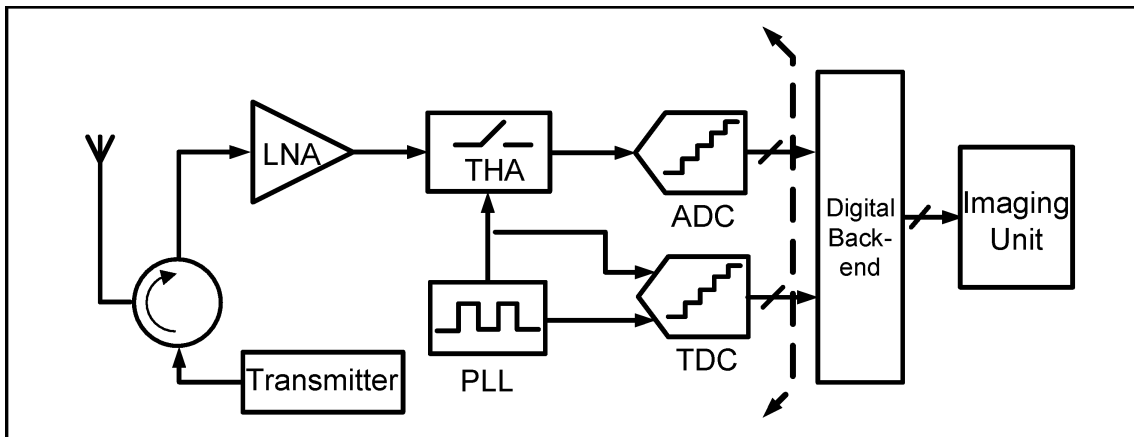
Figure 4.5.   Block diagrams of Coherent Equivalent Time Sampling (CETS) receiver.

noise and INL. Besides these parameters, the architecture unavoidable impairment random timing jitter produced in PLL has also been involved, which is an undesired perturbation or uncertainty in the timing of events.
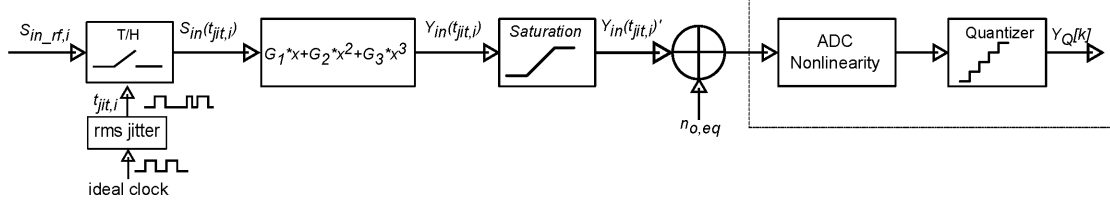
Figure 4.6.   CETS receiver behavioral model.

Since the periodic signal can be both a tone and a periodically repeated UWB pulse (e.g. generated by an UWB transmitter like in [28]), the CETS receiver can work both in SFCW mode and in time-domain. In the first case, amplitude and phase of the received signal are computed by the digital back-end. To permit an easier comparison with the DC receiver, we report the model equations with sinusoidal signals.

The incoming time domain RF signal $S_{in\_rf,i}$ is directly sampled by THA which is modeled as an ideal switch controlled by the sampling clock from PLL. Considering the presence of Root Mean Square (RMS) timing jitter, the rising or falling edge of the sampling clock is deviated with a time deviation j from its ideal position. The noisy sampled signal can be written as,

$$S_{in}(t_{jit,i}) = S_{in\_rf,i}(t_{jit,i}) \tag{4.10}$$

where $t_{jit,i}(m) = mT_s + j_i(m)$, $t_{jit,i}$ is the real sampling clock with jitter influence, T_s is the real sampling period, m is the mth sample, $j_i(m)$ is the mth jitter value for the ith signal, which is modeled as gaussian random variable with zero mean and variance σ_{jit}^2.

Meanwhile, linear conversion gain and AM-AM nonlinearity are modeled using the power series equation.

$$\begin{aligned} Y_{in}(t_{jit,i}) &= G1 \cdot S_{in}(t_{jit,i}) + G2 \cdot (S_{in}(t_{jit,i}))^2 \\ &+ G3 \cdot (S_{in}(t_{jit,i}))^3 \end{aligned} \tag{4.11}$$

Before converting the signal from ADC, thermal noise is added, whose equivalent power is proportional to the signal bandwidth and the overall cascaded noise factor. Since there are not filters in this receiver, the multi GHz signal bandwidth makes thermal noise quite huge in contrast to the case in DC receiver whose noise is filtered

by LPF. Hence, averaging technique is usually applied to alleviate the influence of random noises, like thermal noise and jitter.

$$Y_Q[K] = [Y_{in}(t_{jit,i})' + n_{o,eq}]_q. \tag{4.12}$$

The digital signal Y_Q is therefore the input data of the following digital processing. In addition, the CETS receiver is insensitive to DC offset and flicker noise, because it works at high frequency.

4.3 Methodology and simulation setting

In this chapter the performance of three different system combinations are evaluated, namely DC receiver working with SFCW radar approach, CETS receiver working with SFCW approach and CETS receiver working with impulse time domain radar approach.

Two dimensional electromagnetic breast model is used as the channel model in the system simulations that includes the influence of dispersion and attenuation, as described in previous chapters. A 4-mm diameter tumor with high dielectric properties is inserted in the breast model [54] [4].

For the impulse radar approach the transmitted signals are short UWB pulses. The pulse characteristics must be chosen accordingly to the range resolution and penetration depth, the differential gaussian pulse with a central frequency of about 6 GHz and full width at half maximum equal to 110 ps is used as in [40] [33]. Since the pulse has a significant energy in a 10 GHz bandwidth, the complete system should be able to process an operational bandwidth from 1 GHz to 11 GHz. Use of the SFCW technology results in a system transmitting a single sinusoidal tone starting from 1GHz and stoping at 11GHz, with a fixed frequency step 125 MHz. Consequently, 81 tones are required to cover the equivalent wide bandwidth of a single narrow pulse.

Below these radar specifications are translated into radar functional requirements, range resolution S_r and unambiguous range R_{unabm} [44].

$$S_r = \frac{\upsilon}{2B}, \qquad R_{unabm} = \frac{\upsilon}{2\Delta f} \tag{4.13}$$

where υ is the wave speed in the medium, B is the bandwidth (10 GHz in our case), and Δf is the frequency step (125 MHz). The average propagation velocity is less than 10^8 cm/s, which results in S_r and R_{unabm} about 4.7 mm and 40 cm respectively. These values are sufficient to detect the 4 mm-diameter tumor.

Receiver model equations, electromagnetic breast model, and beamforming algorithm are implemented in Matlab. In order to make these three scenarios more comparable, most of the receivers parameters are set equal in all configurations. The

76

Param.	DC	CETS–Freq.	CETS–Time
Power supply (V)	1.2	1.2	1.2
signal BW (GHz)	1-11	1-11	1-11
total gain (dB)	40	40	40
noise figure (dB)	10	10	10
IIP2 (dBm)	20	20	20
1dB compression point (dBm)	-30	-30	-30
antenna S11 (dB)	-10	-10	-10
circulator S21/S32 (dB)	-5	-5	-5
circulator S31 (dB)	-18	-18	-18
INL (LSB)	2	2	2
noise BW (Hz)	100K	10G	10G
TX power (dBm)	-50 to -18	-50 to -14	-50 to -2
ADC bits	11 to 17	7 to 12	7 to 12
phase noise (deg)	0 to 0.21	NA	NA
phase mismatch (deg)	0 to 6	NA	NA
RMS jitter (ps)	NA	0 to 6	0 to 6
K (iterations)	1 or 100	1 or 100	1 or 100

Table 4.1.   Parameters used in simulation.

high conversion gain is required to amplify the input signals, especially the weak tumor information, but it can not be too high to avoid ADC saturation which will cause distortion, especially the strong skin reflection. According to [46], 40dB gain and 10dB noise figure for two receivers are chosen. The 1-dB compression point is set to -30dBm which indicates around -20dBm IIP3 value. The in-band return loss S11 of UWB antenna is set to be -10dB [55], transmitter-to-receiver isolation and the insertion loss of circulator are set to -18dB and -5dB respectively [56].

The number of bits (NoB) of the ADC, must be chosen accordingly to two opposite requirements: on the one hand it's better to keep it as low as possible for cost and power consumption reasons, on the other hand, the high resolution is needed to have less quantization noise and to improve receiver accuracy. Therefore, due to the different sampling frequency, the ADC resolution of DC receiver is swept from 11bit to 17bit, but only 8bit to 12bit for CETS receiver. The maximum INL value is set to be 2 times the Least Significant Bit (LSB) value [57][58]. Furthermore, the standard deviation of the phase mismatch, phase noise and rms jitter are swept from 0 to 6 degree, 0 to 0.2 degree, and 0 to 6ps respectively.

These parameters are summarized in Table 4.1. The strategy is to fix the values of each common parameters and to choose the appropriate values for other parameters

by sweeping the values of each individual non-ideality considered as an independent and additive noise source.

The effects of the impairments on the receiver performance are characterized in terms of the overall detection system performance, in other words, imaging quality which is specified by visual inspection of the energy maps reconstructed by imaging algorithm [59][33] and SMR/SCR. As defined in Chapter 2, the tumor can be detected if and only if SMR and SCR are greater than 10 dB and 0 dB, an energy peak appears at the correct tumor position. The coming reported SMR/SCR results for each scenarios with random non-idealities are the average from at least 20 times repeated Matlab simulations.

Before any evaluation, the system feasibility is verified. If the effect of all the impairments in Table 4.1 is not considered—i.e. all noise sources, mismatches, non-linearity, and quantization are removed—a system with ideal receiver is obtained. However the 40 dB gain may cause ADC saturation of the skin reflection part in the received signal, this saturation is unavoidable. Without loss of generality, we consider tumors with in three different locations, at (7.0 cm,5.2 cm), (8.8 cm,8.8 cm) and (11.7 cm,12.6 cm), corresponding to a position close to the skin, in the middle of the breast and deep in the breast. It is possible to verify that in this ideal case these three scenarios yield the same results. The values of SMR and SCR are tabulated in Table 4.2, and energy maps are graphed in Figure 4.7. The built system works well as the tumors corresponding to the energy peaks (enclosed by a circle) are clearly identified. Moreover, as seen from Figure 4.7 (a), more clutters near tumor appear, due to the skin distortion. SMR value for the deep tumor condition is quite small, but the energy peak still can be recognized in Figure 4.7 (c), the reason is that the amplitude of tumor reflection is smaller with larger attenuation, and the distortion from breast wall. In theory, receiver parameters do not depend on tumor position as the tumor information happens at different time delay.

Tumor Pos.	SMR(dB)	SCR(dB)	Max. Energy Pos.
(7.0 cm, 5.2 cm)	15.8	2.3	(7.0 cm, 5.1 cm)
(8.8 cm, 8.8 cm)	16.5	7.0	(8.8 cm, 8.8 cm)
(11.7 cm, 12.7 cm)	11.6	2.6	(11.7 cm, 12.8 cm)

Table 4.2.   SMR and SCR in the ideal case with different position.

Since the focus in this chapter is to compare different receivers, to better assess the influence, the middle position tumor is used in the following simulations. Results reported in the next section, where all the impairments are considered, can be compared to the ideal case to evaluate the performance degradation.
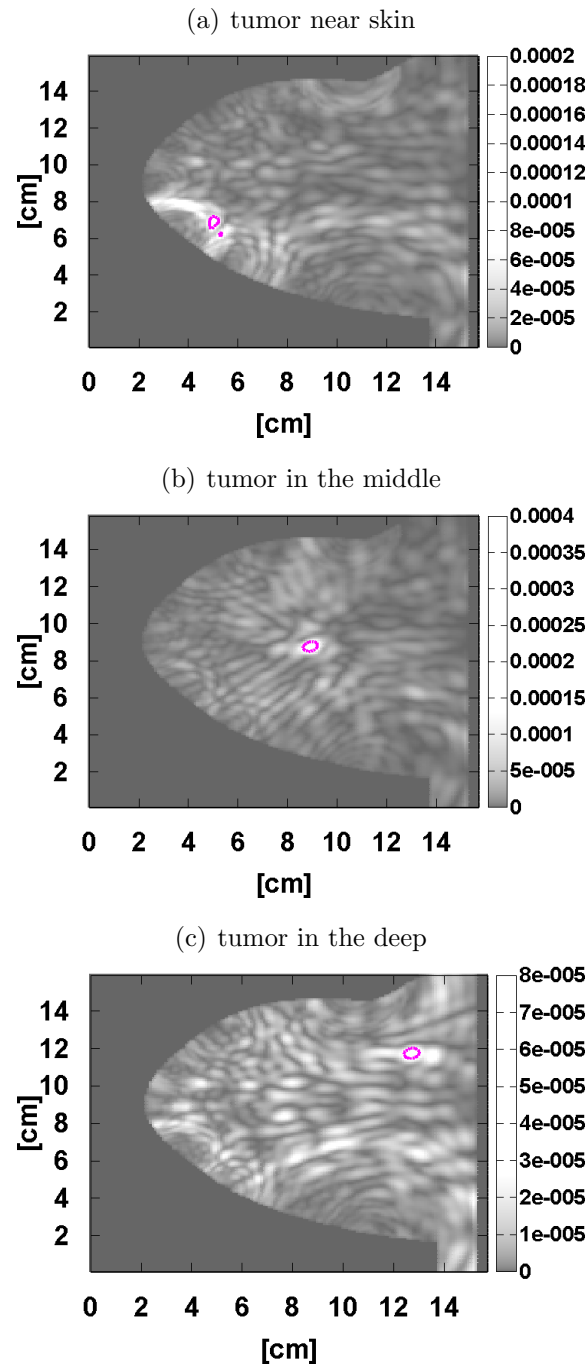
Figure 4.7.   Energy maps of the breast with the ideal receiver for different tumor positions. Map (a) is for tumor placed near skin, (b) for tumor placed in the middle of breast, (c) for tumor placed deep in breast.

4.4   Simulation results

In order to choose the suitable values for the parameters of each receiver and thereby compare the performance of three scenarios, the effectiveness of these main impairments on the receiver performance are demonstrated in this section. They are evaluated in terms of system-level parameters such as SMR and SCR.

4.4.1   DC receiver with SFCW approach

The most critical impairments for DC receiver are ADC resolution, phase noise and phase mismatch. Their influences are presented one by one.

ADC

As highlighted in the previous section, ADC has two main limitations, ADC resolution and nonlinearity. We set all the fixed parameters in Table 4.1 to the nominal value. In this evaluation, all the non-idealities are not considered, except ADC and saturation. Figure 4.8(a) shows the evaluation of system performance at different transmitted power with different ADC resolution, which changes from 11 to 17bit. Considering the region of low resolution, the SMR and SCR values increase with transmitted power. Considering instead the region at low power, the impact of quantization noise is evident as SMR/SCR values improve obviously when ADC resolution increases. The curves indicate that the performance benefit of using higher ADC resolution is negligible when ADC bits is bigger than 15-bit.

Figure 4.8(b) and (c) depict the overall performance with additional ADC nonlinearity INL. Compared to Figure 4.8(a) and (c), the values in Figure 4.8(b) and (d) have at least 1dB and 2dB decrease respectively, moreover, ADC nonlinearity has stronger influence at low power and low resolution. However, the selected 15-bit ADC reaches the optimum performance for transmitted power between -35dBm and -20dBm. Consequently, this power range and a 15-bit ADC is used for the following analyses.

Phase Noise

In this analysis we evaluate the effect of transmitted power and phase noise variance σ_{pn}^2. Simulations are run for values of σ_{pn} between 0 and 0.21^0. Results are obtained using ADC quantization of 15bit with all other impairments set to their nominal value as in Table 4.1, like thermal noise, nonlinearity and saturation, while, phase mismatch is not considered yet.

Figure 4.9(a) shows the results when K is set to 1 (no iterations). SMR and SCR are sensitive to the variance of phase noise during 0.15^0 and 0.03^0, there is a
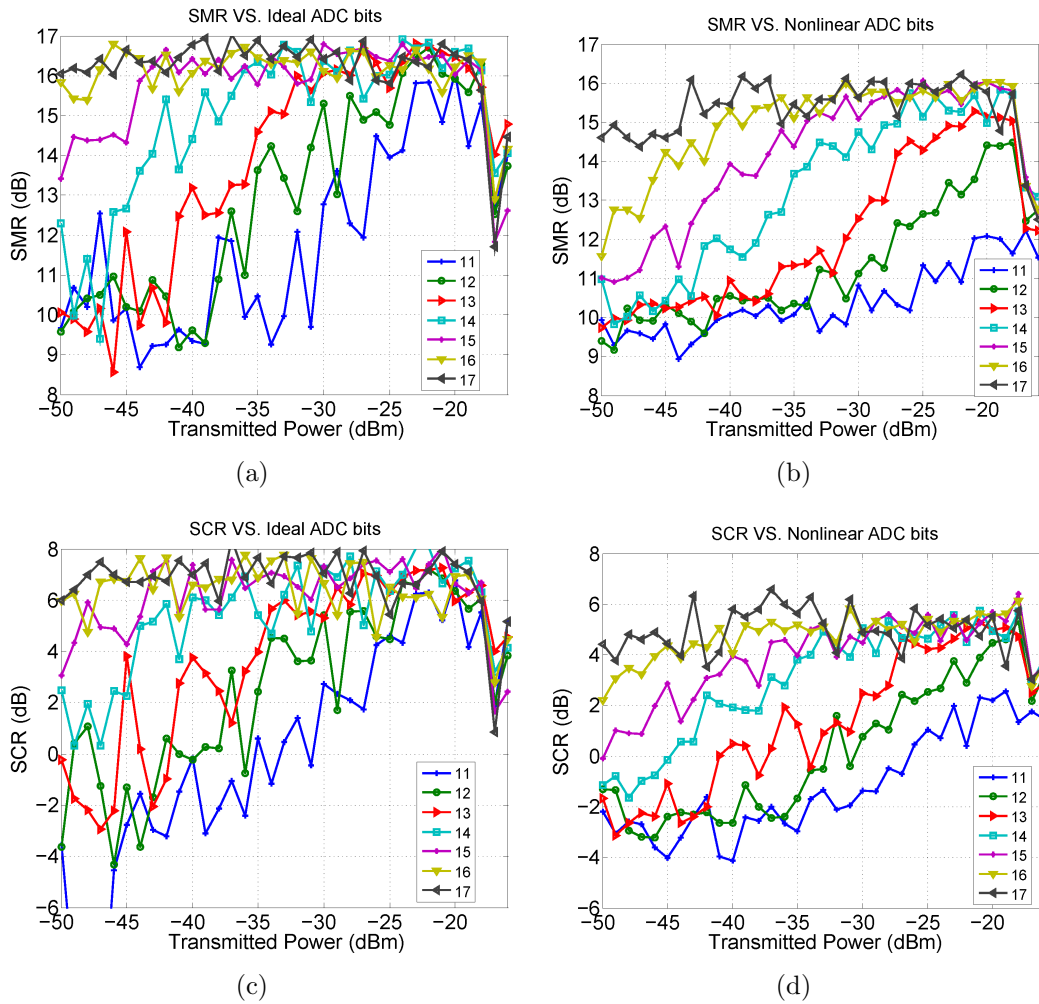
Figure 4.8. DC receiver system performance (SMR a-b, SCR c-d) with different signal power and ADC bits; results are reported both for ideal ADC (a,c) and for ADC with nonlinearity (b,d).

decrement of $2\,\mathrm{dB}$ when σ_{pn} increases from 0.09^0 to 0.15^0 and an increment of $2\,\mathrm{dB}$ increase when σ_{pn} is 0.06^0 smaller than 0.09^0. The overall system performance is mainly influenced by phase noise, but comparing the blue line(phase noise excluded) in Figure 4.9(a) with Figure 4.8(b) and (d), we see that thermal noise have clear influence when transmitted power is less than -35dBm. In the high power part, bigger than -18dBm, the nonlinearity limits the performance.

As defined in Section 4.3, in order to make the three scenarios comparable, we also apply the average technique to DC receiver. Figure 4.9(b) shows the results with $K = 100$ iterations, which prove that the random thermal noise and phase noise can be reduced by an average operation. However, this operation increases the data acquisition time which will be discussed later. Considering a real circuit implementation, a value of 0.1^0 as phase noise standard deviation is chosen, the corresponding maximum SMR value is about 14dB without average.
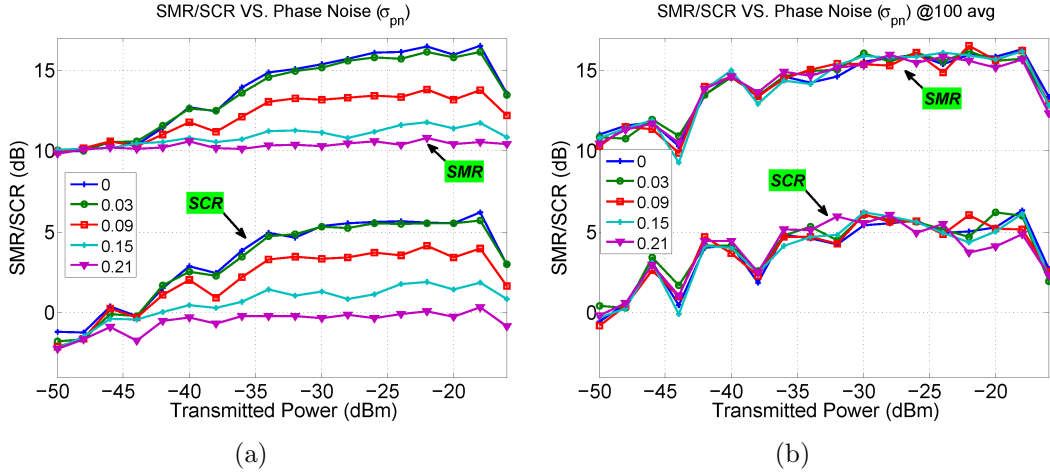
Figure 4.9. DC receiver system performance with different signal transmitted power and phase noise σ_{pn}; results are reported both for a single evaluation (a) and for an averaging on 100 trials (b).

Phase Mismatch

Common mode and differential mode phase mismatch are then added to the model, with standard deviation σ_{pm} sweeping from 0 to 6^0, while the other impairments left untouched. -28 dBm is chosen as the transmitted power, which is the value that optimizes performance. Figure 4.10 shows the results with and without average, we see that SMR and SCR values decrease when phase mismatch increases. In addition, since the phase mismatch is a systematic error, comparing Figure 4.10(a) and (b), it can be observe that, even with 100 times average, the phase mismatch

influence on system performance can not be alleviated. The overall performance improvement is determined by the averaging of thermal noise and phase noise. As a result, σ_{pm} greater than 2^0 can cause more than $1\,\mathrm{dB}$ SMR decrease. As a guideline for designers, phase mismatches must be kept well below this limit.
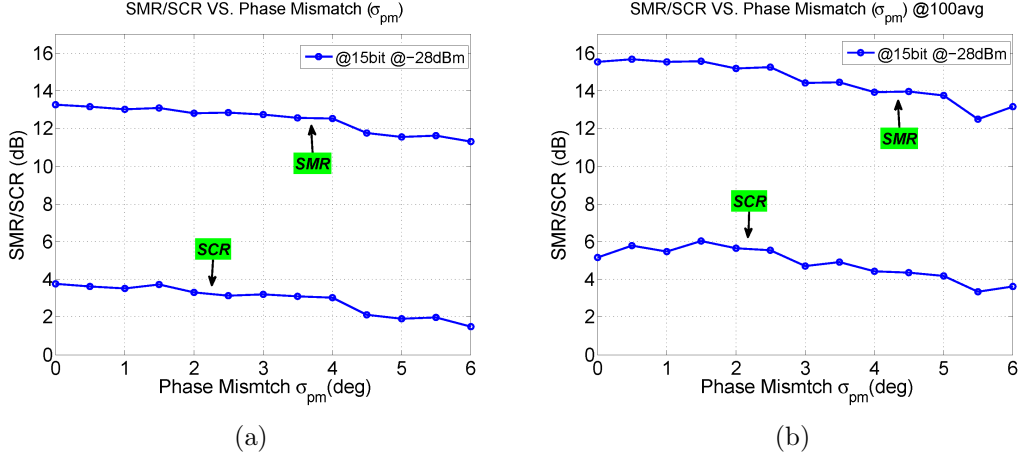
Figure 4.10. DC receiver system performance (SMR, SCR) with different phase mismatch with 15-bit ADC and -28dBm transmitted signal power; results are reported both for a single evaluation (a) and for an averaging on 100 trials (b).

4.4.2 CETS receiver with SFCW approach

Considering the results obtained for the DC receiver, the critical impairments in CETS receiver should be ADC resolution, thermal noise and jitter. Concerning thermal noise, there is no mixer and filter in CETS receiver, the receiver will work in the whole input signal bandwidth, in our specific case 10GHz, therefore, much more influence from thermal noise than in DC receiver is expected.

ADC

Figure 4.11 shows the values of SMR and SCR as a function of transmitted power, with ADC resolution changing from $7\,\mathrm{bit}$ to $12\,\mathrm{bit}$. Thermal noise and jitter are not included now, K is set to one iteration. The difference between Figure 4.11(a) and Figure 4.11(b) is the presence of the ADC nonlinearity, as can be seen there is only a small difference in system performance, indicating that the effect of ADC INL is negligible at these ADC resolution levels. However, the results demonstrate that the system performance is good enough when ADC resolution is bigger than 9-bit in the range of -35 dBm and -22 dBm transmitted power. In addition, the performance

starts to be strongly limited by nonlinearity, especially saturation, when transmitted power is larger than -22dBm.

ADC sampling frequency might be relatively high, thus, based on the technique design constraints, 10-bit is the perfect choice. With a resolution of 10 bit, SMR and SCR are bigger than 15 dB and 5 dB respectively, between -35 dBm and -22 dBm power range.
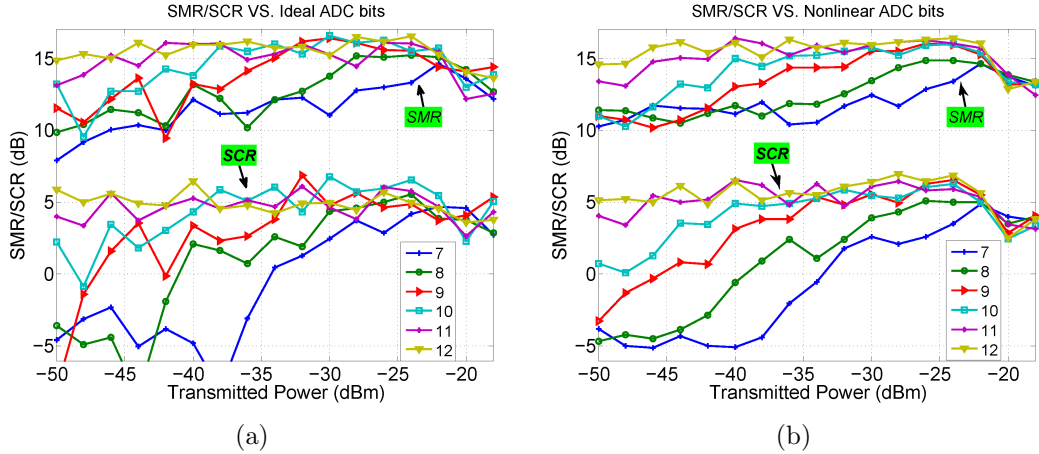
Figure 4.11. CETS receiver system performance (SMR, SCR) with SFCW approach with different signal power and ADC bits; results are reported both for an ideal ADC (a) and for a nonlinear ADC (b).

Thermal noise

The simulation results of the CETS receiver with 10-bit ADC and additional thermal noise are presented in Figure 4.12(a). It is possible to see that the influence of thermal noise is significant, especially at low power, since the system does not work if the signal power is less than -30 dBm. Actually, the thermal noise influence is less than in the case we are about to examine (CETS in time domain). This is caused by the FFT operation after the ADC which behaves as a bandpass filter centered around the given frequency.

The results after enough average time (100 times here) in Figure 4.12(b) proves the perfect functionality of the average technique in reducing random noise. The SMR and SCR reductions in low power part are due to the ADC quantization noise and ADC nonlinearity. It is therefore a necessary to implement averaging technique in this kind of receiver and application. Figure 4.12(b) illustrates that the ideal working power range still is from -35 dBm to -22 dBm, in order to keep consistent

with the above DC receiver, -28 dBm is chosen as our transmitted power for our following evaluation.
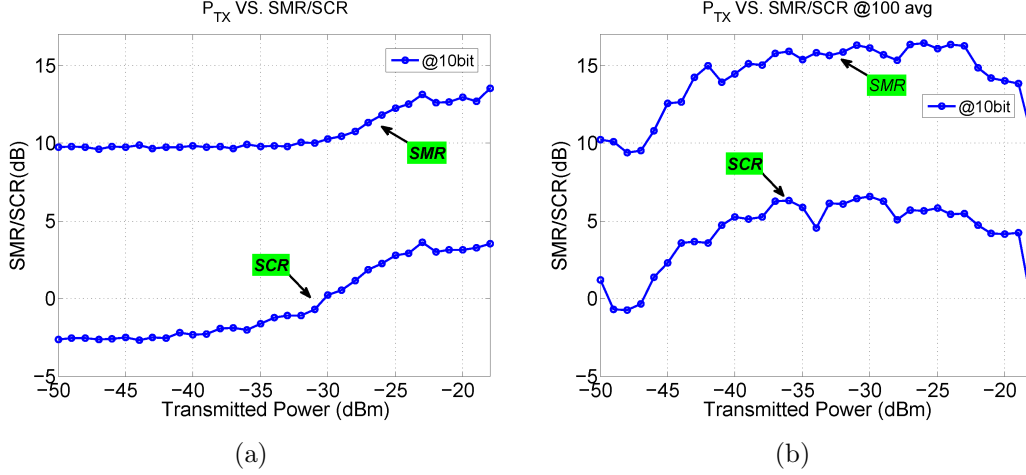
Figure 4.12. CETS receiver system performance (SMR, SCR) with SFCW approach with different signal power, with 10-bit ADC and thermal noise; results are reported both for a single evaluation (a) and for an averaging on 100 trials (b).

Jitter

Simulations are performed sweeping the rms timing jitter variance, from 0 to 6 picoseconds. The simulation results in Figure 4.13(a) are referred to the case without average. The depicted curves present the results with -28 dBm as the transmitted power, and 10-bit as ADC resolution. Here, the impact of jitter is obvious since SMR and SCR decrease dramatically and approach the working threshold values when rms jitter variance is 2 ps. However, results with 100 times average are quite good, as shown by curves in Figure 4.11(b), which prove the CETS receiver is considerably robust to jitter influence. PLL with 2 ps rms jitter can be achieved, as shown in [60].

4.4.3 CETS receiver with time domain approach

In this scenario, instead of transmitting a series tones of variable frequency, a single gaussian pulse with ultra-wide-band is transmitted.

ADC

Since the ADC resolution for the CETS receiver has already been decided in previous simulations, the focus of this analysis will be put on the performance with this 10-bit
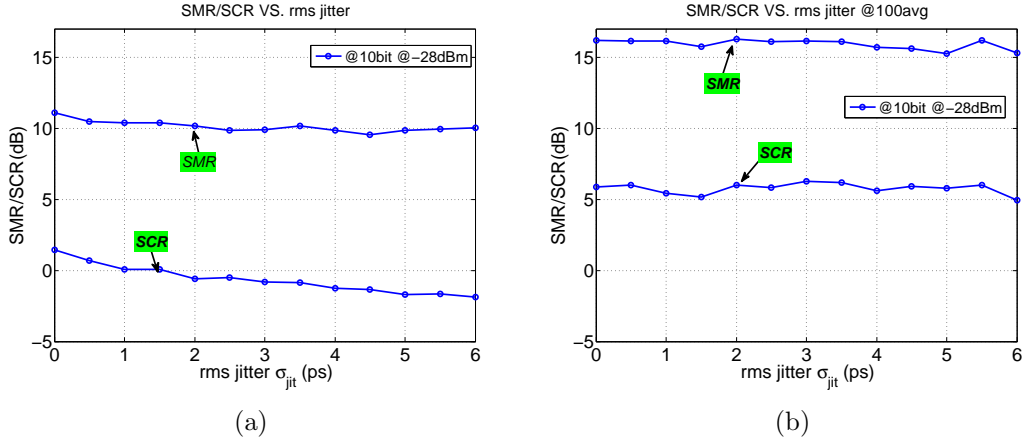
Figure 4.13. CETS receiver system performance (SMR, SCR) with SFWC approach and with different rms jitter, with 10-bit ADC and -28dBm transmitted signal power; results are reported both for a single evaluation (a) and for an averaging on 100 trials (b).
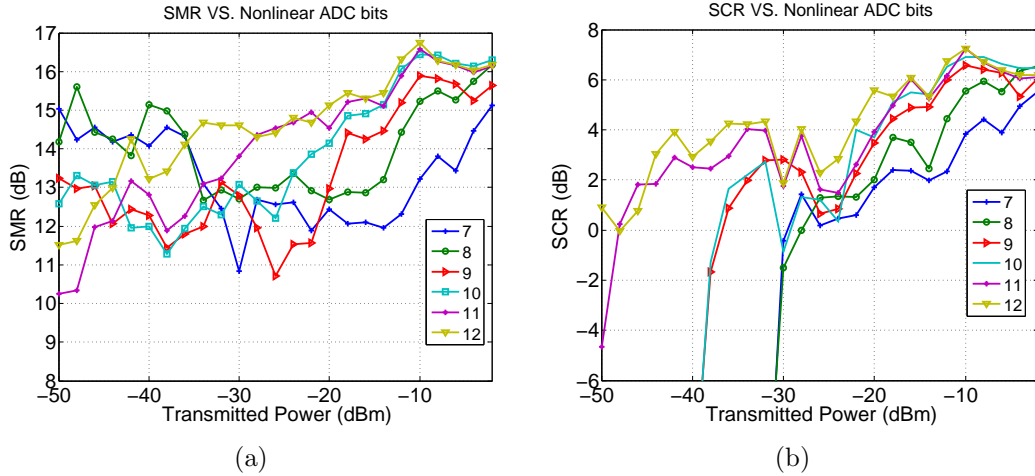
Figure 4.14. CETS receiver system performance (SMR, SCR) with different signal power and ADC bits; results are reported for a nonlinear ADC.

ADC. The transmitted signal level is scaled from -50dBm to -2dBm as defined in Section 4.3. As can be seen from Figure 4.14, 10-bit is also a good choice in this kind of application when transmitted power is greater than -20dBm, based on the rule that SMR is meaningful if and only if the corresponding SCR is bigger than 0dB.

Thermal noise

In this specific application, thermal noise is expected to be the big performance degradation contribution, because the noise without filter is added to the time domain signals directly before quantization; moreover, the sampled digital signals after resorting are processed by imaging reconstruction algorithm directly, without any further processing step, like FFT in CETS receiver with SFCW approach.

Figure 4.15 (a) proves this hypothesis, the noise influence is significant. The system starts working if and only if transmitted power is bigger than -10 dBm without average. After 100 times average, Thermal noise is dramatically reduced, the working threshold power becomes -30 dBm, the SMR and SCR values increase monotonically with the power to 16 dB and 5 dB respectively. Figure 4.15 (b) indicates that the needed power for good performance is at least -20dBm.

Note that, unlike the previous two scenarios, nonlinearity and saturation exhibit less impact on the system performance at high signal power. Since the reflected pulse is a combination of skin reflection and tumor response in time, the skin reflection appears early and performs strong, on the contrary, tumor information appears later in time and behaves much weaker. Most of the distortions are due to the strong skin response and are display common to all the received signals at different antennas, as the same distance between antennas and skin is applied, and they are effectively removed by the following skin artifact calibration [33].
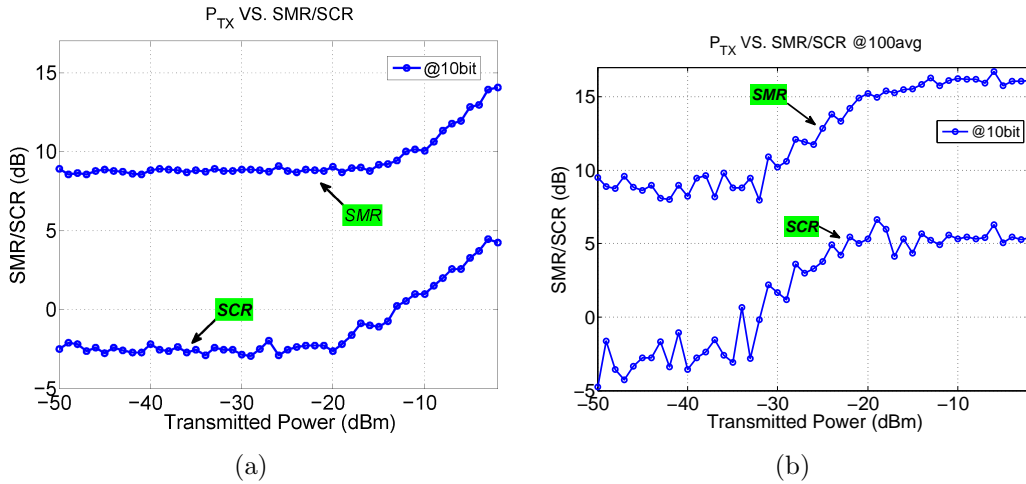
Figure 4.15. CETS receiver system performance (SMR, SCR) in time domain with different signal power and 10-bit ADC; results are reported both for a single evaluation (a) and for an averaging on 100 trials (b).

87

Jitter

RMS jitter is now included in the model, and varied from 0 to 6 picoseconds. Results are shown in Figure 4.16, which are obtained using -10 dBm transmitted power, 10-bit ADC and 100 iterations. As expected, results with averaging (b) are way better than those obtained after a single trial (a), proving that jitter influence can be removed in CETS even with a time domain approach.
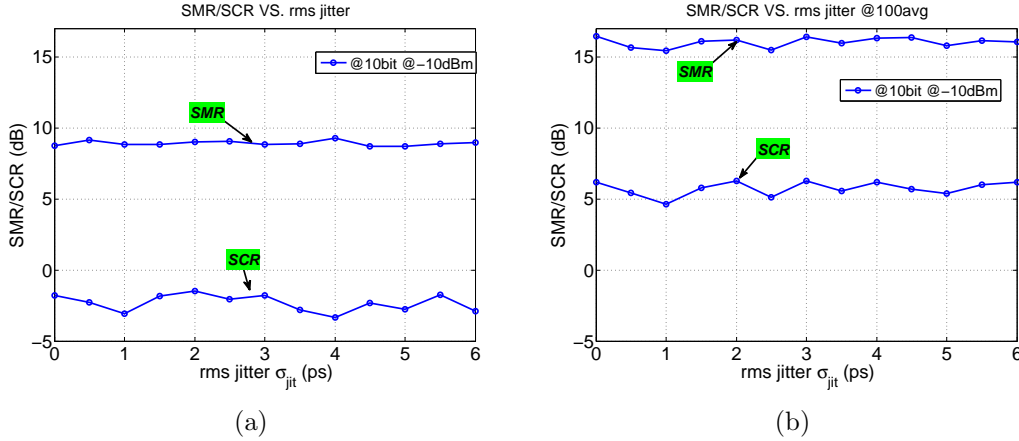
Figure 4.16. CETS receiver system performance (SMR, SCR) in time domain with different rms jitter, with 10-bit ADC and -10dBm transmitted signal power; results are reported both for a single evaluation (a) and for an averaging on 100 trials (b).

4.4.4 Overall comparison

The simulated quantitative results (SMR, SCR) for three different scenarios (DC, CETS receiver at frequency mode and CETS at time mode) are summarized in Table 4.3, along with selected receiver parameters. The corresponding energy maps generated by imaging algorithm are illustrated in Figure 4.17, the maximum energy peaks are enclosed.

For the DC receiver with SFCW approach, the results are obtained under the condition of phase mismatch equal to 2^0, transmitted power is -28 dBm, ADC resolution is 15-bit, phase noise is 0.1^0, the total gain of receiver is 40 dB, a NF is 10 dB, S11 of antenna is -10 dB, insertion loss and isolation of circulator is -2 dB and -18 dB respectively and the IIP2 and IIP3 are 20 dBm and -20 dBm respectively. Compared to the ideal case, SMR and SCR without average decrease by 3.7 dB and 3.7 dB, respectively. Maps are in Figures 4.17 (a)-(b), it is clearly to see that averaging removes many clutters from the image, the tumor is evident. So in conclusion,

DC receiver needs averaging to achieve high performance but averaging increases the data acquisition time.

Results for the CETS receiver with SFCW approach are obtained with $2\,ps$ RMS jitter, 10 bits ADC, -28 dBm transmitted power. The energy map in Figure 4.17 (c) shows a lot of clutters, the energy peak appears in many places, tumor is hard to be identified, while SMR and SCR values tell us the same results. On the contrary averaging improves results and seems to be more effective than in the DC case, as SMR and SCR decrease by only 0.2 dB and 1.0 dB about the ideal case.

Concerning CETS in time domain, the receiver parameters are set equal to the SFCW case except for the 10 GHz effective noise bandwidth. The quantitative results indicate that the tumor can not be detected without average, we can not identify the tumor from the map in Figure 4.17 (e) either. The map after averaging in Figure 4.17 (f) is instead very clear. Performance results are the closest to the ideal case: SMR decreases by 0.3 dB, and by 0.7 dB for SCR.

At last, another comparison parameter for the three scenarios is considered, data acquisition time. For CETS in time domain with 8 ns pulse repetition time and 251 pulses required for a single acquisition, the total acquisition time with averaging is only $200\,\mu s$. The same time is needed for one frequency tone in case of CETS with SFCW, but 81 frequencies are acquired, leading to a total acquisition time of 17 ms. The baseband filter with 100 KHz bandwidth used in DC receiver may have around $4\,\mu s$ rise time, therefore it is reasonable to assume $10\,\mu s$ acquisition time for each frequency. The acquisition time for 81 tones is thus about $800\,\mu s$, and as a consequence the total capture time is about $80\,ms$ in case of 100 iterations. Therefore, the proposed CETS receiver working with impulse radar approach can obtain better results with less acquisition time.

	ideal	DC		CETS–Freq.		CETS–Time	
	no avg	no avg	avg	no avg	avg	no avg	avg
SMR	16.5	12.8	15.2	10.2	16.3	9.0	16.2
SCR	7.0	3.3	5.6	-0.6	6.0	-1.5	6.3

Table 4.3. SMR, SCR for the three scenarios.
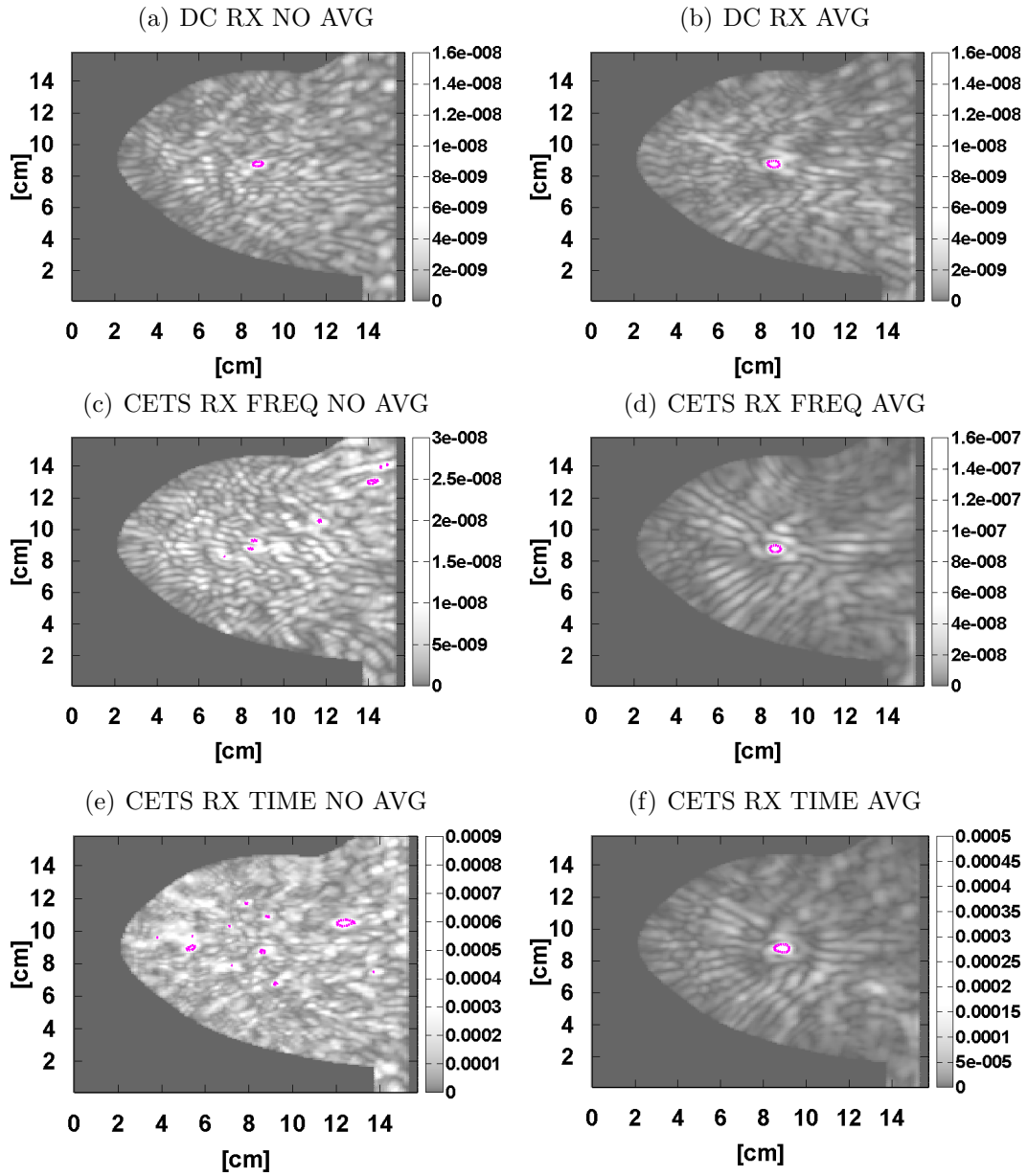
Figure 4.17.   Energy maps resulting from the system-level simulations with different receiver approaches and all the impairments. Maps (a)-(b) are for DC with SFCW approach, (c)-(d) for CETS with SFCW approach, (e)-(f) for CETS in time domain. The left column maps (a)-(c)-(e) are without average, the right ones (b)-(d)-(f) are acquired 100 times and averaged.

Chapter 5

Hardware Implementations

Considering the receiver requirements on bandwidth, resolution and sampling frequency, the most critical blocks in the proposed CETS receiver are LNA and THA. In this chapter, specific LNA and THA are designed for the CETS receiver in 130 nm UMC CMOS technology. Moreover, an UWB slot antenna with HFSS software is designed.

5.1 UWB antenna design

The primary goal of this section is to develop a planar, directional and physically compact UWB antenna for breast cancer detection system.

5.1.1 UWB antenna requirements

The antenna is developed keeping in mind a broad range of possible applications that can be achieved using this time domain impulse UWB radar transceiver. In addition to the parameters described above, the UWB antenna design faces some additional challenges as compared to other narrowband antennas.

First of all, even though the proposed signal bandwidth is 10 GHz in behavioral system simulation, after considering the complexity of the practical hardware design, the standard Ultra Wideband bandwidth 3.1-10.6 GHz is the designed bandwidth range. Consequently, an Ultra Wideband antenna must be operable over the entire 3.1-10.6 GHz frequency range which implies that the UWB antenna must achieve an impedance bandwidth of at least 7.5 GHz. Moreover, due to the very low transmission power spectral density of the UWB signals, high radiation efficiency for the antenna is required, which means that all types of losses, including dielectric and return loss should be kept very low. Another important parameter which must be

Physical Profile	Compact, preferably conformal, Low cost of manufacture
Operational Bandwidth	3.1-10.6 GHz
Radiation Efficiency	High, S11 < -10dB in the entire band
Radiation Pattern	Directional, Stable over the entire frequency range
Directivity and Gain	High
Group Delay	Constant throughout the operational bandwidth

Table 5.1.   UWB Antenna design requirements for UWB transceiver.

taken care of in the case of UWB antennas is the group delay. It gives an indication of the average time delay the input UWB signal suffers at each frequency. For distortion less signal transmission UWB antennas must have a constant group delay over the entire operational bandwidth. In narrowband antennas constant group delay is naturally achieved. The antenna requirements for the UWB transceiver are summarized in the Table 4.1.

5.1.2   Antenna design

The selection of an UWB antenna topology depends on the particular application for which it will be used. A wide variety of UWB antennas are available in literature for different UWB applications in which several antennas for microwave imaging system have been proposed, such as stacked patch antenna[61], Vivaldi[62], horn [55], monopole [63] and also other more antennas are designed and investigated in order to get the proper antenna. Although the popular pyramidal horn antennas is commercially available with an operational frequency band of 1-18 GHz, the large dimensions and high cost make this kind of antenna improper for breast cancer imaging applications.

Therefore, in this section, a wide slot antenna is investigated in which the slot width and length are comparable. The generic form of this configuration has been proposed in [64]. Slot antennas are well-known for their wide bandwidth and small size. In the following, a numerical study of a specific realization of this design is presented, wherein the antenna is customized to centimeter-scale dimensions for operation in the microwave frequency range from 3.1 to 10.6 GHz.

Figure 5.1 displays the top-view and side-view of the proposed wide-slot antenna. A wide slot with comparable width W and length L is placed in the ground plain on one side of the substrate with relative permittivity ε_r. The wide slot is fed by a microstrip line with a fork-like tuning stub, which is printed on the opposite side of the substrate and placed symmetrically with respect to the centerline of the wide slot. The fork-like tuning stub consists of a straight section of length (L2 plus

L4) and two branch sections of equal length. The space between the two branch sections is W5. The widths of these sections are all the same and equal to that of the microstrip line W3. By selecting proper dimensions of the fork-like tuning stub, good impedance matching of the printed wide-slot antenna across a much enhanced bandwidth can be obtained. In this case, 50 Ohm impedance matching is used.
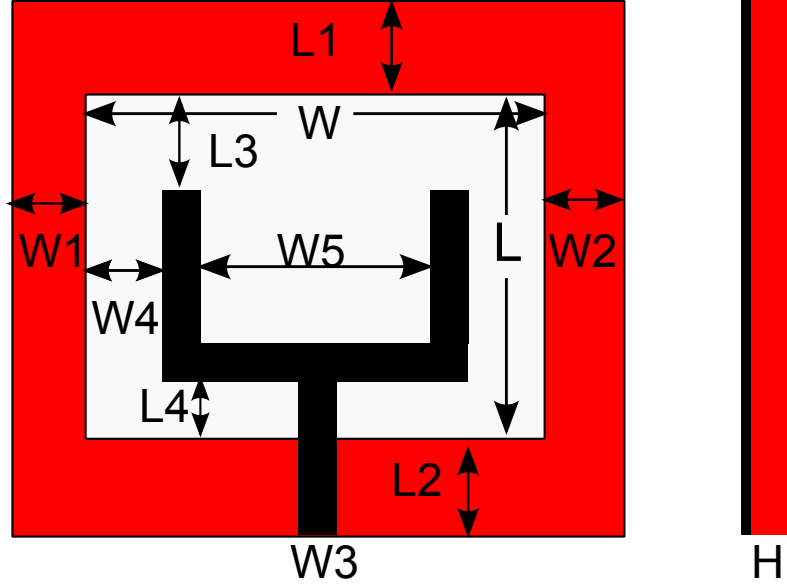
Figure 5.1. The layout of the developed slot antenna.

The first step in the design is to choose a suitable dielectric substrate of appropriate thickness and loss tangent. To begin with, the relationship between thickness H and dielectric constant of the substrate should be compromised. The operation bandwidth improves as the substrate thickness is increased, or the dielectric constant is reduced, but these trends are limited by an inductive impedance offset that increases with thickness [65]. On the other hand, in order to minimize the antenna size, the substrate dielectric constant should be bigger [64], which is an important requirement of breast cancer application.

A logical approach, therefore, is to use a high dielectric constants and a thick substrate. Rogers RT/duroid 6010/6010LM with relative permittivity $\varepsilon_r = 10.2$ and dielectric loss tangent $\tan \delta = 0.0023$ is applied.

Next, based on this relative permittivity and height of substrate, in order to obtain 50 Ohm impedance matching, the relationship between the microstrip line width and the impedance can be calculated in two conditions.
When $W/h \leq 1$

$$Z_c = \frac{\eta}{2\pi\sqrt{\varepsilon_{re}}} \ln(\frac{8h}{W} + 0.25\frac{W}{h})$$

$$\varepsilon_{re} = \frac{\varepsilon_r + 1}{2} + \frac{\varepsilon_r - 1}{2}[(1 + 12\frac{h}{W})^{-0.5} + 0.04(1 - \frac{W}{h})^2] \tag{5.1}$$

When $W/h \geq 1$

$$Z_c = \frac{\eta}{\sqrt{\varepsilon_{re}}}[\frac{W}{h} + 1.393 + 0.677\ln(\frac{W}{h} + 1.444)]$$

$$\varepsilon_{re} = \frac{\varepsilon_r + 1}{2} + \frac{\varepsilon_r - 1}{2}(1 + 12\frac{h}{W})^{-0.5} \tag{5.2}$$

Where ε_{re} is effective dielectric constant, ε_r is relative dielectric constant, Z_c is the characteristic impedance.

The slot antenna is designed and optimized using the CAD tool HFSS v10. During simulation, the ground plane and the microstrip line are assigned as the Perfect E boundary. This type of boundary forces the electric field (E-Field) perpendicular to the surface. Besides, Lumped port is applied as the excitation port. The excitation port is a type of boundary condition that permits energy to flow into and out of a structure, and Lumped Port is useful for modeling internal port within a structure. In order to find best values for different antenna parameters, a number of simulations have been run within the given frequency range 2GHz to 12GHz in HFSS. The best parameters found after parametric optimization in HFSS are listed in Table 5.2. The layout of the antenna in HFSS is shown in Figure 5.2, the total size is $22\,\text{mm} \times 19\,\text{mm} \times 1\,\text{mm}$.

5.1.3   Results and discussion

Reflection coefficient

First, the fundamental parameter impedance matching is simulated, which is used to characterize the impedance bandwidth of an antenna. Figure 5.3 (a) depicts the amplitude of the simulated return loss, for the -10 dB return loss, the measured maximum impedance bandwidth of the proposed antenna is from $2.5\,\text{GHz}$ to $10.8\,\text{GHz}$, which satisfy the good impedance matching requirement. The sharp nulls in the plot correspond to the frequencies that attain the highest resonance. These points indicate a near perfect match to $50\,\text{Ohm}$. Figure 5.3 (b) shows the corresponding phase response of the antenna.

Material Rogers RT/duroid 6010/6010LM	$\varepsilon_r = 10.2 \tan \delta = 0.0023$
Height H	1 mm
Slot width W	17 mm
Slot length L	15.5 mm
Microstrip width W3	1 mm
L1	3.5 mm
L2	3 mm
L3	4.5 mm
L4	4 mm
W1	1 mm
W2	1 mm
W4	4 mm
W5	7 mm

Table 5.2. The dimension and parameter of proposed antenna in millimeters.
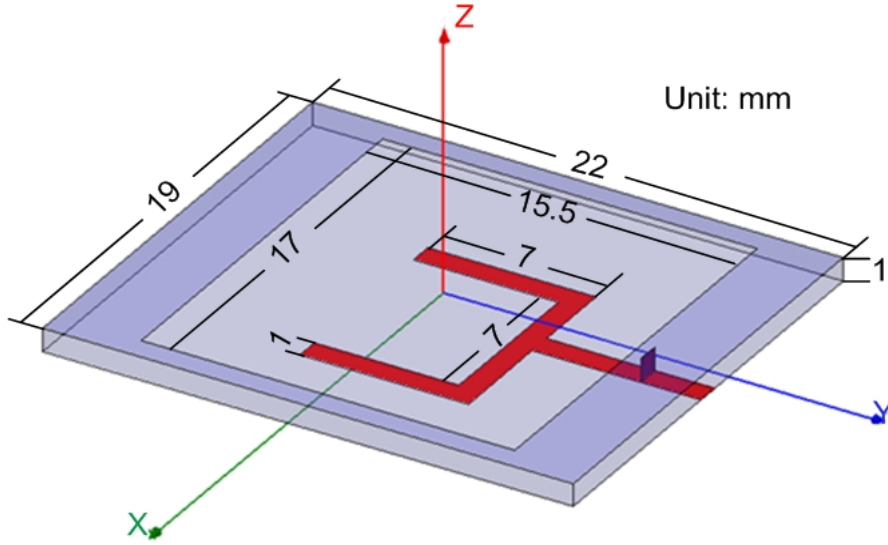
Figure 5.2. Overview of the slot antenna in HFSS.

Radiation pattern

An input matching is only one requirement for the antenna, radiation patterns are also important over the full band of operation. Antenna radiation pattern demonstrates the radiation properties on antenna as a function of space coordinate. The
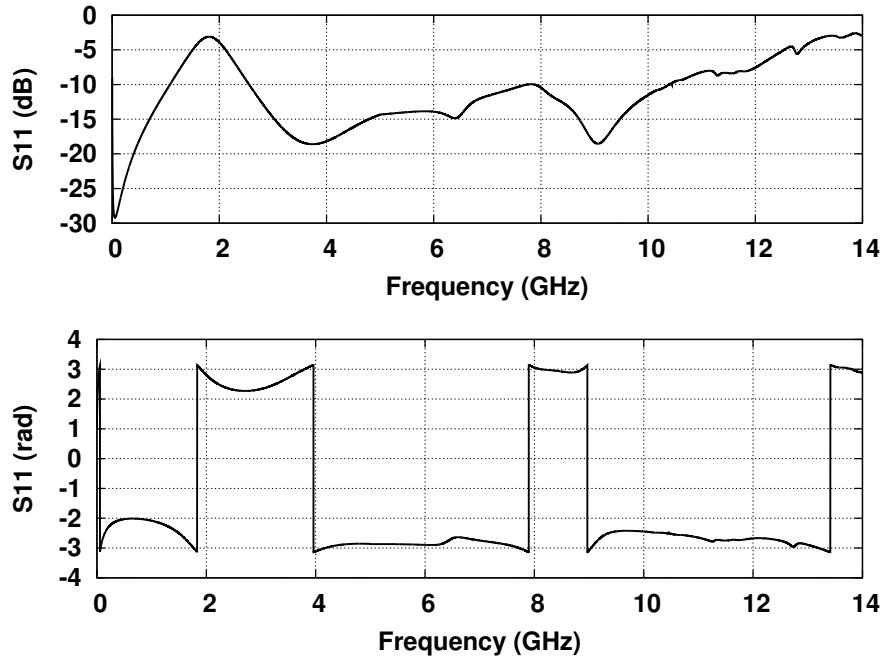
Figure 5.3.   Simulated return loss against frequency.

gain in the z direction (maximum gain direction in the radiation pattern) ranges from 3.2 dBi to 5.9 dBi within the operating bandwidth of the antenna, and the peak gain is at 9GHz. Typical radiation patterns is plotted in Figure 5.4.

Time domain analysis

In order to validate the efficiency of the antenna, the pulse base signal is excited with Gaussian pulse. Figure 5.5 shows the radiated E field which is virtually place probe in simulation to study the effect of radiated signal. It is proved that the proposed antenna has good potential in transmitting UWB signals with minimum distortion and late-time ringing. Furthermore, the time domain UWB pulse signal received by the electric probe shows stable performance where the received pulse signal is almost identical to the transmitted pulse signal.

The above results show that the proposed wide slot antenna has a good impedance matching, well more than the entire UWB range (7.5 GHz). Furthermore, the wide slot antenna has much smaller size than other type of antennas. Simulated radiation patterns confirm good directional radiation performance over the entire UWB range.
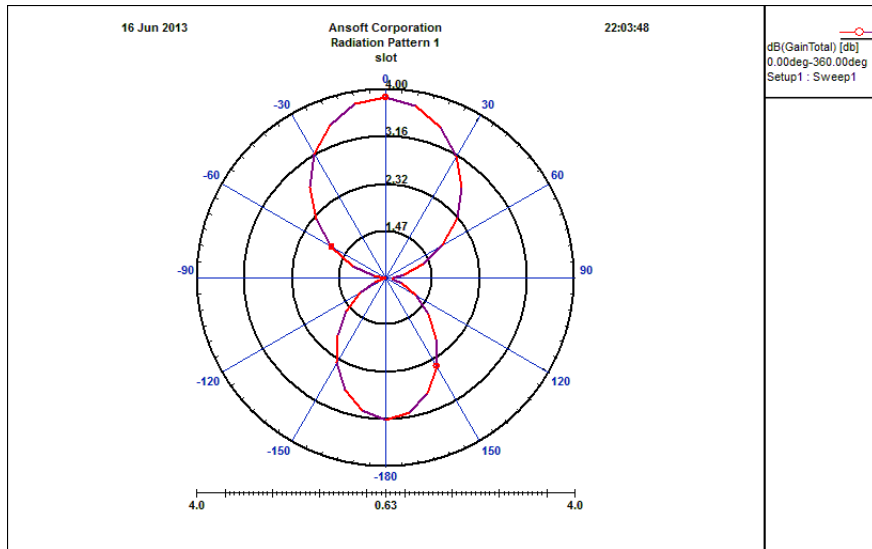
Figure 5.4.   Radiation pattern.
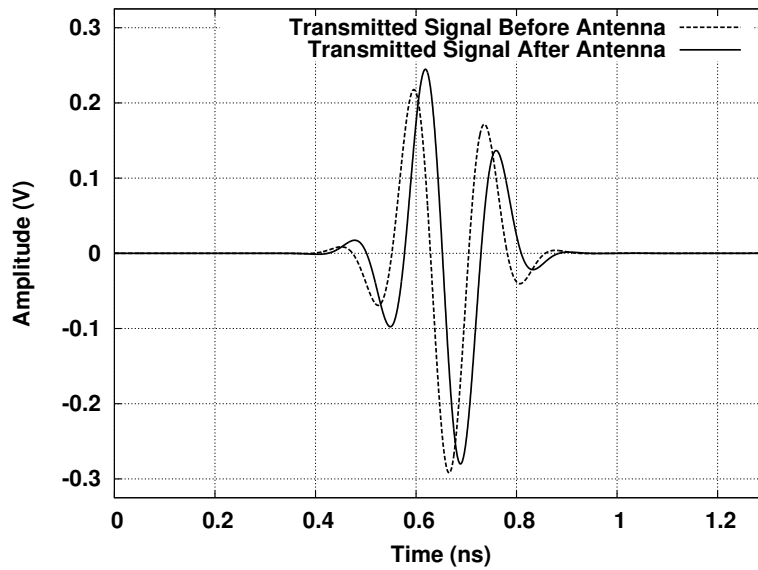
Figure 5.5.   Calculated electric field waveforms.

5.2   Low Noise Amplifier

As the first block in receiver, the purpose of the low-noise amplifier (LNA) is to amplify the weak RF-signal while adding a minimum noise.

97

5.2.1   Design consideration

As discussed in Chapter 4, the main concern of the proposed CETS receiver in time domain impulse radar approach is the influence of thermal noise. Based on the Friis' formula, the cascaded noise figure and third-order intercept point IP3 of a receiver can be expressed as:

$$F = F_1 + \frac{F_2 - 1}{G_1} + \frac{F_3 - 1}{G_1 G_2} + ... + \frac{F_N - 1}{G_1 G_2 \cdots G_N}$$
$$IP3 = \frac{1}{\frac{1}{IP3_1} + \frac{G_1}{IP3_2} + \frac{G_1 G_2}{IP3_3} + ... + \frac{G_1 G_2 \cdots G_N}{IP3_N}}$$

(5.3)

where F_i, $IP3_i$ and G_i ($i = 1,2,...N$) are the noise figure, third-order intercept point and gain of each individual component in the RF chain.

Therefore, the noise figure and gain of the first component in receiver, LNA, are important. The overall noise figure of the receiver caused by the second component, THA, is reduced by the gain of the LNA, as well as nonlinearity behavior. But the high gain may cause a potential problem that strong signals in the bandwidth of the amplifier may drive it into saturation and generate spurious frequencies.

To sum up, considering that the received pulse has ultra wide bandwidth (3.1 GHz to 10.6 GHz) and small tumor information amplitude, the main specifications of LNA are the following: the LNA input impedance must be matched as closely as possible to the antenna characteristic impedance over the entire bandwidth to guarantee the maximum power transfer; the LNA must exhibit the flat gain behavior over the entire bandwidth with sharp roll-off at the upper and lower -3 dB frequencies to prevent out-of-band interference; the LNA must have a high conversion gain to amplify the weak tumor information; the noise figure (NF) should be low enough to identify important information from noise interference. Nevertheless, it must offer robust RF performance (i.e., gain and dynamic range) over many gigahertz of bandwidth (7.5 GHz) with levels of current consumption comparable to existing narrowband amplifiers.

In recent times, many literatures have reported UWB LNA circuit designs with various approaches to impedance matching and involving lower noise. Table 5.3 illustrates the recent researches in UWB LNA.

5.2.2   UWB LNA design

There are two popular architecture choices for input matching, common-source topology and common-gate topology. Most reported common-source structure can provide acceptable gain and input matching while dissipating rather low power. However, these common-source UWB LNAs tend to show unacceptably high noise figure (NF) at high frequencies (near 10 GHz) due to the strong cutoff frequency

Ref	Technology	Gain (dB)	BW (GHz)	NF (dB)	S11 (dB)	Power (mW)
[66]	0.13 μm CMOS	11	2-9.6	3.6-4.8	< -9.5	19
[67]	0.18 μm CMOS	9.5	3.1-10.6	5-5.6	< -8.6	9.4
[68]	0.18 μm CMOS	9.7	1.2-11.9	4.5-5.1	< -11	20
[69]	0.13 μm CMOS	15.1	3.1-10.6	2.1-2.53	< -9	9
[70]	0.13 μm CMOS	16	2.9-11	3.8-4.0	< -10	9.5

Table 5.3.   Researches in UWB LNA.

dependence [71]. Instead, common-gate topology is benefited from its better input matching, inherent wideband operating performance, good linearity and input-output isolation property [72].

Figure 5.6 and Figure 5.7 show a typical inductively degenerated common-source LNA (CS-LNA) and a common-gate LNA (CG-LNA).
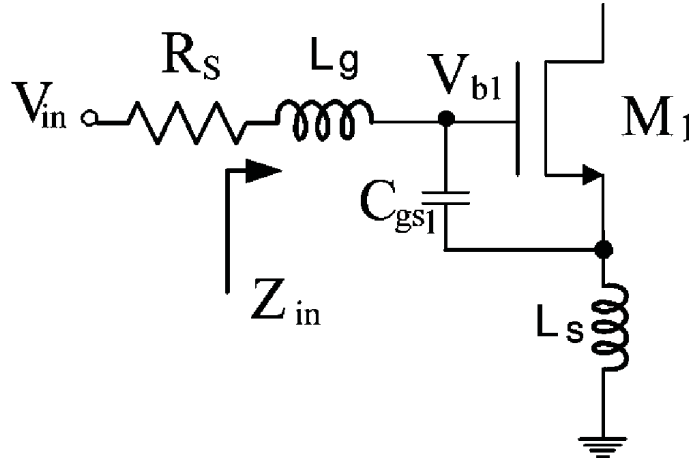
Figure 5.6.   Typical inductor-degenerated common source LNA [73].

The corresponding input impedance of Figure 5.6 can be expressed as,

$$Z_{in}(s) = \frac{s^2 + s\frac{g_{m1}L_s}{(L_s+L_g)C_{gs1}} + \frac{1}{(L_s+L_g)C_{gs1}}}{s/(L_s + L_g)} \tag{5.4}$$

The corresponding input impedance of Figure 5.7 can be expressed as,

$$Z_{in}(s) = \frac{s/C_{gs1}}{s^2 + s\frac{g_{m1}}{C_{gs1}} + \frac{1}{L_sC_{gs1}}} \tag{5.5}$$
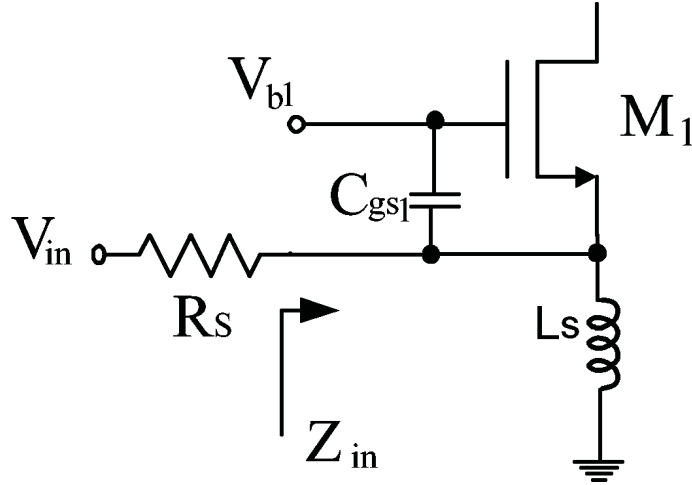
Figure 5.7.   Typical common gate LNA.

Where C_{gs1} is the parasitic gate-to-source capacitance of the input transistor.

As thermal noise is the most important impairment in the CETS receiver, more attention being paid to it. The NF of the CS-LNA is generally superior to that of the CG-LNA at lower frequency, because the CG-LNA's NF is limited by $1/g_m$ input matching. But, the NF of CS-LNA is proportional to ω_0/ω_T, while the NF of CG-LNA is constant with respect to ω_0/ω_T. Therefore, the CG-LNA outperforms CS-LNA in the higher frequency.

Taking advantage of the common gate topology, as above mentioned, and taking inspiration from a single-ended LNA in [70], a fully differential LNA is proposed. The schematic is shown in Figure 5.8. Compared to [70], this LNA occupies less area, one of the reasons is that two inductors in the original circuit are removed.

As the circuit in Figure 5.8 is a total symmetrical structure, it can be considered as a single-side circuit when discuss it. The proposed common gate wide-band Low Noise Amplifier (LNA) consists of three stages, a common-gate stage, a common-source stage and an output buffer. The common-gate stage provides input matching and wide-band noise. The second stage use cascode to extend the overall amplifier bandwidth and gain and the output buffer is a source follower for measuring purposes.

The circuit has been designed with UMC CMOS 130 nm technology. All inductor, resistors and capacitors are implemented on chip. Various pre-characterized active and passive components that UMC makes available through their design library are used.

The first stage is critical since it should match with source impedance to get

Figure 5.8. Proposed differential UWB LNA.

maximum power transfer and minimum reflection. Its noise figure must be kept under control, because the overall noise is mostly determined in this stage. The input impedance can be simplified as

$$Z_{in}(s) = sL1/(1 + (g_{m1} + sC_{gs1})sL1). \tag{5.6}$$

Where g_{m1} and C_{gs1} are the transconductance and the parasitic capacitance of transistor $M1$. Z_{in} is determined by inductor $L1$ at low frequency and is close to $1/g_{m1}$ at high frequency. $L1$ provides a DC path for the first stage, and combines with the parasitic capacitance C_{gs1}, which resonates and determines the input matching range and input impedance.

In addition, the gain of the first stage is determined by the size of $M1$ and $R1$. Input inductor $L1$ of $10\,\text{nH}$ (with $7\,\text{GHz}$ Self Resonant Frequency (SRF)) and input transistor $M1$ of $50\,\mu m/0.12\,\mu m$ are chosen to ensure the broad-band input matching condition. Figure 5.9 plots the simulated frequency response of this first stage. The optimal matching frequency is $1.2\,\text{GHz}$. The 3-dB bandwidth of the first stage is $0.36\,\text{GHz}$-$5\,\text{GHz}$ with the maximum gain of $14.9\,\text{dB}$ at $1\,\text{GHz}$.

The second stage is a simple cascode common-source stage, which provides high-frequency gain and determines higher 3-dB bandwidth of the LNA. The cascode transistor $M3$ is used for better isolation, higher frequency response and higher gain. A series peaking inductor $L2$ will resonate with the parasitic capacitance of $M3$ and $M5$ at high frequency. By optimizing the values of $L2$ and $R2$, the second stage can compensate the gain roll-off from first stage at high frequencies. Hence the

Figure 5.9.   Simulated frequency response of the first stage.

flat frequency response is obtained over the whole frequency band of interest. $L2$ in the second stage is 3.99 nH (with 14GHz SRF). Figure 5.10 displays the simulated frequency response of the second stage. The maximum gain of the second stage is 17.7 dB at 10 GHz and 3-dB bandwidth is 5.9 GHz-11 GHz.

$M4$ and $M5$ compose the output buffer. The output buffer is a simple source follower. In order to reduce the parasitic capacitance arisen from a large device, the input device of this buffer must be reduced despite larger loss occurs. The width and length of the input device $M5$ are set to 20 μm and 0.12 μm, respectively. The loss of the output buffer is 10 dB in this design for output impedance matching. These three stages have the same bias voltage, which simplifies the bias circuit. The dimensions of the circuit components are organized in the Table 5.4.

5.2.3   Simulation results and discussion

The LNA is simulated and designed in 0.13 μm CMOS technology with 1.2 V supply. The circuit has been simulated under Cadence design framework. Figure 5.11 (a) shows the input and output impedance matching performance ($S11$ and $S22$), which is less than -10 dB over the bandwidth from 500 MHz to 12 GHz. The maximum power gain with 50 Ω matched load is 17.2 dB and the reverse isolation is less than -55 dB, as shown in Figure 5.11 (b).
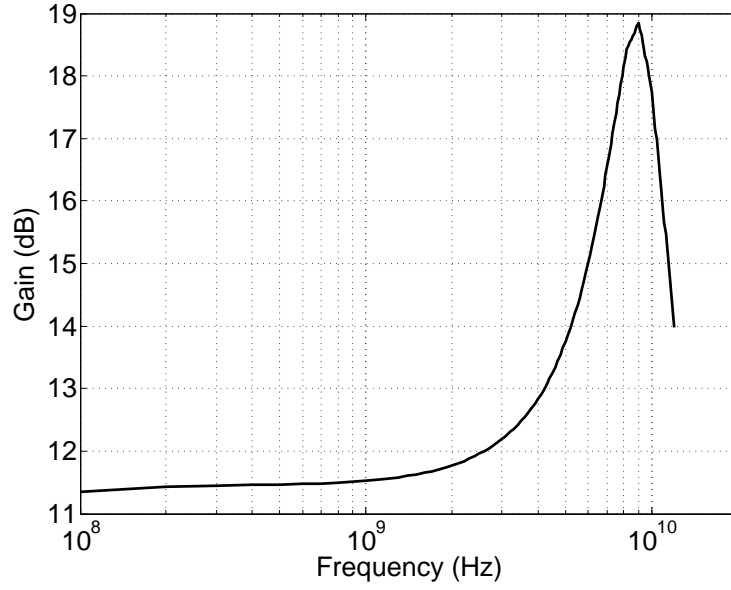
Figure 5.10.   Simulated frequency response of the second stage.

Component	value	unit
M1	50/0.12	μm
M2	34/0.12	μm
M3	20/0.12	μm
M4	30/0.12	μm
M5	20/0.12	μm
M3	4/0.12	μm
R1	510	Ω
R2	210	Ω
R3, R4, R5	10	$K\Omega$
C1, C2	10	pF
C3, C4	1	pF
L1	12	nH
L2	3.99	nH

Table 5.4.   Dimension of LNA components.

The simulated NF of the proposed LNA as a function of frequency is also presented in Figure 5.11 (c), which is improving with frequency. It is because the effect

103

of $L1$ on input matching and NF increases at high frequencies. This is also the advantage of common-gate topology over other architectures like common-source or cascode amplifiers, whose NF is increasing with frequency. In this LNA design, the NF values range from 3.1 to 4 dB between 2 and 12 GHz.

Two-tone test with 250 MHz spacing at various frequencies is implemented to examine the linearity performance of the proposed LNA. In the frequency range of 3-12 GHz, the IIP3 varies from -12 to -18 dBm, which is presented in Figure 5.12. As proved in Chapter 4, the nonlinearity problem exhibited less impact on the system performance in this specific application, given that the received reflected pulse is a combination of skin reflection and tumor response in time, the skin reflection appears early and performs strong, on the contrary, tumor information appears later in time and behaves much weaker. Most of the distortions are due to the strong skin response and display common to all the received signal at different antennas, as the same distance between antennas and skin is applied, and they are effectively removed by the following skin artifact calibration. Consequently, the requirement on nonlinearity is not that stringent.

The layout of the proposed LNA is shown in Figure 5.13. The input and output coupling capacitors occupy the majority area. Due to the reduction of the used inductors, the chip area is saved. Power consumption is 11 mW at 1.2 V and the chip area is 0.24 mm^2. The LNA performances are summarized in Table 5.5.

Table 5.5. Summary of the simulated LNA performances.

parameter	value
Technology	UMC $0.13\,\mu m$ CMOS
S11 (dB)	< -10
S22 (dB)	< -10
S12 (dB)	< -55
S21 (dB)	$14.5-17.2$
3dB bandwidth (GHz)	$0.5-12$
NF (dB)	$3.1-4$
IIP3 (dBm)	-15
Power consumption (mW)	11
Area (mm^2)	0.24
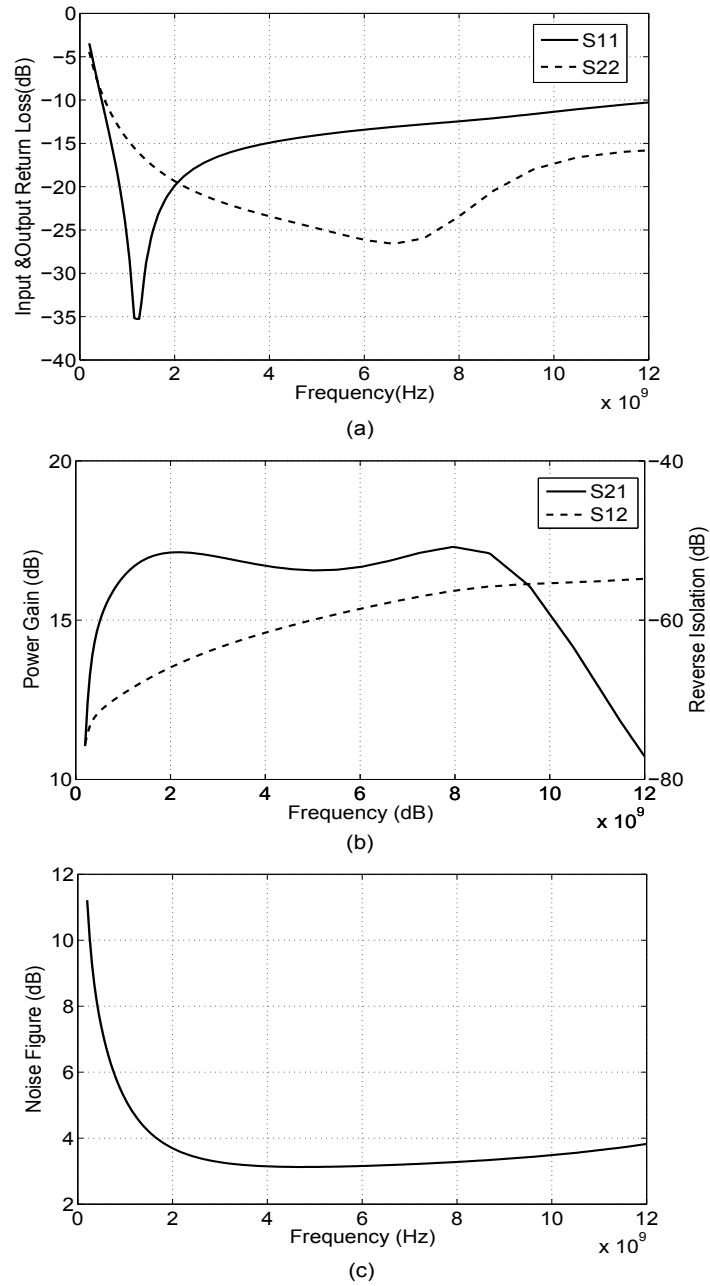
Figure 5.11. Simulated performance of the proposed LNA: (a) Input and output reflection coefficient (S11 and S22) of the UWB LNA versus frequency, (b) Gain and reversal isolation (S21 and S12) of the UWB LNA versus frequency and (c) Noise figure of the UWB LNA versus frequency.

105
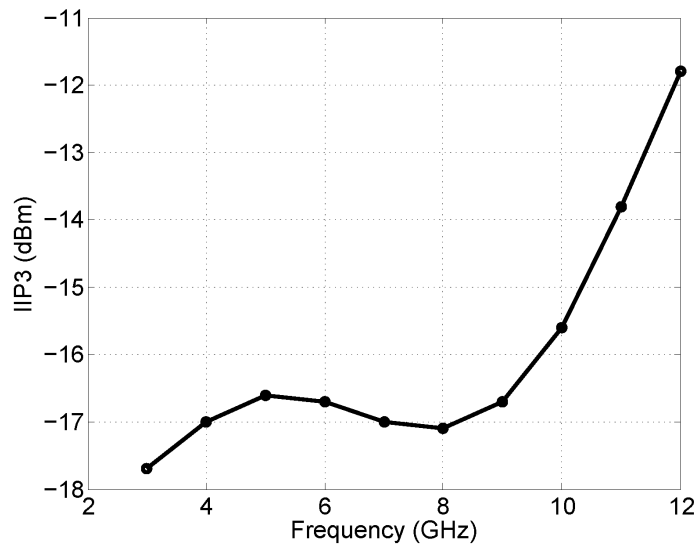
Figure 5.12.   Simulated IIP3 of the proposed LNA versus frequency.
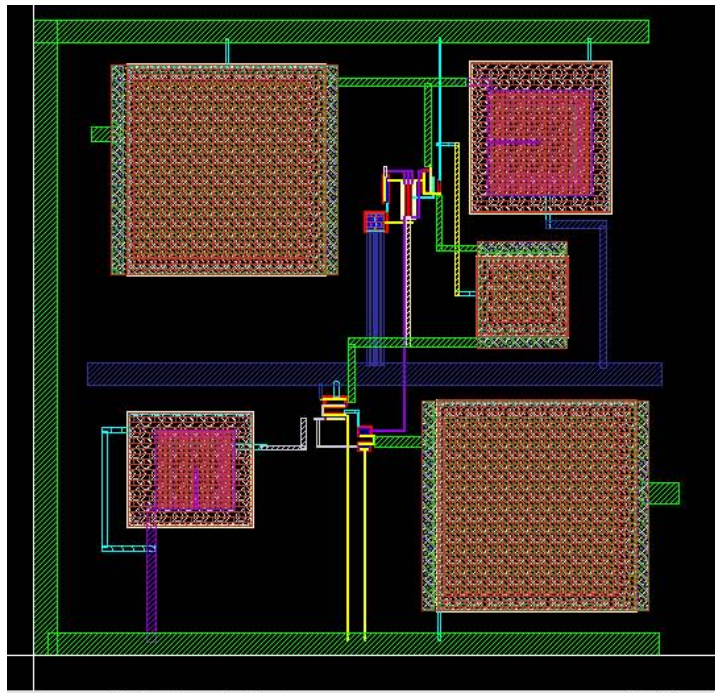
Figure 5.13.   Layout of the proposed LNA.

5.3   Track and Hold Amplifier

As mentioned in previous chapters, high speed data acquisition systems require ultra high-speed analog-to-digital converters (ADCs). The THA is a crucial building block in ADCs since it makes a great impact on the dynamic performance of ADCs.

5.3.1   THA design

Based on some simple differences in architecture, the topologies of THA can be classified as closed-loop topology, open-loop topology and distribute topology [74]. To achieve high speed operation, the open loop architecture switched source follower (SSF) is chosen [75] [76]. Therefore, to understand the principle of the SSF circuit, the simplest open-loop THA composes of two elements: a storage capacity and a switch (implemented with a MOS transistor) controlled by a clock. The simple circuits are illustrated in Figure 5.14.
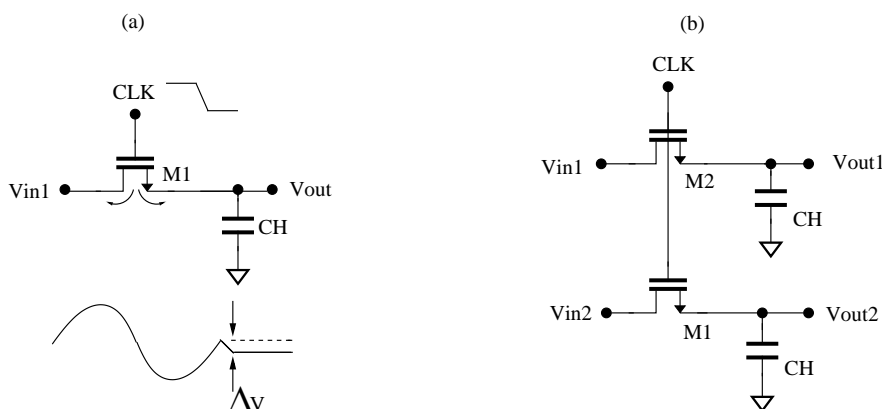
Figure 5.14.   Diagram of a simple circuit with THA differential switches in series (a) and its differential version (b) [76]

The circuit works at track mode when switch is on, and hold mode when switch is off. Even though this topology is characterized by simplicity, two problems should be concerned: one is the low velocity due to on-resistance of the sampling transistor; the other is that the output voltage is lower than the supply voltage due to the fact that a threshold voltage V_{gs} is necessary to turn on the transistor in track mode.

Consequently, the SSF structure was proposed to solve these problems, which is characterized by high speed and high linearity. The single-side structure is shown in Figure 5.15. This circuit consists of a differential pair (Q_N and Q_P), a current tail I_T, a switched source follower Q_{SF} and a hold capacitor C_H. In track mode, CLK_P is high, the tail current I_T flows through Q_{SF} and Q_P, transistor Q_{SF} acts

as a source follower and the output voltage V_{out} is linearly dependent on the input voltage V_{in}. In hold mode, CLK_N is high, the tail current I_T switches through the load R_L other than transistor Q_{SF}. The value of R_L is chosen such that the voltage drop $I_T R_L$ turns off transistor Q_{SF} and the hold capacitor C_H maintains the sampling voltage [75].
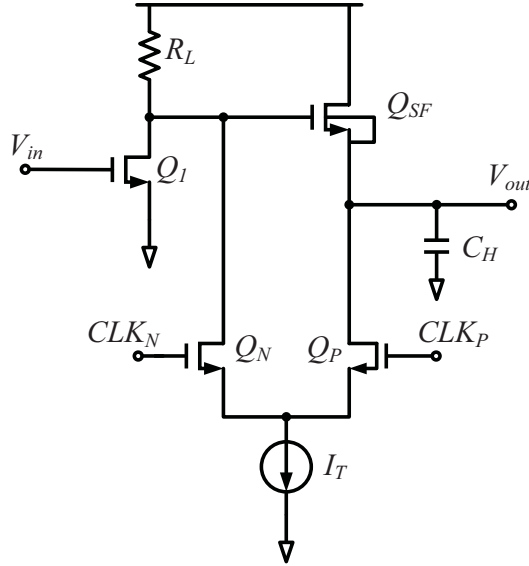
Figure 5.15.   A switched source follower track and hold amplifier

The main specifications of the required THA in the microwave imaging application are high-frequency operation in track mode (up to 10GHz), high-speed when moving from track to hold mode, and high linearity. In Figure 5.15, both the differential pair and the input buffer show highly linear behavior. There is inherent distortion in the SSF, which limits the performance of THA. Therefore it is necessary to improve the above existing architecture to suppress the effect of the distortion, improve linearity without renouncing speed. The proposed THA architecture is presented in Figure 5.16: differential circuits are used to solve the even harmonics problem and the odd harmonics are still exist.

A fairly effective method, harmonic-canceling technique, is applied to reduce the odd harmonics problem, which has been proved to be an effective way to increase the linearity of an amplifier or buffer [77] [78]. To implement the harmonic canceling technique, the nonlinearity of the input buffer is compensated by means of adding small transistors $M3$, $M4$ and $M6$.

In addition, if a standard source follower (Q_{SF}) is used, its large input capacitance would cause a high aperture time. To guarantee low aperture time without increasing power consumption, a modified source follower is proposed in Figure 5.17.

108
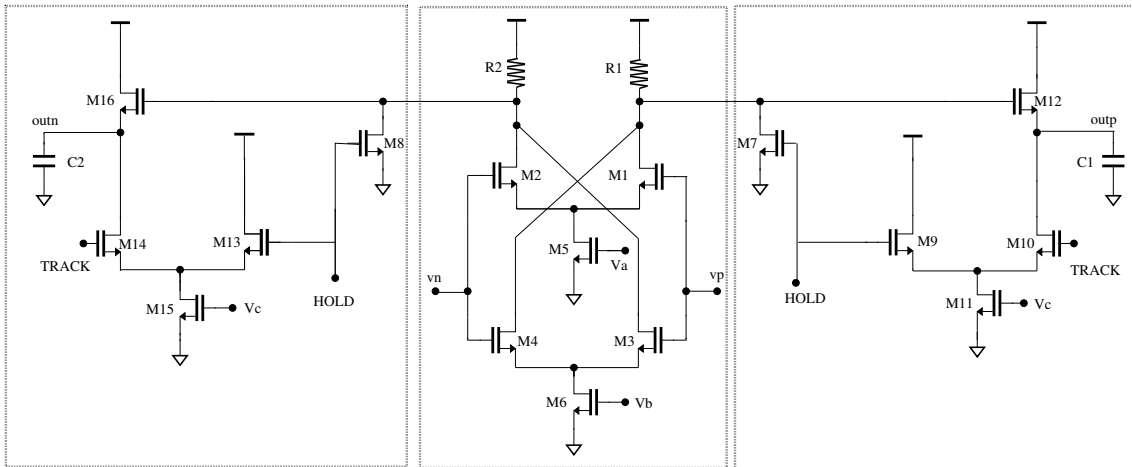
Figure 5.16.   Proposed high linearity THA

$M5$ (in Figure 5.16) or $M7$ and $M8$ (in Figure 5.17) are added and controlled by hold clock. In the track phase, $M12$ and $M16$ act as source follower. In the hold phase, $M7$ and $M8$ switch off $M12$ and $M16$, respectively, and their currents are deviated in $M10$ and $M13$.
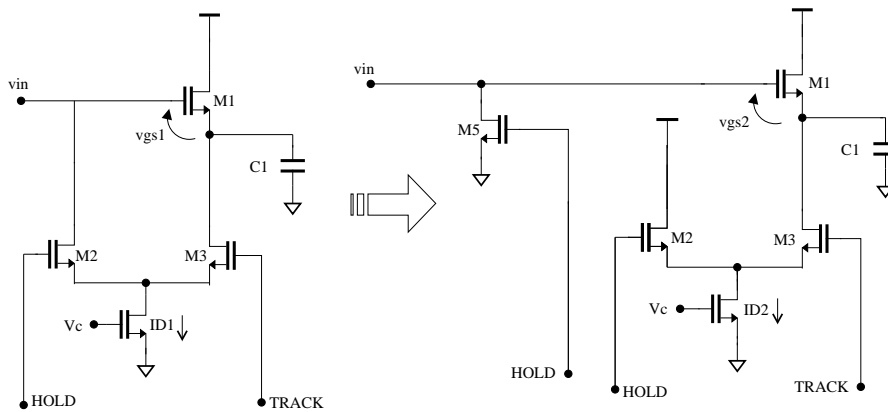
Figure 5.17.   Diagram showing the circuit innovations made to the basic scheme of Figure 5.15

The THA is simulated and designed in 0.13 μm CMOS process under Cadence design framework. The dimension of the circuit component are organized in the Table 5.6.

109

Component	value	unit
M1, M2	11.3/0.12	μm
M3, M4	3/0.12	μm
M12, M16	80/0.12	μm
M10, M14	5/0.12	μm
M9, M13	20/0.12	μm
M11, M15	20/0.12	μm
M7, M8	80/0.12	μm
M5	43/0.12	μm
M6	8/0.12	μm
R1, R2	175	Ω
C1, C2	200	fF

Table 5.6.   Dimension of THA components.

5.3.2   Simulation results

First of all, stand-alone simulations have been carried out in Cadence design framework to verify the transient behavior of the THA in track and hold mode. Figure 5.18 shows the transient simulation results of THA, the red line is track clock which has a period of 0.9ns, black one is the THA output with input frequency of 6GHz and the dotted blue one is the output under the condition of track clock always '1' and hold clock always '0' which shown as a reference. It is possible to see from Figure 5.18 that the circuit works very well in track and hold phases.

The simulated conversion gain of the proposed THA is shown in Figure 5.19. It has maximum gain of -2.5 dB and a bandwidth of at least 12 GHz when the circuit is operated in track mode.

The linearity of THA is characterized in terms of SFDR which is shown in Figure 5.20. In particular, the third harmonic distortion (the strongest) is less than -50 dB from 0 to 10GHz, while the fifth and seventh harmonic distortion are less than -65 and -70 dB, respectively. The layout of the proposed THA is shown in Figure 5.21.

Since in the receiver THA directly follows LNA, Figure 5.22 shows the circuit transient simulation results when both of them are simulated together. The track clock period is 1.9 ns, input signal frequency is 4 GHz. The blue line is the LNA input signal, the purple one is the output of LNA (input of THA) and the black one is the differential output of THA. The signal is correctly amplified and held.
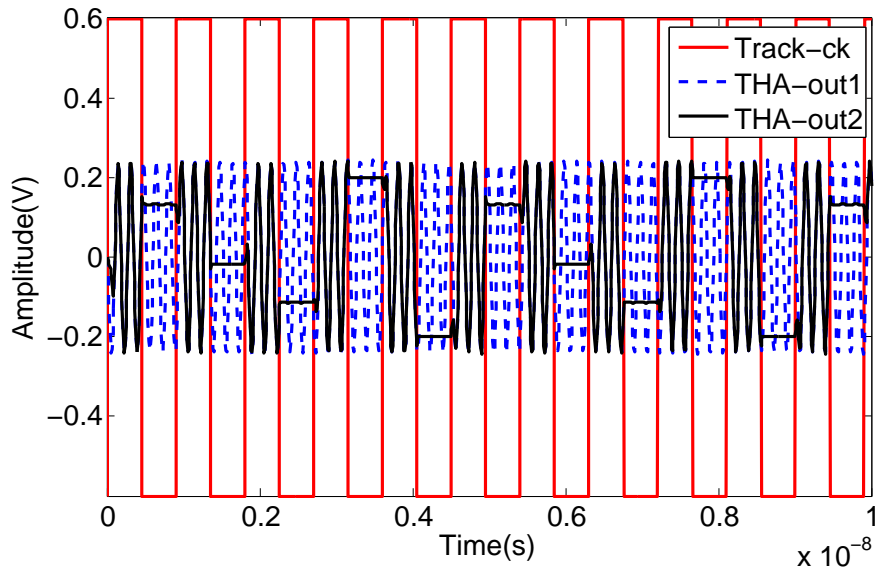
Figure 5.18.   THA transient simulation results
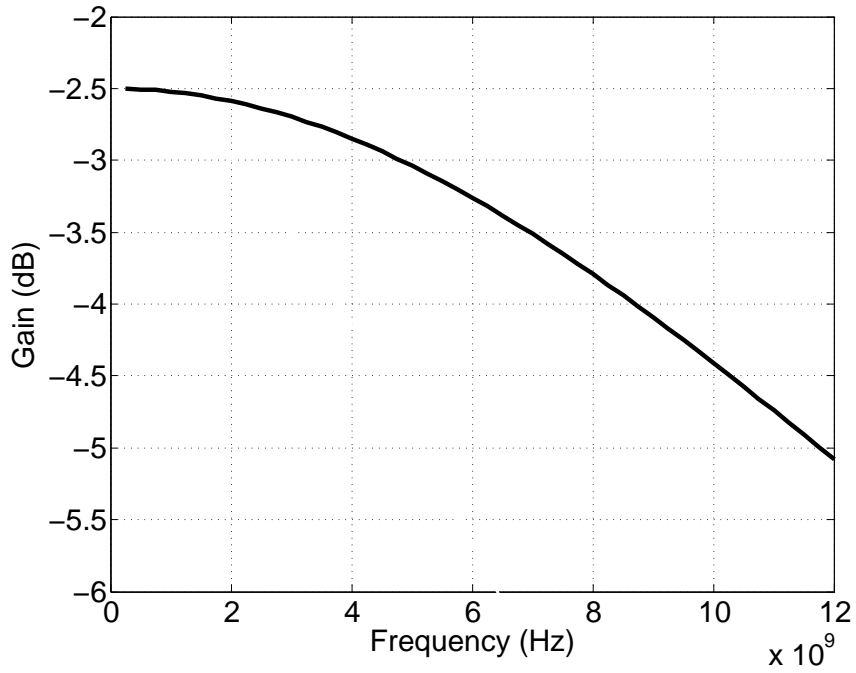
Figure 5.19.   THA AC simulation results
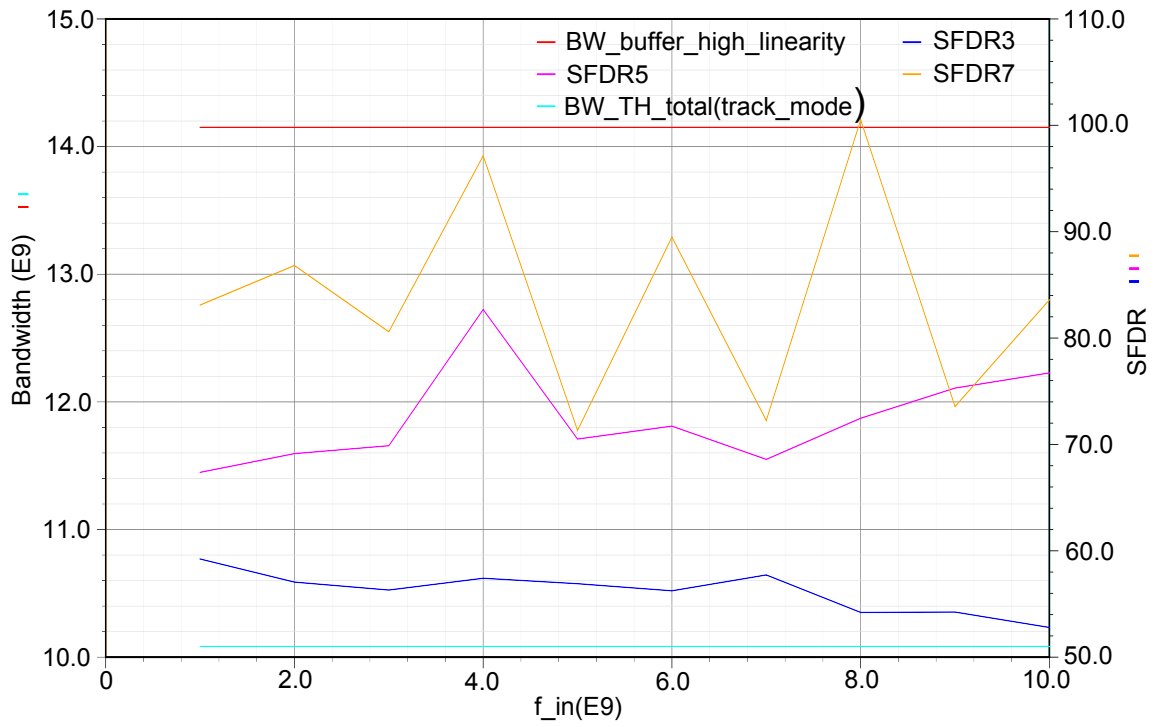
Figure 5.20.   THA linearity performance in terms of SFDR.
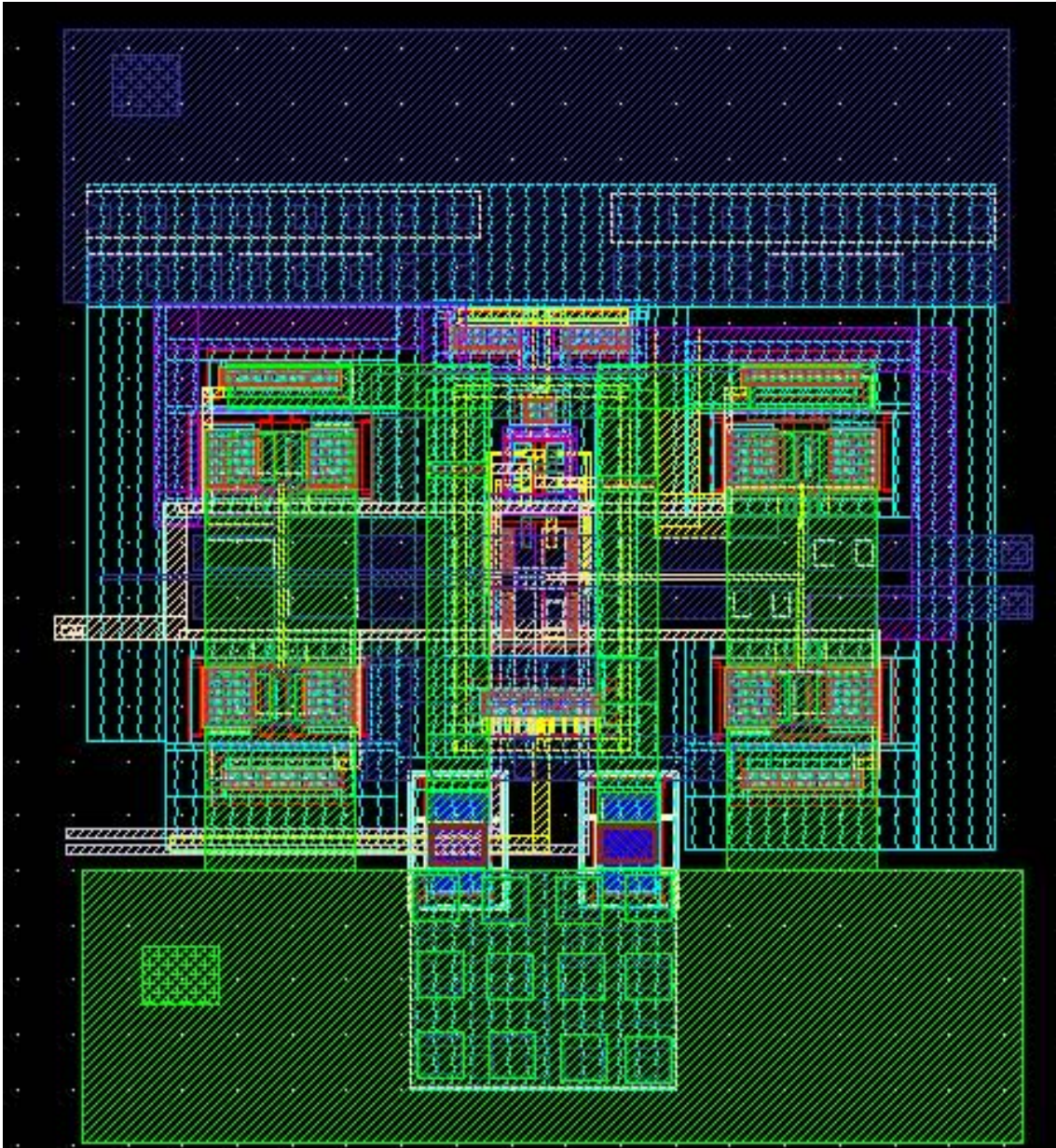
Figure 5.21.   Layout of the proposed THA.
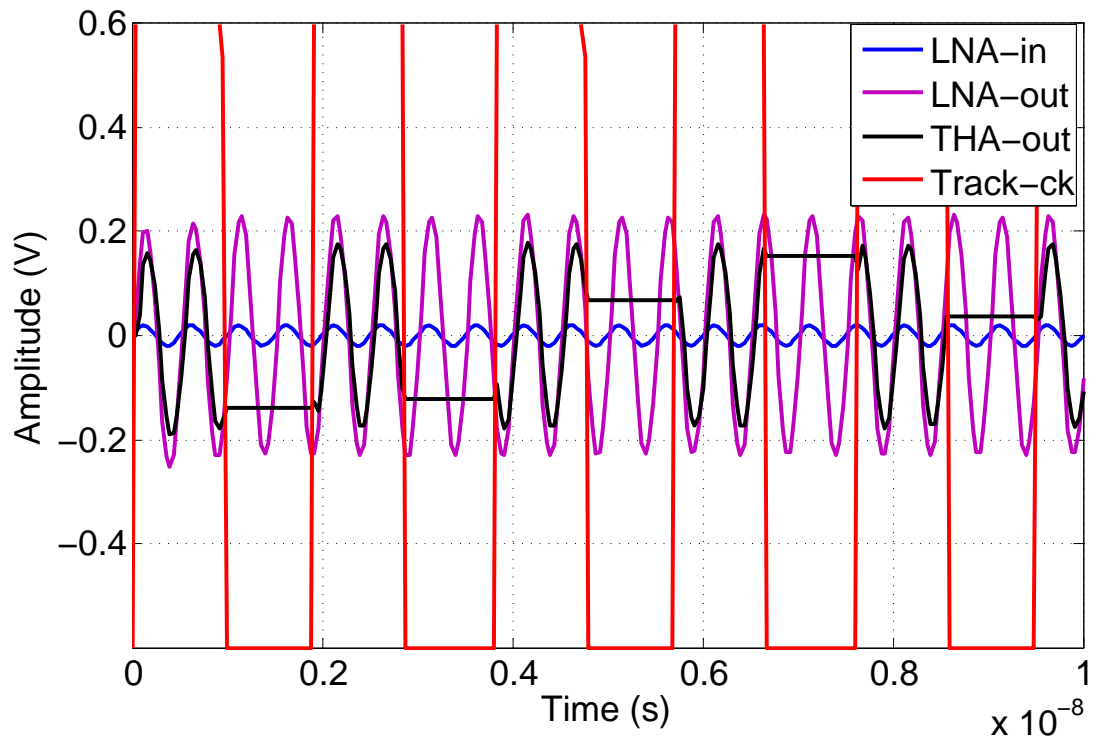
Figure 5.22.   Transient simulation results with both LNA and THA

Chapter 6

System performance evaluation

6.1 Introduction

In addition to present the circuit simulation results, the influence of the implemented circuit components with respect to the system performance is evaluated in this chapter. To achieve that, a multi-resolution methodology is applied. The first step of this approach is an *ideal model* of the entire environment, which comprises breast, antennas, transmitter, receiver and digital processing. High-level simulations with such models determine an ideal result, which is a performance upper bound, as illustrated in Chapter 3. Then, a progressive *refinement* of the design description allows evaluating the impact of non-idealities on system-level performance.

Unlike the behavioral functional modeling way of receiver in Chapter 4, the receiver is modeled block by block. Therefore, the designed circuit can be easily substituted by its netlist form. As an example, a designer can evaluate by how much a given system-level performance metric is influenced by circuit-level characteristics of the receiver low-noise amplifier (LNA), all the other components being ideal. The designer can then use this valuable feedback to optimize the design of the LNA. Key to achieve this result is a multi-resolution environment for the co-simulation of differently described components. Tools based on VHDL Analog and Mixed-Signal (AMS) hardware description languages, which can also co-simulate Spice-level components, proved effective in complex designs [79][80][42][81].

In order to keep the consistent of the performance evaluation, some results replicate to Chapter 3 may reported. The main objective of this investigation is to assess the functionality of an UWB imaging system for breast cancer detection. In particular, the critical components of an implementation that uses, for the most part, ad-hoc CMOS integrated circuits are focused. To reach this goal, a simulation and design environment according to the top-down, system-level approach that outlined

above is built. The starting point is an idealized Matlab model like the above chapters, which is the highest-level model to which the refined and less abstract models of the system are compared. For such refined versions, Mentor Graphics' ADMS and its multi-resolution capability is leveraged [42]. ADMS allows to co-simulate blocks described at behavioral-level with blocks described at transistor-level. Such capability allows to test the effect at the system level of circuit-level aspects of the most critical components, which are designed down to the layout level, as well as the effect of noise, nonlinearity, and other impairments. The investigation ends with the understanding through accurate simulations of the effect of the designed components. Therefore, fabricating the system and testing it is out of the scope of this thesis in which the main contributions are illustrated in the following:

- A simulation environment of an UWB imaging system has been implemented and presented again. Simulations use data from real measurements of breast electrical parameters in the microwave frequency range.

- A detailed implementation of an UWB imaging system for breast cancer detection along with its design methodology is outlined.

- A practical implementation has been proved that leverages existing technology is feasible, and the effects of non-ideality of some components are evaluated (UWB antennas and receiver elements like LNA and Track-and-Hold Amplifier) by means of accurate, full-system simulations. In particular, these effects on the reconstructed 2D maps of UWB reflected energies are analyzed and quantified with standard metrics.

The contributions are demonstrated in typical conditions (e.g. breast and tumor size, image resolution). Exploring all possible parameter variations, albeit interesting, is more appropriate when the potential of the technique has to be demonstrated. This is not the goal of this investigation, given that the microwave imaging capability has already been proved with simulations and instrumentation tools.

6.2 UWB imaging system building

To build a simulation and design environment for the entire system, it is partitioned in blocks again, as shown in Figure 6.1: the transmitter, the antenna, the channel model (i.e. the breast and the surrounding environment), the receiver, and the IU that performs image reconstruction.

The simplified scheme in Figure 6.1 reflects the portion of the system that is active any time one pulse is sent, received, and processed. Depending on the position of the antennas around the breast, the channel model is different. In the following, the characteristics of the blocks in Figure 6.1 are succinctly described simply.

116
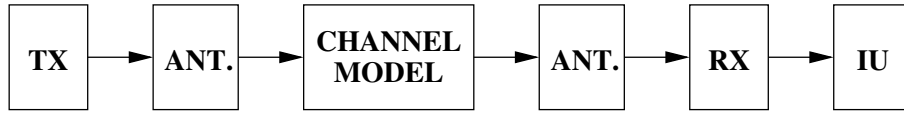
Figure 6.1.   Block scheme of the portion of the system active when one UWB pulse is sent, received and processed. TX is for transmitter, ANT. for antenna, RX for receiver, and IU for Imaging Unit.

6.2.1   Transmitter

The transmitter should offer a certain level of flexibility to generate UWB pulses with different spectral characteristics. An integrated and flexible CMOS UWB transmitter architecture based on the distributed-waveform generator technique has been proposed previously [28][43]. The transmitter synthesizes arbitrary UWB waveforms by delaying, weighting, and finally adding a set of ultra-short base pulses. The transmitter uses a pre-emphasis technique to compensate for bandwidth limitations arising from the antenna or other circuit nonidealities. Post-layout simulations show that generated signals like differential gaussian (DG), Modified Hermite Polynomial (MHP), and Modulated and Modified Hermite Polynomial (MMHP) pulses differ by less than 2% from ideal pulses in terms of RMS error, even when the antenna is taken into account. In this chapter the results obtained with DG pulses are reported, as the DG signal is the most often used in the literature [40][33]. The pulse center frequency is 6 GHz and the pulse 3dB-bandwidth extends from 4.3 to 7.7 GHz.

6.2.2   Antenna

As mentioned previously, in the ideal model that used as a reference, the antenna is ideally modeled as a hertzian dipole, but a custom-designed *slot* antenna is also experimented. Moreover, the so-called monostatic approach is utilized. Since in this approach each antenna transmits the pulse and receives the echo at the same time, an antenna switch cannot be used. Instead, a circulator can be used for this purpose (or a quasi-circulator, given that there is no power transfer from receiver to transmitter), and integrated implementations in the working bandwidth have been reported in the literature [82].

6.2.3   Channel model

The channel model is obtained from an electromagnetic model of the breast, which is assumed surrounded by air. Two numerical breast phantoms are experimented:

an ideal model of a breast uniformly filled with adipose tissue, and a real model with a mix of fat and fibroglandular tissue.

6.2.4 Receiver

In the imaging system, the maximum depth of investigation S_{max} is about 15 cm. The pulse repetition period must be greater than the round-trip time of the UWB pulse, $T_{pulse} \geq 2S_{max}/v$, where v is the wave speed in the breast tissue, which is about $0.95 \cdot 10^{10}\,cm/s$ for the uniform breast model and $0.86 \cdot 10^{10}\,cm/s$ for real breast model. Therefore, the pulse repetition time should be big enough to make sure the echoed pulse from the target will return before next pulse emission. As the investigated scenario is CETS receiver works under time domain radar approach and Eldo is best known for operating in the time domain, the simulation is quite slow especially when its noisetran analysis is activated. In order to save the simulation time, the pulse is repeated every 4 ns instead of 8 ns in Chapter **??**. Furthermore, in order to have a sufficient accuracy in the following imaging process, $T_{equiv} = 4\,ps$ is used, which means that $N = 1000$ equivalent samples in one 4 ns period are acquired. Moreover, parameter M, which determines the real sampling frequency, is limited by the implementation of the following THA/ADC blocks. The choice of $M = 251$ results in $T_{sample} = (251/1000)\,4\,ns = 1.004\,ns$, compatible with the chosen ADC resolution. Each sample is acquired $K = 50$ times and averaged. It can be observed that increasing K up to 50 results in increasingly better results. Beyond 50 the advantage in terms of noise reduction is marginal and there is a negative impact on the overall execution time of the measurement.

The gray box in the block scheme in Figure 6.2 encloses the CETS-based receiver. PLL, TDC and ADC are described behaviorally in VHDL-AMS (hence their different coloring in Figure 6.2). PLL's critical parameter is the jitter of the generated sampling clock, which we consider in its behavioral model. The RMS jitter that a typical PLL can achieve is less than 0.2% of the operation period [83]. In this system 0.2% is about 2 ps as selected in Chapter 4. The TDC is modeled as an ideal 11-bit converter with 2 ps resolution, which can also be achieved in existing technologies [84][85]. At the sampling frequency at stake, the ADC can be implemented with a resolution of 12 bits [86][87]. The different color of two blocks LNA and THA in Figure 6.2 indicates that they are modeled both in VHDL-AMS and as transistor-level components. The digital process block has been modeled in VHDL.

6.2.5 Imaging Unit

As usual, MIST beamforming algorithm is used to reconstruct the imaging. It is implemented in Matlab. For comparison purpose, Figure 6.3 (a) is obtained with an ideal calibration that subtracts, signal by signal, the response without tumor from
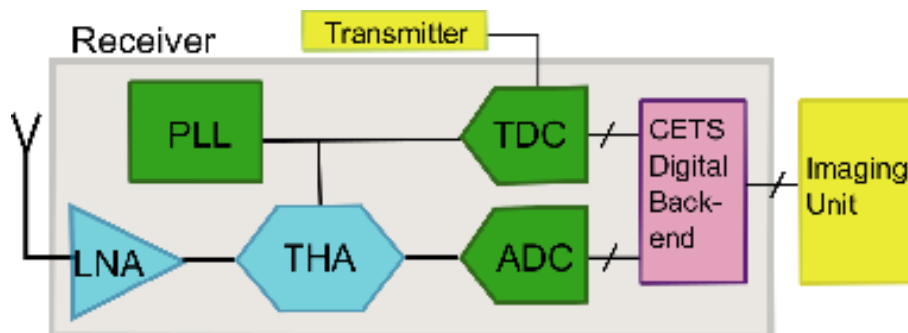
Figure 6.2. Gray box encloses the architecture of the CETS-based receiver. All mixed-signal and analog blocks have a VHDL-AMS description, but LNA and THA also have a Spice transistor-level description. CETS digital back-end block has a VHDL description.

the response with tumor. The ideal calibration is of course not feasible in practice, but the comparison of its results with those of a real calibration helps evaluate the performance of the latter. Figure 6.3 (b) reports the result obtained with MIST after the SKAR calibration introduced in [33]: the tumor is clearly evident and the maximum energy of tumor response is in the same location of the ideal calibration (88 mm, 88 mm). The standard metrics SMR and SCR are also used to evaluate the effectiveness of imaging.

For the cases in Figure 6.3, SMR is 18.5 dB with ideal calibration and 16.7 dB with real calibration. SCR is 8.33 dB with ideal calibration and 7.91 dB with real calibration.

6.3 Methodology

To evaluate the performance of the UWB imaging system as progressed in the refinement of its description, a first ideal version is also implemented and referred as golden case in the remainder of the thesis. Various refined versions are compared to the golden case and this comparison is executed for the two breast models introduced in Chapter 2. In both cases a 4-mm tumor is placed in the middle location within the breast, corresponding to position (88 mm,88 mm) in the 2D map of dielectric properties of the breast.

Firstly, the comparison of the golden case with ideal breast with seven other refined cases are discussed, case-1 to case-7. Then the breast model is changed and the golden case with real breast is compared with a final case, which is called as case-8. Table 6.1 summarizes the various cases and their main features.

In the two golden cases, the entire system is modeled in Matlab, including FDTD

119
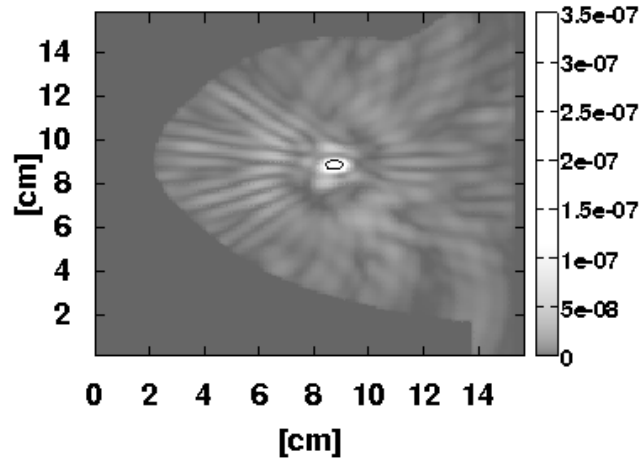
(a)
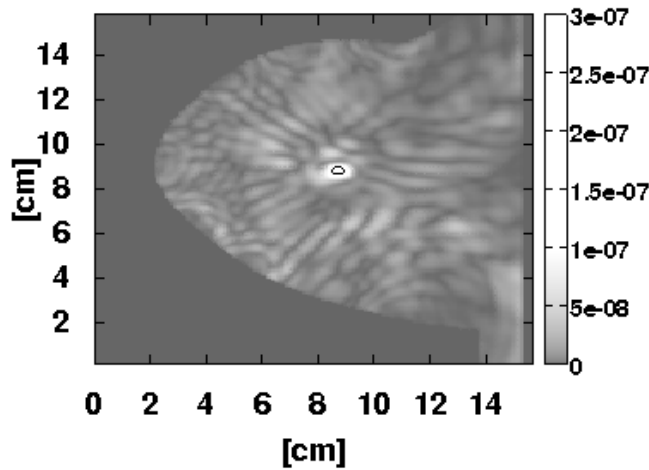
(b)

Figure 6.3.   Images reconstructed using MIST. (a) Skin artifact removed by ideal calibration and (b) by real calibration. The tumor is enclosed by a contour level set to a value slightly lower than the maximum energy found in the map.

channel model and back-end processing. To determine a performance upper bound, noise sources and other non-idealities are ignored. For instance, the TDC and the ADC in the golden cases have infinite resolution – 64-bits double precision numbers is used – and have no saturation or input range limitations. The same holds for LNA, THA and antennas, assumed as ideal components without bandwidth limitations nor limits in dynamics determined by a finite supply voltage. Data fed to the image reconstruction algorithm have highest resolution and accuracy. The MIST image in

Case	Description
golden with ideal breast	Matlab description of the imaging system, case of homogeneous breast, tumor in middle position.
case-1	Receiver blocks in behavioral VHDL-AMS, limited resolution and input range as well as saturation effects of ADC (12 bits) and TDC (11 bits).
case-2	Like case-1, with AMS modeling of noise (thermal, clock jitter), bandwidth limitations and non-linearity.
case-3	Like case-1, with custom-designed antenna.
case-4	Like case-1, with transistor-level LNA description.
case-5	Like case-1 with transistor-level THA description.
case-6	Like case-1, with both transistor-level LNA and THA.
case-7	Like case-2, with custom antenna, LNA, and THA.
golden with real breast	Like golden case with ideal breast, but with a heterogeneous breast model taken from [21].
case-8	Like case-7, but with heterogeneous breast model.

Table 6.1.   Description of the simulation cases.

Figure 6.3 (b), which commented on above, represents the energy map obtained in the golden case with ideal breast.

The first refined version, case-1, has been obtained by removing from Matlab the description of the receiver, and by building a VHDL-AMS model of it to be run within ADMS. The rest of the system keeps being modeled in Matlab, and file exchange acts as interface between Matlab and ADMS. In this version, all the receiver blocks in Figure 6.2 are individually and behaviorally modeled. Every block has its own VHDL-AMS entity and architecture, and together they form a structural netlist. The structural description is a necessary step toward the refinement of the description of the other cases in Table 6.1. Noise source and bandwidth limitations are not considered yet, but a limited resolution and input range of ADC and TDC are introduced. Saturation effects determined by the supply voltage are also modeled.

Simulations in case-2 to case-8 are evolutions of case-1. The effect of noise, finite bandwidth and non-linearity are firstly considered. Then the substitute-and-play approach described in [42] is applied to refine the description of the blocks. First the hertzian dipole is replaced with a custom-designed slot antenna. The evaluations are

continued by replacing the VHDL-AMS models of LNA and THA with their Spice-level description, one by one or combined. Finally all the non-idealities are put together. This approach permits to keep the overall system architecture unchanged across the multiple cases, to reuse the same testbench, and so to easily compare the results.

Details about implementation of the blocks and modeling issues are reported in the next section, together with the results of the simulations of the various cases.

6.4 Simulation results

The refinement of the description shows how the various non-ideal effects determine a performance degradation with respect to the golden cases. The impact the reduction of abstraction has on performance qualitatively is determined, by visually comparing the images obtained in the various cases to the golden images, and quantitatively, by comparing SMR and SCR values to the corresponding golden values.

Case-1: In case-1 all the blocks are still described behaviorally. The modeled non-idealities are finite resolution of ADC and TDC, input range limits of ADC and saturation effects. Assuming that the voltage cannot exceed the range from $0\,\mathrm{V}$ to $1.2\,\mathrm{V}$ in any point in the chain that goes from LNA to ADC. This range comes from power supply limits of the technology that will be use in the next steps. The LNA voltage gain is set to 5 ($14\,\mathrm{dB}$) and the THA gain to 1 ($0\,\mathrm{dB}$).

Figure 6.4 reports signals from case-1 simulations and shows the transmitted pulse, the pulse at the input of the receiver, and the pulse at the output of the block that models the LNA. The zoomed part is where the tumor information is.

The dynamic range of the signal is on the order of $70\,\mathrm{dB}$, which has two consequences. First, the high gain needed to sense the small tumor information determines a substantial distortion of the first part of the signal, which contains the large echo of the skin back-scatter. The effect can be seen in the saturation of the LNA output in Figure 6.4. Since this distortion does not modify the part of the signal that conveys the tumor information, it has little or no effect on performance.

The second consequence is that at least a 12-bit ADC is required, as referring to the value defined in Chapter 4. The flexibility of VHDL-AMS allows to explore the design space. Simulation experiments with a 12-bit and a 16-bit ADC model have been executed. SCR and SMR metrics have been compared, and visually inspected the energy maps. Since the difference is around $0.5\,\mathrm{dB}$ in terms of SCR and SMR values, and the two maps are almost indistinguishable to the naked eye, a 12-bit ADC is selected for this receiver.

SCR, SMR, and position of the tumor for case-1 are reported in Table 6.2, which also reports all the values found in the various cases. Likewise, Figure 6.8 reports
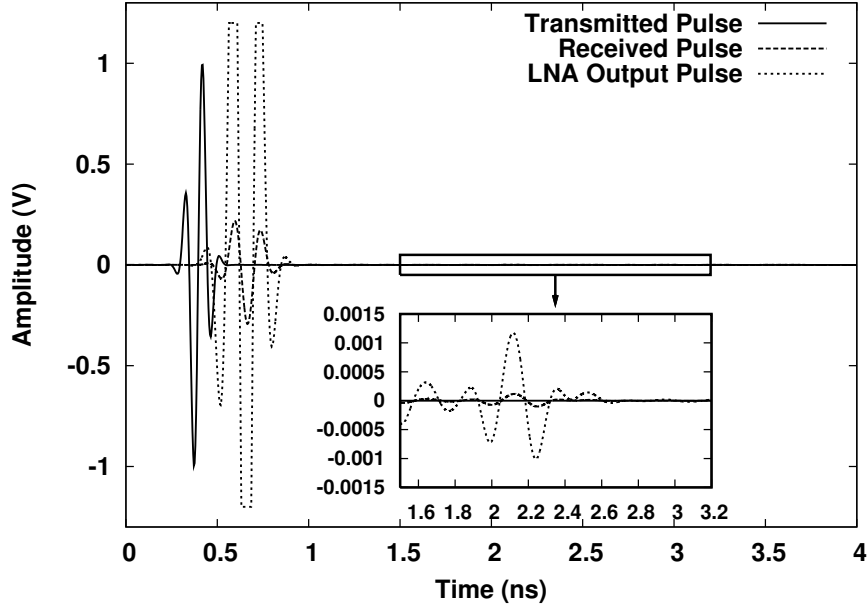
Figure 6.4. Example of signals from case-1 simulation. The inset expands the time region associated with the tumor information.

all the energy maps. By comparing case-1 to the golden case with ideal breast, the impacts of ADC, TDC, and saturation are quantifies as about 1.0 dB in terms of SCR and SMR. The maximum of the energy response is within the 4-mm tumor region, albeit displaced by 1 mm compared to the golden case.

Case-2: In case-2 bandwidth limitations, thermal noise, clock jitter and non-linearity are added, which are modeled in VHDL-AMS and parametrized to permit sensitivity analyses. The results obtained with the following parameters are reported, which are reasonable and consistent with the state of the art: 3-dB bandwidth between 0.5 GHz and 10 GHz; LNA gain, noise figure, and third-order intercept points 14 dB, 5 dB, and -3 dBm, respectively; 150 fF for the KT/C noise of the THA; 2 ps RMS jitter noise; standard value of input thermal noise at 300 K, modeled as additive gaussian noise.

As stated above, the CETS acquisition is repeated $K = 50$ times and the samples are averaged. Figure 6.5 shows the 50 sampled signals overlapped and the average signal after reordering. Zoomed insets in Figure 6.5 show that averaging reduces the effect of noise sources, particularly in the region around the small tumor information. The TDC values obtained in K experiments are therefore averaged to minimize the effect of PLL's jitter.
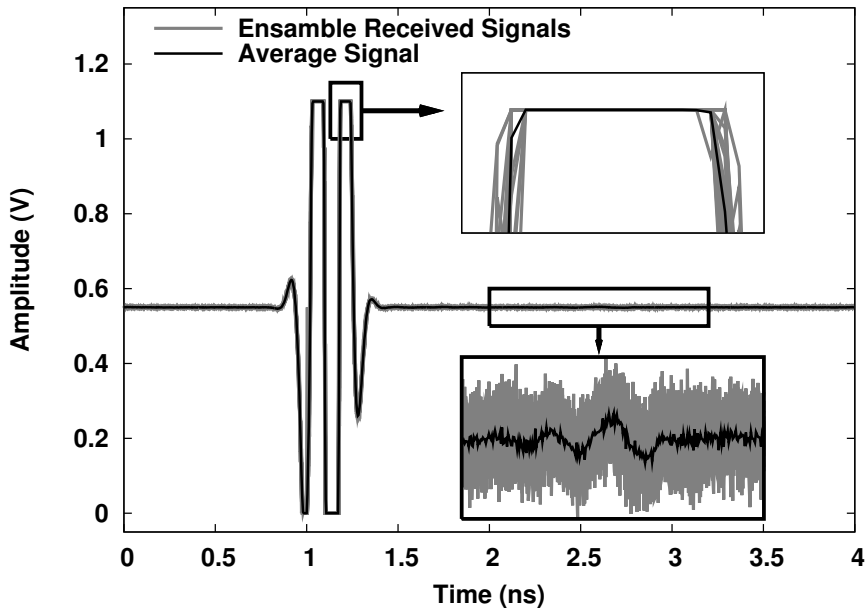
Figure 6.5. Ensemble received and reordered signals (K=50) and average signal in case-2, with thermal noise, jitter and quantization. Insets show effectiveness of average in mitigating these effects, especially around the time region where the small tumor information is present.

Results in Table 6.2 and Figure 6.8 show that the various impairments have small effect. The tumor is clearly visible, but the clutter is more evident. SMR and SCR are about 1 and 2.7 dB smaller than in golden case.

Case-3: In case-1 and case-2 the antenna is modeled as an ideal hertzian dipole, which is replaced by a real microstrip slot antenna that was designed in Chapter 5 in this case.

To analyze separately the effect of the antenna, in case-3 noise sources and all other linear and non-linear distortions of case-2 are removed. The antenna is modeled as a 2-port network, with S-parameters [50] as a function of frequency, and replaced in VHDL-AMS the ideal model with the refined one. The relationship between antenna input pulse and output pulse is represented by the insertion loss S_{21}, which is calculated by the following equation [50].

$$|S_{21}| = \sqrt{(G(1 - |S_{22}|^2))} \tag{6.1}$$

where G is the antenna power gain, S_{22} is the same with S_{11} of the antenna, as assuming antennas have the same characteristics in transmitting and receiving mode.

Results in Figure 6.8 and Table 6.2 show the the effect of the antenna is very small, if comparing SMR, SCR and the map to case-1 in which an ideal antenna is used.

In addition, as mentioned in Section 6.2.2, the monostatic approach requires an additional circulator or quasi-circulator with sufficient isolation between transmitter and receiver in the whole bandwidth. The coupling between transmitter and receiver of a non-ideal circulator is modeled. Results show that SMR has 0.3 dB reduction and SCR has 0.03 dB reduction when the isolation is set to -18 dB. Therefore the circulator that would be used must feature an isolation of -18 dB or better, which can be easily achieved [82][88].

Case-4: Thanks to the flexibility offered by Mentor Graphics' ADMS, the VHDL-AMS behavioral model of the LNA can be replaced by a transistor-level Spice netlist which will be exported from Cadence software. The entity declaration does not change, nor does the structural description at the upper hierarchy level

The antenna in case-3 is single-ended, so a balance-unbalance (balun) transformer is required when connecting the antenna to the differential LNA. The balun should cover the whole bandwidth and have small insertion and return losses. Several papers show an insertion loss smaller than 2 dB in a 7.5-GHz bandwidth [89] [90]. This typical value is used as a model parameter of the balun when we evaluate the system performance.

As shown in Section 5.2, the impedance mismatch (S11 and S22) of the designed LNA is less than -10 dB from 500 MHz to 12 GHz, and the gain is between 14.5 and 17.2 dB. The noise figure ranges from 3.1 to 4 dB between 2 and 12 GHz. However, the simulated nonlinearity parameter IIP3 is -16 dBm at 5 GHz. The nonlinearity will mainly influence the skin backscattered part of the received pulses, because the tumor information part is weak and so not influenced by nonlinearity. Since the distorted skin-reflected part will be erased through a careful calibration, as shown in Figure 3.10, there will be no effect of this distortion.

Full-system simulations are run as the other cases, both including and not including the LNA post-layout parasitic parameters. Results in Table 6.2 refer to the case in which parasitics are included. The evaluated performance without parasitic parameters shows a reduction of about 1.1 dB and 2.6 dB of SMR and SCR, respectively, compared to the golden case. When parasitics are taken into account, SMR and SCR in Table 6.2 are 2.5 dB and 3.6 dB less than the golden case, respectively. The map in Figure 6.8, accordingly, exhibits a more energetic clutter than in the case without parasitics (not reported).

Case-5: Similarly to case-4, the THA behavioral model is replaced by the transistor-level netlist of a circuit designed in the same 130 nm CMOS technology.

Figure 6.6 reports waveforms obtained from full-system simulations and shows

125
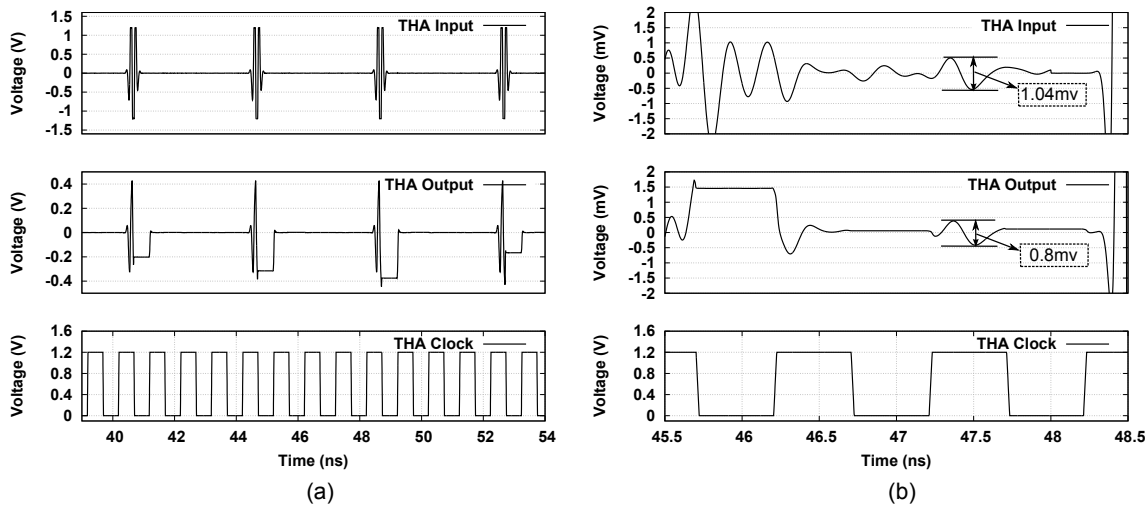
Figure 6.6.   ADMS simulation result showing the behavior of THA when tracking and holding one of the received signals.

that the received signal is correctly tracked and held by the THA. It also shows that the sampling clock correctly drifts in time with respect to the pulse repetition clock, hence permitting the acquisition of different samples as we exemplified in Figure 4.4. Figure 6.6 (b) is a zoom of Figure 6.6 (a) and shows the part of the signal that contains the weak tumor information, also correctly sampled. The period of the sampling clock is 1.004 ns, according to the specifications outlined in Section 6.2.4, with 32 ps rise time and 28 ps fall time, as determined by the clock buffer. Figure 6.6 (b) shows that the gain of the THA in track phase is about 0.8/1.04=0.769, which corresponds to -2.28 dB. More detailed AC simulations show that the gain is -2.5 dB over a 12-GHz 3-dB input bandwidth (refer to Section 5.3). The output/input ratio that one can measure in Figure 6.6 (a) is less than -2.5 dB due to the gain compression determined by nonlinearity. As stated above, however, the skin reflected part of the pulse that causes nonlinearity effects will be eliminated through calibration.

The imaging performance has been assessed using the THA with post-layout parasitic parameters as well as THA without parasitics, and the similar SMR is obtained and only 0.6-dB SCR reduction when parasitics are included. SMR and SCR in Table 6.2 include parasitics and are close to the golden case values. Accordingly, the map in Figure 6.8 has a clear energy peak. These results confirm that the CMOS THA block works nearly as well as its ideal version.

Case-6: In case-6 both the LNA and THA VHDL-AMS models are replaced with Spice netlists annotated with layout parasitics. As expected, the clutter in Figure 6.8 is more evident. Likewise, SMR and SCR are worse than values obtained

in case-4 and case-5, in which the two circuits were tested separately (see Table 6.2). Still, the tumor is correctly identified.

Case-7: This is the worst among the cases of ideal breast, because the realistic antenna, LNA and THA are all put together, and on top of that all noise and jitter sources are enabled. It is pleased to observe that all the components combined perform, at system-level, as well as when each is separately considered, even under worst noise and jitter. SCR, SMR, and energy map are similar to previously analyzed cases.

In this case, the effect of reducing the tumor size below 4 mm are also evaluated. The graphs in Figure 6.7 show the simulated system performance metrics as a function of the tumor size. It is possible to see that the system performance increases with the increase of tumor size. A tumor having a diameter as small as 2 mm yields 10.3 dB SMR and 1.5 dB SCR, which are values that make the tumor hardly detectable.
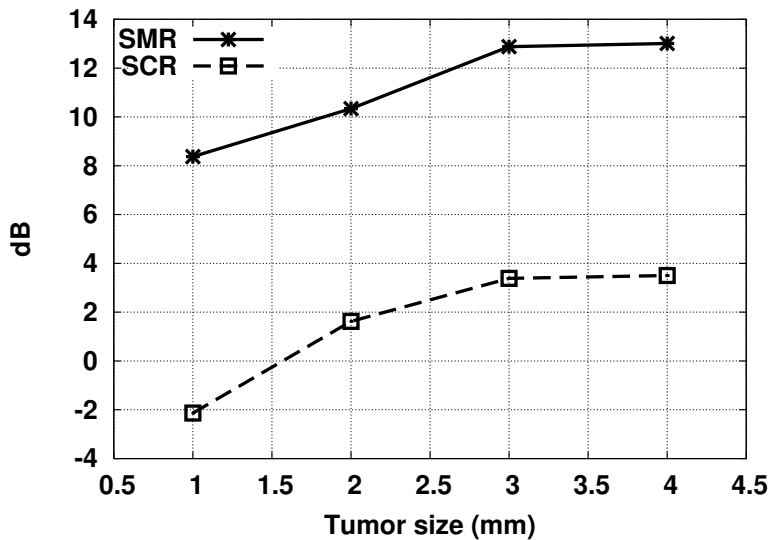
Figure 6.7.   System metrics (SMR, SCR) as a function of tumor's size.

Golden case with real breast model: Results obtained in the golden case with a real breast model are significantly different than those obtained in the golden case with an ideal breast model. Tumor detection is more challenging, because different tissues have different propagation velocity, which makes the alignment of received signals a more complex task. A greater signal attenuation decreases the dynamic response of the tumor mass, which calls for a very sensitive receiver. On

127

Case	SMR (dB)	SCR (dB)	Tumor position (mm,mm)
golden ideal breast	16.76	7.91	88,88
case1	16.00	6.96	88,87
case2	15.81	5.19	88,87
case3	15.80	7.09	88,87
case4	14.26	4.37	90,88
case5	16.03	5.43	89,87
case6	13.50	3.22	91,88
case7	13.01	3.50	89,88
golden real breast	13.11	2.44	82,84
case8	13.06	1.98	86,82

Table 6.2. Signal-to-Mean Ratio (SMR), Signal-to-Clutter Ratio (SCR), and tumor estimated position for the cases outlined in Table 6.1.

top of that, each dielectric discontinuity generates a reflection that makes the clutter response larger.

The map in Figure 6.8 exhibits a more evident clutter and more than one point with a very high reflected energy. Consequently, SCR in Table 6.2 is small (2.4 dB).

SMR is still high, about 13 dB, which means that there is still a significantly higher energy value in the tumor region than elsewhere. The tumor can still be easily found, even though the estimated position is offset by 6 mm and 4 mm in the two directions.

Since this is a golden case, the reduction of imaging performance with respect to previous cases is determined by the more complex breast model and the MIST limitations. Circuit-level effects are not yet considered.

Case-8: For sake of brevity, Results for all the intermediate cases as we did for the uniform breast model are not reported. Instead, results for a case akin to case-7 are reported, which is the worst case with ideal breast, with all sources of non-idealities active, and with antenna, LNA, and THA circuits. Numerical results in Table 6.2 are very close to the corresponding golden case with real breast, which confirms that the effect of circuits and non-idealities is small. The reconstructed map in Figure 6.8 shows that the tumor is still easily identified.

Given that the system performance metrics in this case of heterogeneous breast are slightly worse than the performance in the homogeneous case, and based on the results of Figure 6.7, is is possible to conclude that 4 mm is the limit size of a clearly detectable tumor.
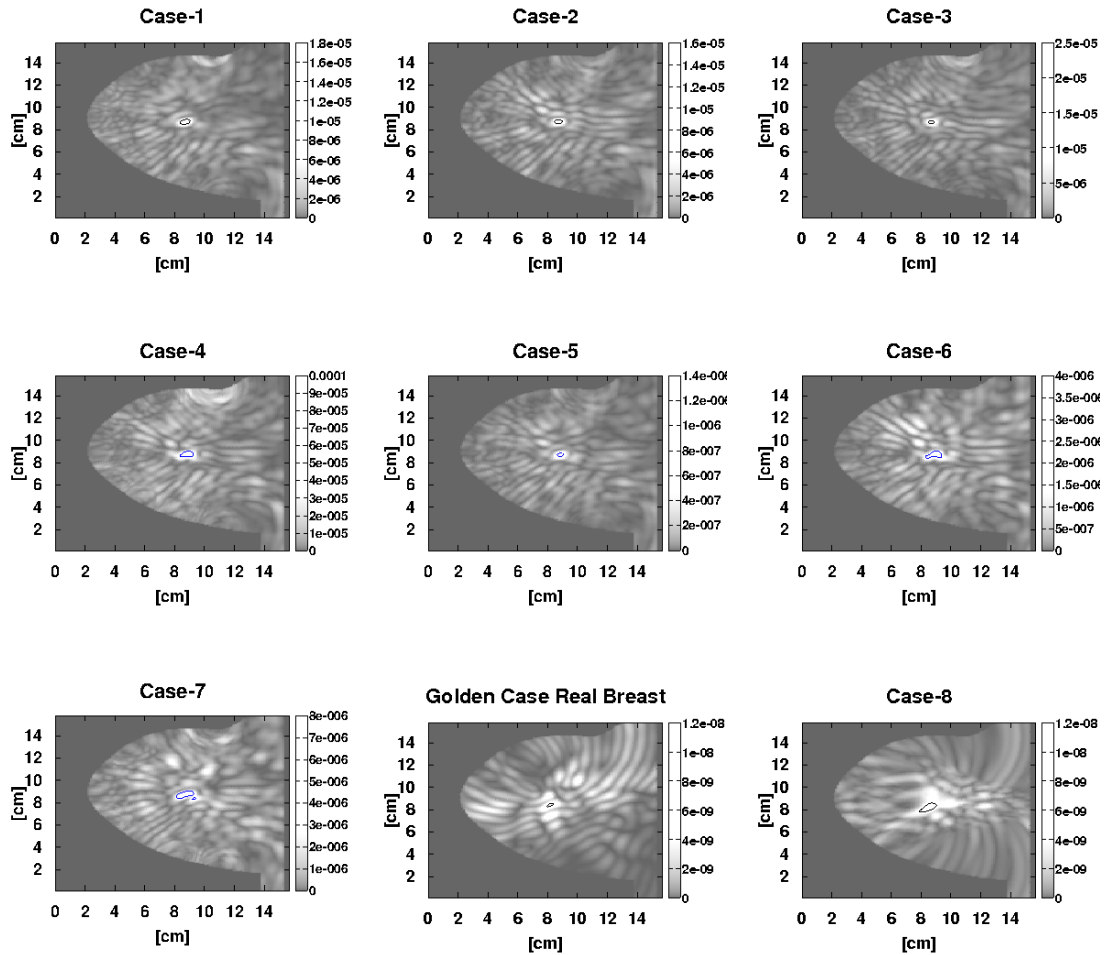
Figure 6.8. Energy maps resulting from the system-level simulations of the various cases outlined in Table 6.1 (energy unit is arbitrary). The tumor can be easily identified in each of the reported maps, because it is enclosed by a contour level that we set to a value slightly lower than the maximum energy.

Chapter 7

Conclusion

The work of this thesis aimed to develop an UWB imaging system for breast cancer detection. The principle this diagnostic method relies on is the UWB microwave radar imaging technique already used in ground-penetrating radar applications. It is suited to breast cancer detection, because it is non-ionizing and so it can be repeated several times without incurring the problem of radiation typical of standard methods like mammography, at the cost of a lower accuracy. Another advantage is that it is potentially a lower-cost alternative to standard methods like the mentioned mammography or other methods like magnetic resonance. Experiments with RF instrumentation proved this method capable of detecting small tumors, but adoption in screening campaigns requires the replacement of RF tools with ad-hoc circuits and systems: this is where the research conducted in my thesis fits in. In order to do this, the overall simulation environment must be developed, which includes a breast electromagnetic model obtained with an FDTD technique, antennas which are put around the breast model and modeled as ideal dipoles, digital processing which is used to reconstruct the breast image by a specific microwave imaging algorithm and UWB transmitters and receivers which connect to the antenna by means of circulators. Initially all the system elements are described behaviorally and as ideal components. The results of this system analysis reveal the functionality of the imaging system, in the case of different breast model, different tumor size and different tumor position. In addition, to save simulation time, the transfer functions of the breast electromagnetic model were developed, and were verified to be able to replace the time-domain model of real breasts reasonably.

Subsequently, the RF front-end was developed, especially the ad-hoc designed receiver. The reason of this choice was that in this medical imaging application the receiver was more important and difficult to implement than other parts, since its requirements were quite strict, given that it had to cover the specific ultra-wide bandwidth (from 3.1 to 10.6 GHz), while achieving very large dynamic ranges. There were two candidates for the implementation of integrated receiver of the RF frontend:

one was the direct conversion (DC) receiver, the other was the coherent equivalent time sampling (CETS) receiver. Primarily, the receivers were behaviorally modeled and applied in the imaging system. Key impairments relating to the circuit design were involved. The receivers performance was evaluated in terms of both qualitative breast images and of specific quantitative metrics like SMR and SCR. In particular, the effects of transmitted signal power, analog-to-digital converter quantization, noise, phase mismatches and non-linearity were evaluated. Considering the overall behavior in terms of image quality, performance measured by SMR and SCR parameters, and data acquisition time. The CETS receiver was proved to outperform the DC one, and was thus more suitable for this microwave breast cancer detection application.

The aim of this work was also the hardware implementation. Two key elements of the proposed CETS receiver, Low Noise Amplifier (LNA), and the Track-and-Hold Amplifier (THA), have been designed and simulated in a CMOS 130 nm technology using Cadence. The post-simulation results of the proposed LNA showed good conversion gain and noise performance within the 3 dB bandwidth 2-12 GHz. The designed THA achieved high linearity from 0 to 10 GHz and high sampling frequency up to 4 GHz, which were suitable for this specific application. Moreover, an UWB slot antenna was designed with HFSS software, it presented a less than -10 dB return loss behavior from 2 GHz to 11 GHz.

Finally, in order to evaluate the system performance with these real designed circuits, a different system environment was built, which was based on analog and mixed-signal hardware description languages VHDL-AMS and on powerful tools like Mentor Graphics' ADMS. The system environment permitted to explore the refinement of this complex system in various design stages. To keep the consistency of the system evaluation, the design flow started from a highly abstract description of the system, and progressively refined it by replacing some of the most critical blocks' behavioral description with a lower-level description. The impacts of non-idealities like quantization, noise, jitter and input range limits on the performance of the imaging system were evaluated. The effects at system-level of three critical blocks were eventually determined, by replacing their behavioral description with real transfer functions (antennas) or transistor level netlists obtained from previously designed in a 130 nm CMOS technology (LNA and THA). The simulation and comparison results, which were obtained under both homogeneous breast model and heterogeneous breast model, reveal that despite the design challenges that an UWB imaging system poses, the system is capable of detecting a small 4 mm tumor, as proved with accurate simulations on numerical breast phantoms.

Bibliography

[1] Ries LAG, Young JL, Keel GE, Eisner MP, Lin YD, and Horner M-J (editors). SEER Survival Monograph: Cancer Survival Among Adults: U.S. SEER Program, 1988-2001, Patient and Tumor Characteristics. *National Cancer Institute, SEER Program, NIH Pub. No. 07-6215, Bethesda, MD.*

[2] Guth U, Huang DJ, Huber M, and et al. Schotzau A. Tumor size and detection in breast cancer: Self-examination and clinical breast examination are at their limit. *Cancer Detect Prev*, (32):224–228.

[3] Kerlikowske K, Hubbard RA, Miglioretti DL, Geller BM, Yankaskas BC, Lehman CD, Taplin SH, and Sickles EA. Comparative effectiveness of digital versus film-screen mammography in community practice in the United States: a cohort study. *Ann Intern Med*, 8(155):493–502, 2011.

[4] Smith AP, Hall PA, and Marcello DM. Emerging technologies in breast cancer detection. *Radiology Management*, 4(26):16–24, 2004.

[5] E.C. Fear, X. Li, S.C. Hagness, and M.A. Stuchly. Confocal microwave imaging for breast cancer detection: Localization of tumors in three dimensions. *IEEE Transactions on Biomedical Engineering*, 49(8):812–822, 2002.

[6] Natalia K. Nikolova. Microwave imaging for breast cancer. *IEEE Microw. Mag.*, 12(7):78–94, 2011.

[7] R. Tipa and O. Baltag. Microwave Thermography for Cancer Detection. *Rom. Journ. Phys.*, 51:371–377, 2006.

[8] A. Mamouni Y. Leroy G. Giaux J. Delannoy B. Bocquet, J. C. Van De Velde and D. Delvalee. Microwave radiometric imaging at 3 GHz for the exploration of breast tumors. *IEEE Trans. Microw. Theory Tech.*, 38(6):791–793, 1990.

[9] Meaney P M et al Fear C, Hagness S C. Enhancing breast Tumor detection with near field imaging. *IEEE Microwave Magazine*, 3(1):48–56, 2002.

[10] Vitaliy Zhurbenko. Challenges in the Design of Microwave Imaging Systems for Breast Cancer Detection. *Advances in Electrical and Computer Engineering*, 11(1):91–96, 2011.

[11] J.D. Shea, S.C. Hagness, and B. D. Van Veen. Hardware acceleration of fdtd computations for 3-d microwave breast tomography. In *Antennas and Propagation Society International Symposium, 2009. APSURSI '09. IEEE*, pages 1–4.

132

IEEE, 2009.

[12] S.K. Padhi, A. Fhager, M. Persson, and J. Howard. Experimental performances of antennas for a proposed microwave tomography system using the time-domain approach. In *Antennas and Propagation Society International Symposium, 2009. APSURSI '09. IEEE*, pages 1–4. IEEE, 2009.

[13] D. Morris. Sorting through em simulators. In *Microwaves & RF*, 2012.

[14] A. Taflove and S. C. Hagness. *Computational Electrodynamics: The Finite-Difference Time-Domain Technique*. 3rd ed. Boston, MA: Artech, 2005.

[15] Carl H. Durney Douglas A. Christensen Dale N. Buecheler, Daniel H. Roper. Modeling sources in the fdtd formulation and their use in quantifying source and boundary condition errors. *IEEE Transactions on Microwave Theory and Techniques*, 43(4):810–814, 1995.

[16] M. Bonazza. Analisi e sviluppo di un sistema di ricetrasmissione basato su uwb per l'identificazione del carcinoma mammario. Master's thesis, Politecnico di torino, 2011.

[17] W.Yu. *Electromagnetic Simulation Techniques Based on the FDTD Method*. John Wiley & Sons, 2009.

[18] J. Berenger. A perfectly matched layer for the absorption of electromagnetic waves. *Journal of Computational Physics*, 2(114):185–200, 1994.

[19] J. A. Roden and S. D. Gedney. Convolutional pml (cpml): An efficient fdtd implementation of the cfs-pml for arbitrary media. *Microwave Optical Tech. Let.*, 27:334–339, 2000.

[20] E. Zastrow, S. K. Davis, M. Lazebnik, F. Kelcz, B. D. Van Veen, and S. C. Hagness. Database of 3d grid-based numerical breast phantoms for use in computational electromagnetics simulations.

[21] Uwcem numerical breast phantom repository, 2012.

[22] D. Popovic C. B. Watkins M. J. Lindstrom J. Harter S. Sewall A. Magliocco J. H. Booske M. Okoniewski M. Lazebnik, L. McCartney and S. C. Hagness. A large-scale study of the ultrawideband microwave dielectric properties of normal breast tissue obtained from reduction surgeries. *Physics in Medicine and Biology*, 52:2637–2656, 2007.

[23] L. McCartney C. B. Watkins M. J. Lindstrom J. Harter S. Sewall T. Ogilvie A. Magliocco T. M. Breslin W. Temple D. Mew J. H. Booske M. Okoniewski M. Lazebnik, D. Popovic and S. C. Hagness. A large-scale study of the ultrawideband microwave dielectric properties of normal, benign, and malignant breast tissues obtained from cancer surgeries. *Physics in Medicine and Biology*, 52:6093–6115, 2007.

[24] R. W. Lau S. Gabriel and C. Gabriel. The dielectric properties of biological tissues: Iii. parametric models for the dielectric spectrum of tissues. *Physics in Medicine and Biology*, 41:2271–2293, 1996.

[25] D.W. Winters, E.J. Bond, B.D. Van Veen, and S.C. Hagness. Estimation of the frequency-dependent average dielectric properties of breast tissue using a time-domain inverse scattering technique. *IEEE Trans. Antennas Propag.*, 54(11):3517–3528, 2006.

[26] Maciej Klemm, Ian Craddock, Jack Leendertz, Alan Preece, and Ralph Benjamin. Radar-based breast cancer detection using a hemispherical antenna array-experimental results. *IEEE Trans. Antennas Propag.*, 57(6):1692–1704, 2009.

[27] S. Ingarra. Progetto di un sistema di trasmissione uwb per il rilevamento del carcinoma mammario. Master's thesis, Politecnico di torino, 2010.

[28] M. Cutrupi, M. Crepaldi, M. R. Casu, and M. Graziano. A flexible uwb transmitter for breast cancer detection imaging systems. In *Design, Automation & Test in Europe Conference &Exhibition (DATE)*, pages 1076–1081, Dresden, 2010.

[29] M. O'Halloran, E. Jones, and M. Glavin. Quasi-Multistatic MIST Beamforming for the Early Detection of Breast Cancer. *IEEE Trans. Biomed. Eng.*, 57(4):830–840, 2010.

[30] Y.F. Chen, E. Gunawan, K.S. Low, S.C. Wang, Y.M. Kim, and C.B. Soh. Pulse design for time reversal method as applied to ultrawideband microwave breast cancer detection: A two-dimensional analysis. 55(1):194–204, 2007.

[31] S.C. Hagness S.K. Davis, H. Tandradinata and B.D. Van Veen. Ultrawideband microwave breast cancer detection: A detection-theoretic approach using the generalized likelihood ratio test. *IEEE Trans. Biomed. Eng.*, 52(7):1237–1250, 2005.

[32] Hooi Been Lim, Nguyen Thi Tuyet Nhung, Er-Ping Li, and Nguyen Duc Thang. Confocal Microwave Imaging for Breast Cancer Detection: Delay-Multiply-and-Sum Image Reconstruction Algorithm. *IEEE Trans. Biomed. Eng.*, 55(6):1697–1704, 2008.

[33] E.J. Bond, Xu Li, S.C. Hagness, and B.D. Van Veen. Microwave imaging via space-time beamforming for early detection of breast cancer. *IEEE Transactions on Antennas Propagation*, 51(8):1690–1705, 2003.

[34] X.Li, E.J. Bond, Barry D. Van Veen, and Susan C. Hagness. An overview of ultra-wideband microwave imaging via space-time beamforming for early-stage breast cancer detection. *Antennas and propagation magazine*, 47(1):19–34, 2005.

[35] P. Rosingana. Design of a uwb imaging system for breast cancer detection. Master's thesis, Politecnico di torino, 2011.

[36] Shakti K. Davis, Essex J. Bond, Xu Li, Susan C. Hagness, and Barry D. Van Veen. Microwave imaging via space-time beamforming for early detection of breast cancer: Beamforming design in the frequency domain. *Journal of Electromagnetics Waves and Applications*, 17:357–381, 2003.

[37] Shakti K. Davis, Xu Li, Essex J. Bond, Susan C. Hagness, and Barry D. Van Veen. Frequency-Domain Penalized Least-Squares Beamformer Design for Early Detection of Breast Cancer via Microwave Imaging. In *Sensor Array and Multichannel Signal processing Workshop Proceedings*, 2002.

[38] S. Haruyama M. Ghavami, L. B. Michael and R. Kohno. A novel uwb pulse shape modulation system. *IEEE Transactions on Microwave Theory and Techniques*, 23:105–120, 2002.

[39] R.Kohno M.Ghavami, L.B. Micheal. *Ultra Wideband, signals and systems in communication engineering*. John Wiley & Sons, 2004.

[40] X. Li and S.C. Hagness. A confocal microwave imaging algorithm for breast cancer detection. *IEEE Microwave and Wireless Components Letters*,11(3):130–132, 2001.

[41] James Michaelson, Sameer Satija, Richard Moore, Griffin Weber, Elkan Halpern, Andrew Garland, Daniel B Kopans, and Kevin Hughes. Estimates of the sizes at which breast cancers become detectable on mammographic and clinical grounds. *Journal of Women's Imaging*, 5(1):3–10, 2003.

[42] M. R. Casu, M. Crepaldi, and M. Graziano. A vhdl-ams simulation environment for an uwb impulse radio transceiver. *IEEE Trans. Circuits Syst. II*, 55(5):1368–1381, 2008.

[43] M. R. Casu, M. Graziano, and M. Zamboni. A fully differential digital cmos uwb pulse generator. *Circuits, Systems, and Signal Processing*, 28:649–664, 2009.

[44] Donald R. Wehner. *High-Resolution Radar*. Artech House Radar, 1994.

[45] Behzad Razavi. *RF Microelectronics*. Prentice Hall, 1997.

[46] Matteo Bassi, Andrea Bevilacqua, Andrea Gerosa, and Andrea Neviani. Integrated sfcw transceivers for uwb breast cancer imaging: Architectures and circuit constraints. *IEEE Trans. Circuits Syst. I*, 59(6):1228–1241, 2012.

[47] Matteo Bassi, Michele Caruso, Andrea Bevilacqua, and Andrea Neviani. A 1.75–15 ghz stepped frequency receiver for breast cancer imaging in 65 nm cmos. In *2012 Proceedings of ESSCIRC*, pages 353–356. IEEE, 2012.

[48] David D. Reynolds and Roman A. Slizynski. Coherent sampling digitizer system, January 1998.

[49] X. Guo, M.R. Casu, M. Graziano, and M. Zamboni. Breast cancer detection based on an uwb imaging system: Receiver design and simulations. In *Proc. IEEE Int. Conf. on IC Design and Technology(ICICDT)*, pages 167–170, Pavia, Italy, 2013.

[50] T. Prakoso, R. Ngah, and T.A. Rahman. Representation of antenna in two-port network s-parameter. In *Proc. 2008 IEEE International RF and Microwave Conference*, pages 293–297, Kuala Lumpur, 2008. IEEE.

[51] Modeling rf system, 2005.

[52] J. He, J.S. Yang, Y. Kim, and Kim. A.S. System-level time-domain behavioral modeling for a mobile wimax transceiver. In *Behavioral Modeling and Simulation Workshop, Proceedings of the 2006 IEEE International*, pages 138–143, San Jose, CA, 2006. IEEE.

[53] M. Kimura, A. Minegishi, K. Kobayashi, and H. Kobayashi. A new coherent sampling system with a triggered time interpolation. *Journal of IEICE Trans. Fundamentals*, (3):713–719, 2001.

[54] M. Klemm, Ian. Craddock, J. Leendertz, A. Preece, and R. Benjamin. Experimental and clinical results of breast cancer detection using uwb microwave radar. In *AP-S 2008. IEEE*, pages 1–4, San Diego, CA, 2008.

[55] X. Li, S.C. Hagness, M.K. Choi, and D.W Van Der Weide. Numerical and experimental investigation of an ultrawideband ridged pyramidal horn antenna with curved launching plane for pulse radiation. *Antennas and Wireless Propagation Letters, IEEE*, 2(1):259–262, 2005.

[56] S.C. Shin, J.Y. Huang, K.Y. Lin, and H. Wang. A 1.5-9.6ghz monolithic active quasi-circulator in 0.18 mm cmos technology. *IEEE Microw. Wirel. Compon. Lett.*, 18(12):797–799, 2008.

[57] Chun-Ying Chen, Jiangfeng Wu, Juo-Jung Hung, and Tianwei Li. A 12-bit 3 gs/s pipeline adc with $0.4mm^2$ and 500 mw in 40 nm digital cmos. *IEEE J. Solid-State Circuits*, 47(4):1013–1021, 2012.

[58] Eric Siragusa and Ian Galton. A digitally enhanced 1.8-v 15-bit 40-msample/s cmos pipelined adc. *IEEE J. Solid-State Circuits*, 39(12):2126–2138, 2004.

[59] F. Colonna, M. Graziano, M.R. Casu, X. Guo, and M. Zamboni. Hardware acceleration of beamforming in a uwb imaging unit for breast cancer detection. *VLSI Design*, 2013(no. Article ID 861691):11 pages, 2013.

[60] Jaeha Kim. Adaptive-bandwidth phase-locked loop with continuous background frequency calibration. *IEEE TRANSACTIONS ON CIRCUITS AND SYSTEMS-II*, 56(3):205–209, 2009.

[61] R. Nilavalan, I.J. Craddock, A. Preece, J. Leendertz, and R. Benjamin. Wideband microstrip patch antenna design for breast cancer tumour detection. *IET Microw. Antennas Propag.*, 2(1):277–281, 2007.

[62] S. Salvador and G. Vecchi. On some experiments with uwb microwave imaging for breast cancer detection. In *Antennas and Propagation Society International Symposium*, pages 253–256, Honolulu, HI, 2007.

[63] X. Chen, J. Liang, P. Liand L. Guo, C.C. Chiau, and C.G. Parini. Planar uwb monopole antennas. In *Microwave Conference Proceedings, 2005. APMC 2005. Asia-Pacific Conference Proceedings*, 2005.

[64] D. R. Gibbins, M. Klemm, I. J. Craddock, G. S. Hilton, and D. L. Paul. The design of a wide slot antenna for the transmission of uwb signals into the human body using fdtd simulation. In *The Second European Conference on Antennas and Propagation, 2007. EuCAP 2007.*, pages 1–5, nov. 2007.

136

[65] Ali A. Dheyab Al-Sajee and Karim A. Hamad. IMPROVING BANDWIDTH RECTANGULAR PATCH ANTENNA USING DIFFERENT THICKNESS OF DIELECTRIC SUBSTRATE. *ARPN Journal of Engineering and Applied Sciences*, 4(6):48–56, 2006.

[66] Q. Li, Y.P. Zhang, and J.S. Chang. An inductorless low-noise amplifier with noise cancellation for uwb receiver front-end. In *Solid-State Circuits Conference, 2006. ASSCC 2006. IEEE Asian*, pages 267 – 270, Hangzhou, 2006.

[67] R. Gharpurey. A broadband low-noise front-end amplifier for ultra wideband in 0.18 μ m cmos. *IEEE Journal of Solid-State Circuits*, 40(9):1983–1986, 2005.

[68] J.S. Walling and D.J. Allstot. A gm-boosted current-reuse lna in 0.18 μ m cmos. In *Radio Frequency Integrated Circuit (RFIC) Symposium, 2007 IEEE*, pages 613 – 616, Honolulu, HI, 2007.

[69] Michael T. Reiha and John R. Long. A 1.2 v reactive-feedback 3.1-10.6 ghz low-noise amplifier in 0.13 μm cmos. *IEEE Journal of Solid-State Circuits*, 42(5):1023–1033, 2007.

[70] Yuna Shim, Chang-Wan Kim, Jeongseon Lee, and Sang-Gug Lee. Design of Full Band UWB Common-Gate LNA. *IEEE Microwave and Wireless Components Letters*, 17(10):721–723, 2007.

[71] A. Bevilacqua and A. Niknejad. An ultra-wideband cmos lna for 3.1 to 10.6 ghz wireless receivers. In *IEEE Int. Solid-State Circuit Conf. Tech. Dig.*, page 139–140, 2004.

[72] D.J. Allstot, X.Y. Li, and S. Shekhar. Design considerations for cmos low-noise amplifiers. In *2004, Radio Frequency Integrated Circuits (RFIC) Symposium*, pages 97–100. IEEE, 2004.

[73] T.H. Lee. *The Design of CMOS Radio-Frequency Integrated Circuits*. Cambridge, U.K.: Cambridge Univ. Press, 1998, 1998.

[74] B. Razavi. Design of sample-and-hold amplifiers for high-speed low-voltage a/d converters. In *Custom Integrated Circuits Conference, 1997., Proceedings of the IEEE 1997*, page 59–66, 1997.

[75] Hailang Liang anf Rob.J. Evans and Efstratios Skafidas. Distortion analysis of 30gsample/s cmos switched source follower. In *Circuits and Systems (ISCAS), Proceedings of 2010 IEEE International Symposium on*, pages 4293–4296, Paris, 2010.

[76] A. Colonna. Analisi e progetto di un ricevitore uwb per il rilevamento del carcinoma mammario. Master's thesis, Politecnico di torino, 2010.

[77] A. Lewinski and J. Silva-Martinez. Ota linearity enhancement technique for high frequency applications with im3 below -65 db. *IEEE Transactions on Circuits and Systems—Part II*, 51(10):542–548, 2004.

[78] T.Y. Lo and C.C. Hung. A 40 mhz double differential-pair cmos ota with -60 db im3. *IEEE Transactions on Circuits and Systems—Part I*, 55(1):246–253, 2008.

[79] J. Ravatin, J. Oudinot, S. Scotti, A. Le-Clercq, and J. Lebrun. Full transceiver circuit simulation using vhdl-ams. *Microwave Engineering*, pages 29–33, 2002.

[80] M. Sida, R. Ahola, and D. Wallner. Bluetooth transceiver design and simulation with vhdl-ams. 19(2):11 – 14, mar 2003.

[81] Pavel V. Nikitin and C.-J. Richard Shi. Vhdl-ams based modeling and simulation of mixed-technology microsystems: a tutorial. *Integration, the VLSI Journal*, 40:261–273, 2007.

[82] S.-C. Shin, J.-H. Huang, K.-Y. Lin, and H. Wang. A 1.5-9.6 ghz monolithic active quasi-circulator in 0.18μm cmos technology. *IEEE Microwave and Wireless Components Letters*, 18(12):797–799, 2008.

[83] J. Kim. Adaptive-bandwidth phase-locked loop with continuous background frequency calibration. *IEEE Trans. Circuits Syst. II*, 56(3):205–209, 2009.

[84] Y.-H. Seo, J.-S. Kim, H.-J. Park, and J.-Y. Sim. A 0.63 ps resolution, 11b pipeline tdc in 0.13μm cmos. In *2011 Symposium on VLSI Circuits (VLSIC)*, pages 152–153, Honolulu, 2011.

[85] J.-S. Kim, Y.-H. Seo, Y. Suh, H.-J. Park, and J.-Y. Sim. A 300-ms/s, 1.76-ps-resolution, 10-b asynchronous pipelined time-to-digital converter with on-chip digital background calibration in 0.13μm cmos.

[86] R. Payne, C. Sestok, W. Bright, M. El-Chammas, M. Corsi, D. Smith, and N. Tal. A 12b 1gs/s sige bicmos two-way time-interleaved pipeline adc. In *2011 IEEE International Solid-State Circuits Conference Digest of Technical Papers (ISSCC)*, pages 182–184, feb. 2011.

[87] Chun-Ying Chen and Jiangfeng Wu. A 12b 3gs/s pipeline adc with 500mw and 0.4 mm^2 in 40nm digital cmos. In *2011 Symposium on VLSI Circuits (VLSIC)*, pages 120–121, june 2011.

[88] I.D. Robertson and A.H. Aghvami. Novel monolithic ultra-wideband unilateral 4-port junction using distributed amplification techniques. In *Microwave Symposium Digest, 1992., IEEE MTT-S International*, pages 1051 – 1054, Albuquerque, 1992.

[89] F. Zhu, W. Hong, and K. Wu J.-X. Chen. Ultra-wideband single and dual baluns based on substrate integrated coaxial line technology. *IEEE Trans. Microw. Theory Tech.*, 60(10):3062–3070, 2012.

[90] J. Xia, Z. Wang, and X. Guo. 3-11 ghz monolithic balun in cmos technology for uwb applications. In *Microwave and Millimeter Wave Technology, 2007. ICMMT '07. International Conference on*, pages 1–3, Builin, 2007.